

**Three-dimensional numerical modelling of
static and transient Coulomb stress changes on
intra-continental dip-slip faults**

Von der Naturwissenschaftlichen Fakultät der
Gottfried Wilhelm Leibniz Universität Hannover

zur Erlangung des Grades
Doktorin der Naturwissenschaften (Dr. rer. nat.)

genehmigte Dissertation

von

Meike Bagge, M. Sc.

[2017]

Referentin: Prof. Dr. rer. nat. Andrea Hampel

Korreferent: Prof. Dr. sc. nat. Ulrich Heimhofer

Tag der Promotion: 10.02.2017

Abstract

Earthquakes on intra-continental faults pose substantial seismic hazard to populated areas. The interaction of faults is an important mechanism of earthquake triggering and can be investigated by the calculation of Coulomb stress changes. Using three-dimensional finite-element models, co- and postseismic stress changes and the effect of viscoelastic relaxation on dip-slip faults are investigated. The models include elastic and viscoelastic layers, gravity, ongoing regional deformation as well as source and receiver fault zones. A parameter study with a systematic fault geometry, which is independent of a specific earthquake, shows that high coseismic stress increase occurs in along-strike prolongation of the source fault and in small areas parallel to the source fault. The coseismic slip and coefficient of friction influence the magnitude of stress changes, while the fault dip also influences the distribution. The stress changes can be explained by the spatial distribution of the coseismic strain. Differences in normal and thrust fault models are mainly caused by the different fault dips. The postseismic stress changes – caused by viscoelastic relaxation and interseismic stress increase – modify the coseismic stress changes that stress-triggering zones can change to stress-shadow zones and *vice versa*. Stress changes induced by viscoelastic relaxation can outweigh the interseismic stress increase so that negative stress changes can persist for decades. The lower the viscosity of the lower crust or lithospheric mantle, the more pronounced is the effect of viscoelastic relaxation in the first years. Layers with low viscosity define the area of highest postseismic velocities and hence determine relaxation and stress changes. The application of the model to the active Wasatch fault system in the eastern Basin and Range Province (Utah) is the first study in which an entire series of earthquakes on a natural fault system is simulated in a finite-element model using realistic fault geometries and palaeo-seismological data to investigate the co- and postseismic Coulomb stress changes for palaeo-earthquakes and the future evolution. The coseismic stress changes extend over all modelled fault segments. The postseismic stress changes and velocities show that the postseismic relaxation dominates the first years after the earthquake, while in the hundredth year the stress increase by the regional stress field dominates. The analysis of the stress changes since the last event per fault segment shows that the Brigham City segment (~780 bar) and Salt Lake City segment (~510 bar) have accumulated the most stress since the last earthquake. Modelled hypothetical present-day earthquakes suggest that present-day ruptures on the Brigham City segment or Salt Lake City segment could experience $M \sim 7.1$ or $M \sim 7.0$ earthquakes, respectively, which pose high seismic hazard for the metropolitan areas.

Keywords: interaction of earthquakes, stress transfer, finite-element-models

Kurzfassung

Erdbeben an intrakontinentalen Ab- und Überschiebungen stellen eine erhebliche seismische Gefährdung dar. Die Interaktion von Störungen ist ein wichtiger Mechanismus zur Auslösung von Erdbeben und kann mithilfe der Berechnung der Coulomb-Spannungsänderungen erforscht werden. Unter Verwendung von dreidimensionalen Finite-Elemente-Modellen werden ko- und postseismische Spannungsänderungen und der Einfluss der viskoelastischen Relaxation auf Ab- und Überschiebungen untersucht. Die Modelle beinhalten elastische und viskoelastische Layer, Gravitation, permanente regionale Deformation sowie Quell- und Empfänger-Störungen. Eine Parameterstudie mit einer systematischen Störungsgeometrie, die unabhängig von einem bestimmten Erdbeben ist, zeigt, dass hohe koseismische Spannungszunahmen sowohl entlang der Streichrichtung der Quell-Störung als auch teilweise in einem kleinen Bereich parallel zur Quell-Störung auftreten. Der koseismische Versatz und der Reibungskoeffizient beeinflussen die Magnitude der Spannungsänderung, wohingegen das Einfallen der Störungen die Verteilung beeinflusst. Die Spannungsänderungen können anhand der räumlichen Verteilung der Verformung erklärt werden. Unterschiede in den Ab- und Überschiebungsmodellen entstehen hauptsächlich durch das unterschiedliche Einfallen der Störungen. Die postseismischen Spannungsänderungen, die durch die viskoelastische Relaxation und die interseismische Spannungszunahme verursacht werden, verändern die koseismischen Spannungsänderungen, sodass sich *Stress-Triggering-Zonen* in *Stress-Shadow-Zonen* umwandeln können und umgekehrt. Spannungsänderungen, die durch die viskoelastische Relaxation erzeugt werden, können die interseismische Spannungszunahme überlagern, sodass negative Spannungsänderungen über Jahrzehnte existieren können. Je geringer die Viskosität der unteren Kruste oder des lithosphärischen Mantels ist, desto größer ist der Effekt der viskoelastischen Relaxation in den ersten Jahren nach dem Beben. Layer mit einer geringen Viskosität stehen im Zusammenhang mit Bereichen hoher postseismischer Geschwindigkeiten und bestimmen somit über den Prozess der Relaxation und die Spannungsänderungen. Die Anwendung des Modells auf das aktive Wasatch-Störungssystem in der östlichen *Basin-and-Range* Provinz repräsentiert eine erste Studie, in welcher eine vollständige Serie von Erdbeben eines natürlichen Störungssystems in einem Finite-Elemente-Modell simuliert wird. Unter Verwendung von realistischer Störungsgeometrie und paläoseismologischen Daten werden ko- und postseismische Spannungsänderungen für Paläo-Erdbeben sowie die zukünftige Entwicklung untersucht. Die koseismischen Spannungsänderungen erstrecken sich über alle modellierten Störungssegmente. Die postseismischen Spannungsänderungen und Geschwindigkeiten zeigen, dass die postseismische Relaxation in den ersten Jahren nach dem Beben überwiegt und im hundertsten Jahr die Spannungszunahme durch das regionale Spannungsfeld bestimmt wird. Die Untersuchung der Spannungsänderungen seit dem letzten Beben per Störungs-Segment zeigt, dass das Brigham City Segment (~780 bar) und Salt Lake City Segment (~510 bar) aktuell am meisten Spannung akkumuliert haben. Modellerte hypothetische Erdbeben zum heutigen Zeitpunkt deuten darauf hin, dass ein heutiges Erdbeben am Brigham City Segment oder Salt Lake City Segment eine Magnitude von $M \sim 7.1$ oder $M \sim 7.0$ aufweisen könnte, was eine erhebliche seismische Gefährdung für die Metropolregionen darstellt.

Schlüsselwörter: Interaktion von Erdbeben, Spannungsübertragung, Finite-Elemente-Modelle

Content

1	Introduction	1
1.1	Motivation	1
1.2	Topic and aim of this thesis	9
1.3	Method of numerical finite-element-modelling	10
2	Three-dimensional finite-element modelling of coseismic Coulomb stress changes on intra-continental dip-slip faults	15
2.1	Introduction	16
2.2	Model setup	18
2.3	Model results	21
2.4	Discussion.....	31
2.5	Conclusions	40
3	Postseismic Coulomb stress changes on intra-continental dip-slip faults due to viscoelastic relaxation in the lower crust and lithospheric mantle: insights from 3D finite-element modelling	42
3.1	Introduction	43
3.2	Model setup	45
3.3	Model results	48
3.4	Discussion.....	58
3.5	Conclusions	64
4	Coulomb stress changes on the Wasatch fault (Utah).....	65
4.1	Introduction	66
4.2	Geological setting and earthquake history.....	68
4.3	Model setup	73
4.4	Model results	76
4.5	Discussion.....	85
4.6	Conclusions	93
5	Discussion.....	95
5.1	Strengths and limitations of the models	95
5.2	Comparison of the studies in this thesis	98
5.3	Comparison with other natural earthquakes	100
5.4	Consideration of other stress transfer mechanisms	102
5.5	Implications for earthquake triggering and forecast.....	102
6	Conclusions and Outlook.....	104
7	Acknowledgements	105
8	References	106
9	Curriculum Vitae	117
10	Publications	118

1 Introduction

1.1 Motivation

1.1.1 Worldwide earthquake distribution

Earthquakes pose a substantial seismic hazard to populated areas. However, so far time, location and magnitude of the next disastrous earthquake cannot be predicted (Geller et al. 1997, Stein 2003). Beside the prevalent occurrence of inter-continental earthquakes along plate boundaries, also a multitude of strong and devastating earthquakes occur on intra-continental fault zones (Fig. 1.1). Examples for recent devastating intra-continental earthquakes are the 2003 $M_w = 6.6$ Bam (Iran) (Fu et al. 2004), the 2009 $M_w = 6.3$ L'Aquila (Italy) (Serpelloni et al. 2012), the 2008 $M_w = 7.9$ Wenchuan (China) (Shan et al. 2013, Wang et al. 2014a) and the 2016 $M = 6.2$ central Italy (USGS homepage <http://earthquake.usgs.gov/>) earthquakes. Nevertheless, the potential to cause moderate to large earthquakes on intra-continental fault zones received less attention than the earthquake hazard on inter-continental fault zones, partly due to the fact that intra-continental fault zones are much less well defined, have average lower slip rates and longer earthquake recurrence intervals (England and Jackson 2011). However, intra-continental earthquakes also pose high substantial seismic hazard to populated areas and the investigation is of crucial importance.

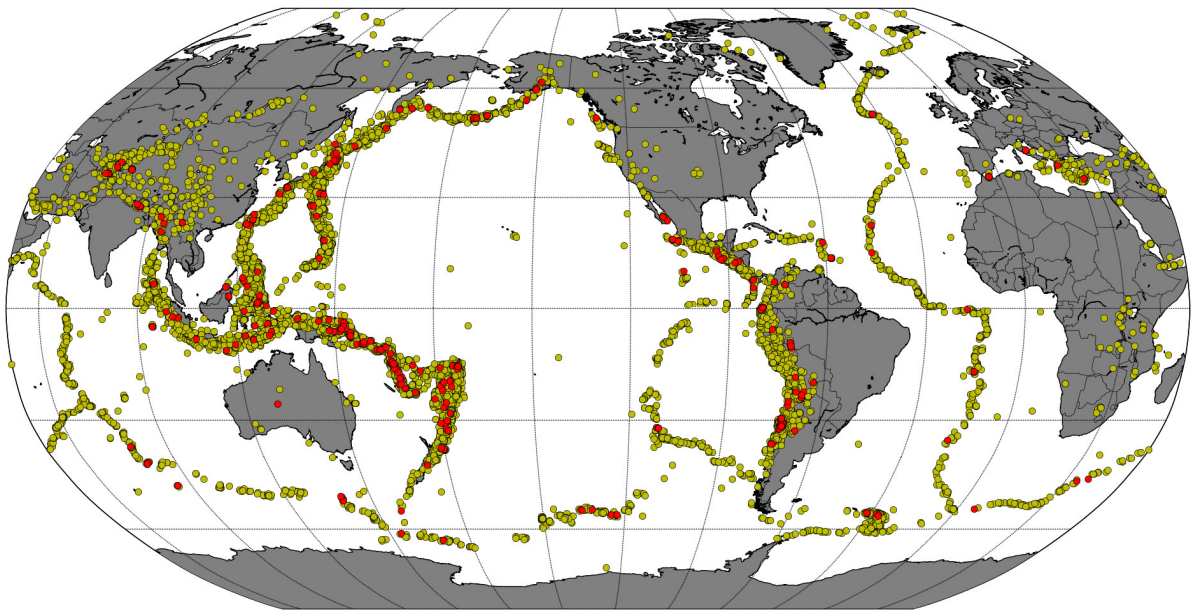


Figure 1.1: Worldwide earthquake distribution during the last two years (17/09/2014-17/09/2016). Earthquakes with magnitudes $4.5 < M < 6$ are shown in yellow and $M \geq 6$ in red. (Earthquake data source: USGS homepage <http://earthquake.usgs.gov/>).

1.1.2 Earthquake cycle models

Earthquakes are caused by the sudden release of elastic strain, which has been accumulated in the rigid plates during the interseismic phase mainly by the regional stress field. Earthquakes are triggered when the critical shear stress on a fault zone is exceeded, the fault fails and the crustal blocks slip. One way to describe the frictional behaviour and slip on fault zones is the Mohr-Coulomb criterion

$$|\tau_{\max}| = C + \mu\sigma_n$$

where τ_{\max} is the critical shear stress, C is the cohesion, σ_n is the normal stress and μ the friction coefficient (Scholz 2002). The friction coefficient for intra-continental faults generally ranges between 0.3 and 0.8 (Byerlee 1978, Collettini et al. 2009, Hurd and Zoback 2012, Niemeijer and Collettini 2014, Townend and Zoback 2000). Earthquakes occur repeatedly defined as earthquake cycles and several models for earthquake behaviour were developed. These models connect strain energy and slip depending on time over several earthquake cycles (Fig. 1.2, Friedrich et al. 2003).

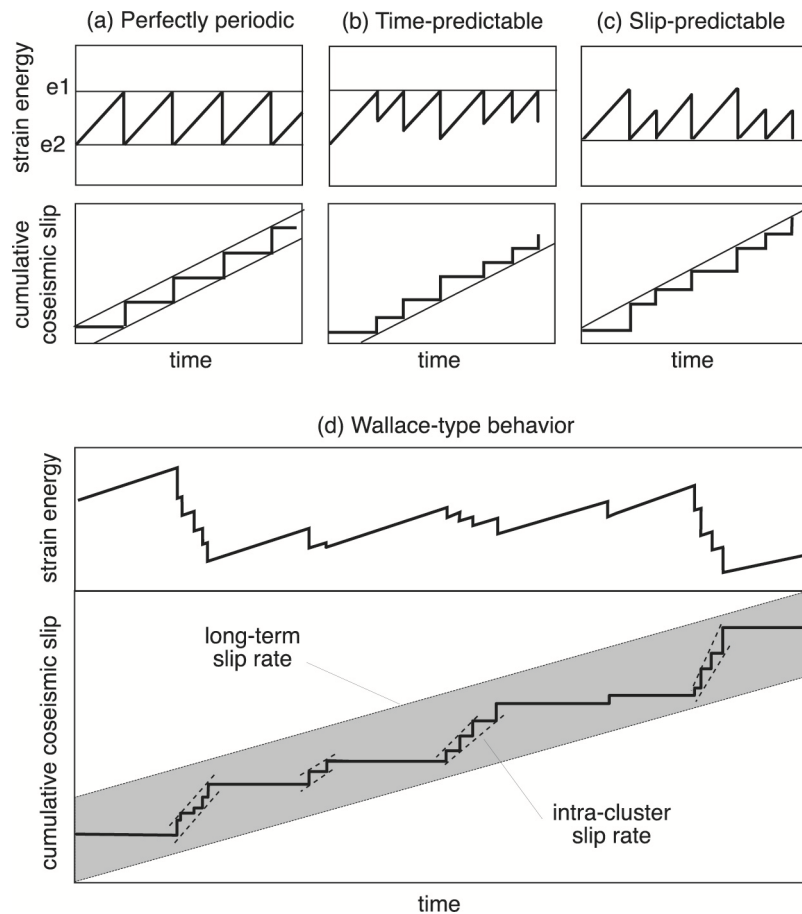


Figure 1.2: Strain release models for earthquakes. (a) Reid-type (perfectly periodic), (b) Time-predictable, (c) Slip-predictable and (d) Wallace-type (Friedrich et al. 2003 and references therein: Reid 1910, Scholz 2002, Shimazaki and Nakata 1980, Wallace 1987)

The perfectly periodic earthquake recurrence model (Reid-type) implies uniform slip, uniform strain release and a uniform recurrence interval resulting in a periodic earthquake interval (Fig. 1.2a). The whole elastic strain energy, which has been accumulated since the last earthquake, is completely released during an earthquake and in a periodic time interval. The model also implies that the uniform far-field displacement rate agrees with the uniform displacement rate on fault zones. For the perfectly periodic model, time and slip are predictable (Reid 1910). If the slip rate is constant, but the interseismic interval and size of earthquake is not perfectly periodic, the time-predictable (Fig. 1.2b) and slip-predictable (Fig. 1.2c) models are applied. In the time-predictable model the earthquake is triggered as soon as the fault has accumulated maximal strain (critical strain energy), but the strain release differs. With a constant slip rate the time of the next earthquake is predictable, but not the size. The slip rate and the size of the last earthquake predict the time (Shimazaki and Nakata 1980). In contrast, in the slip-predictable model the whole accumulated strain since the last earthquake is released. The size of the next earthquake is predictable, but not the time. Therefore, the slip rate and time since the last earthquake predict the size of the next earthquake (Shimazaki and Nakata 1980). If the slip rate is not constant, the Wallace-type model can be applied, which defines earthquake clusters (Fig. 1.2d). The slip rate is separated in a lower long-term slip rate and higher intra-cluster slip rates. The long-term slip rate is the average over time with earthquake clusters and times without earthquakes, whereas the intra-cluster slip rates include small time intervals of high earthquake occurrence (earthquake clusters). A variable slip rate implies that the short-term intra-cluster slip rates differ from the far-field displacement (=long-term slip rate) (Wallace 1987).

In nature, the earthquake occurrence generally differs from these models, so that a prediction of the time for the next earthquake is so far impossible (Geller et al. 1997, Stein 2003). The current stress situation and the status in the earthquake cycle of the faults are unknown. Furthermore, an earthquake can also be triggered by different values of stress accumulation since the last earthquake. Therefore, the analysis of stress changes instead of the investigation of the absolute stress situation has become an important tool for the investigation of earthquakes and future seismic hazard assessment (Stein 1999). The analysis of stress changes reveals no information about the status in the earthquake cycle and the missing value of stress for failure, but it reveals information about increased or decreased seismic hazard and whether the fault has been brought nearer to failure and whether the next earthquake on the considered fault is promoted or delayed.

1.1.3 Interaction of faults (stress changes)

Apart from the stress increase by the regional stress field, stress changes can also be caused by the interaction of faults and the stress transfer between fault zones. Therefore, the investigation of the interaction of faults is crucial for the assessment of future seismic hazards. Several studies have shown that earthquakes interact by stress transfer and that mainshocks and aftershocks, as well as earthquakes with larger temporal and spatial differences, can be linked (e.g. King et al. 1994, Ryder et al. 2012, Stein 1999, 2003). An earthquake on a so-called source fault can cause stress changes on adjacent faults (receiver faults), which may ultimately trigger or delay other earthquakes. Investigating stress transfer by the calculation of Coulomb stress changes is widely applied for assessment of future seismic risk (King et al. 1994, Stein 1999). The Coulomb stress changes (Coulomb failure stress, ΔCFS) associated with an earthquake on a source fault can be calculated for pre-defined planes (e.g. fault planes) by the commonly used equation that is also used in this thesis (e.g. Freed 2005, Stein et al. 1992, Stein 1999, 2003)

$$\Delta\text{CFS} = \Delta\tau - \mu'\Delta\sigma_n$$

where $\Delta\tau$ is the shear stress change on a fault, μ' is the effective coefficient of friction and $\Delta\sigma_n$ is the normal stress change. The shear stress change on a fault plane is defined positive in direction of fault slip. Figure 1.3 shows the relation between displacements and Coulomb stress changes. A displacement corresponding to the coseismic slip direction caused by the regional stress field leads to positive stress changes, whereas a opposite slip direction leads to negative stress changes. The normal stress change is defined positive if the fault is clamped. The effective coefficient of friction, which includes the effects of pore fluids and material properties of the fault zone, is often used if the effect of pore fluids cannot be quantified (Harris 1998) and will also be used in this study.

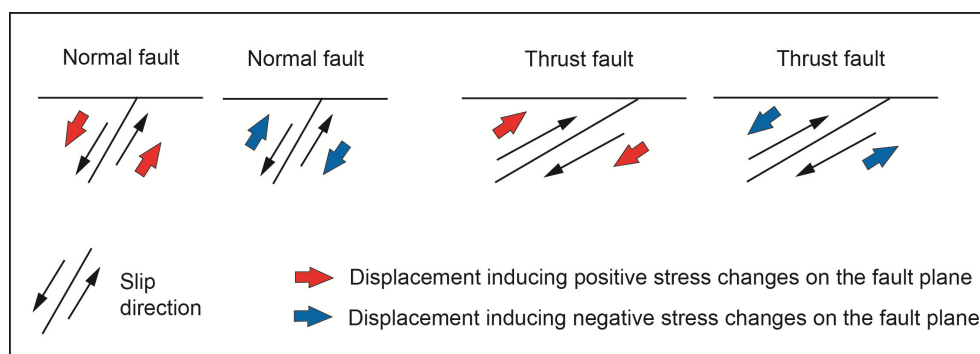


Figure 1.3: Schematic illustration of the coupling between displacements and Coulomb stress changes for normal and thrust faults. Black arrows show the coseismic slip direction caused by the applied regional stress field.

Positive stress change results from an increase in shear stress and/or a decrease in normal stress. If the Coulomb stress change is positive, the receiver fault has been brought closer to failure and seismic hazard is increased. A negative Coulomb stress change implies that the next earthquake is delayed and seismic hazard is decreased in the considered time interval. Zones of positive and negative stress changes are also called stress-triggering zones and stress-shadow zones, respectively. Depending on the status of a fault in its earthquake cycle and the previously accumulated stress, a stress change of 1 bar can be sufficient to trigger an earthquake on a fault (King et al. 1994).

The calculation of stress changes is often presented in map view for theoretical fault zones oriented parallel to the source fault or oriented optimal to the stress field (King et al. 1994, Nostro et al. 2001). However, of particular interest is the calculation of stress changes on fault zones because they represent pre-defined breaking points (zones of weakness), where failure and the next earthquakes can be expected. For the calculation of shear and normal stress on fault zones, the fault geometry has to be known (e.g. as for the Wasatch fault zone, Chapter 4) or a parameter study has to be considered, which includes generalised fault geometry (Chapter 2 and 3). The advantage of the parameter study in this thesis is that the fault geometry for specific faults does not have to be known and general fault geometry can be used.

1.1.4 Mechanisms of stress transfer and earthquake triggering

The stress transfer between earthquakes and fault zones is caused by a number of mechanisms. Next to coseismic (static) stress transfer also dynamic and postseismic (transient) stress transfer are important for earthquake triggering (Freed 2005). Coseismic stress changes are caused by sudden slip on a ruptured fault zone. The ruptured fault is affected by coseismic stress drop and causes stress changes on surrounding fault zones in distance of several fault lengths. Positive and negative coseismic stress changes can occur on the surrounding receiver fault zones. The maximum coseismic stress changes on receiver faults are generally in the range of a few percent of the coseismic stress drop (King et al 1994, Stein 1999). The coseismic stress drop for global moderate to large earthquakes ranges between 0.3 to 50 MPa (Allmann and Shearer 2009). Static stress changes can often explain connections between mainshock, aftershocks and earthquake sequences (Lin and Stein 2004, Mallman and Zoback 2007, Ryder et al. 2012, Stein 1999).

Dynamic and postseismic (transient) stress changes are caused by time-dependent stress transfer mechanisms. These mechanisms act on different time and spatial scales and in

case of positive transient stress changes they can cause delayed earthquake triggering. Dynamic stress changes caused by seismic waves occur over more than thousands of kilometres (Freed 2005). Depending on travel time and velocity of seismic waves, the dynamic stress changes occur in a range of up to several days (Pollitz et al. 2012). Dynamic stress changes by seismic waves are an order of magnitude larger than static stress changes and producing primary only stress increase (Belardinelli et al. 1999, Freed 2005).

An important mechanism of stress transfer is the postseismic viscoelastic relaxation, which represents the transient response of the viscoelastic layers (e.g. lower crust and mantle), which exhibit viscous flow instead of brittle behaviour. Primary the sudden coseismic slip in the brittle upper crust leads to elastic deformation in the viscoelastic lower crust and mantle. In the postseismic phase the stress relaxes by viscous flow and stress is transferred to the elastic upper crust, where another earthquake can be triggered by stress increase (Freed and Lin 2001, Freed 2005). The viscoelastic relaxation can act over hundreds of kilometres (Chéry et al. 2001) as well as hundreds of years, primarily depending on viscosity and coseismic stress drop.

In addition, poroelastic effects can lead to Coulomb stress changes (poroelastic stress changes). Pore pressure changes are caused by the dislocation of the earthquake and cannot be relaxed by fluid flow at once leading to postseismic stress changes and deformation in the surrounding area of the ruptured fault zone (Freed 2005). Depending on the permeability the stress changes by poroelastic effects can occur short-term or over several years (Cocco and Rice 2002, Dempsey et al. 2013). Another stress transfer mechanism is postseismic creep on a ruptured fault zone (afterslip). The slip after the main earthquake, also called aseismic slip, is caused by unrelieved stress on the ruptured fault zone. Afterslip occurs within the rupture surface or in deeper extension of the fault, where high pressures occur (Freed 2005). Afterslip occurs over days to years and leads to stress changes and deformation near the source fault (Hsu et al. 2006).

1.1.5 State of the art

Because the stress transfer plays a crucial role for earthquake triggering, several numerical models have been evaluated to calculate co- and postseismic stress changes. Okada (1992) developed a model that enables the calculation of coseismic stress changes by dislocations in an elastic half-space with uniform isotropic elastic properties. Following Okada (1992), the popular and freely available software Coulomb has been developed and is continuously enhanced (Toda et al. 2011). This software enables, for example, the calculation of coseismic

stress changes on mapped faults and earthquake nodal planes (e.g. fault plane) caused by coseismic fault slip.

Because the vertical orientation of the fault zones simplifies the stress change calculation, first studies of coseismic stress change are applied to strike-slip faults. Stein et al. (1992) calculated the coseismic stress changes on vertical strike-slip faults in south California. They show that the 1992 $M = 7.4$ Landers earthquake was localised in a region of positive stress changes by around 1 bar caused by the previous 1975 Galway Lake, 1979 Homestead Valley, 1986 North Palm Springs and 1992 Joshua Tree earthquakes, which were located in a distance of up to 50 km from the Landers earthquake (Stein et al. 1992). The stress calculation of the Landers earthquake reveals a connection to the $M = 6.5$ Big Bear aftershock, which was located in a zone of stress increase by around 3 bar caused by the Landers earthquake. The comparison of the stress change distribution and the distribution of aftershocks shows that aftershocks occurred in regions of positive stress changes of ≥ 0.1 bar during a period of 25 days after the Landers earthquake (King et al. 1994, Stein et al. 1992). The analysis of an earthquake sequence on the North Anatolian strike-slip fault (Turkey) demonstrates that nine out of ten ruptures were located in stress triggering zones of previous earthquakes (Stein et al. 1997).

The calculation of stress changes on dip-slip faults is applied to investigate the 1971 $M = 6.7$ San Fernando and 1994 $M = 6.7$ Northridge thrust fault earthquakes with the result that the San Fernando earthquake brought the Northridge fault zone closer to failure by positive stress transfer (Stein et al. 1994). Stein (1999) shows a correlation between coseismic Coulomb stress changes and the seismicity rate changes after the Northridge earthquake. Another example is the 2008 $M_w = 7.9$ Wenchuan earthquake (oblique reverse slip) on the Longmenshan fault zone (China) that causes positive static Coulomb stress changes on the southern part of the Longmenshan fault zone; the area, where 2013 the $M_w = 6.6$ Lushan earthquake was triggered (Jia et al. 2010, Parsons et al. 2008, Parsons and Segou 2014).

Coseismic stress transfer in an extensional regime has been investigated by Nostro et al. (1997). The 1980 Irpinia (Italy) normal-faulting event increases the coseismic stress on the strike-slip Potenza fault, where 1990 and 1991 earthquakes were triggered. The analysis of an earthquake sequence between 1688 and 1980 in the southern Apennines (Italy) reveals that most of the large historical earthquakes are located in stress-triggering zones, primarily in along-strike prolongation of previous fault ruptures (Nostro et al. 1997). Serpelloni et al. (2012) calculated the coseismic stress changes for the 2009 $M_w = 6.3$ L'Aquila normal fault

earthquake in the Apennines (Italy) and found out that most of the large aftershocks were triggered in zones of positive stress changes (0.2-13 bar).

These studies of coseismic stress changes on strike- and dip-slip faults show that earthquakes can interact by coseismic stress transfer. Elastic dislocation models are suitable for the calculation of coseismic stress changes, but they ignore the transient effects, so that other models are required for the calculation of postseismic stress changes and to explain time delay between earthquake triggering. Piersanti et al. (1995, 1997) developed a spherical self-gravitating Earth model for the analysis of postseismic viscoelastic deformation and stress transfer. Based on Piersanti et al. (1995, 1997), Nostro et al. (2001) used a numerical code to create a layered medium with viscoelastic (Maxwell) rheology for the investigation of postseismic stress changes and the effect of viscoelastic relaxation in an extensional regime depending on the rheological stratification and the layer thickness. The importance of viscoelastic relaxation for transient stress transfer and earthquake triggering is shown by the analysis of the 1992 $M = 7.3$ Landers strike-slip earthquake and the 1999 $M = 7.1$ Hector Mine strike-slip earthquake (California). While the investigation of coseismic stress changes reveals no significant connection between both earthquakes, the analysis of the transient deformation suggests that the postseismic relaxation of the Landers earthquake causes a stress increase of about 0.7 bar on the ruptured fault zone of the Hector Mine earthquake and therefore contributes to earthquake triggering (Pollitz and Sacks 2002). Besides viscoelastic relaxation, other transient effects that contribute to the triggering of the Hector Mine earthquake are dynamic stress changes (Gomberg et al. 2001), poroelastic effects (Masterlark and Wang 2002) and the tectonic background (Cianetti et al. 2005, Pollitz and Sacks 2002). Using a three-dimensional viscoelastic model, Wang et al. (2014b) demonstrate that the viscoelastic relaxation influenced the stress transfer between the 2008 Wenchuan earthquake and the 2013 Lushan earthquake and both co- and postseismic stress changes brought the ruptured fault of the Lushan earthquake closer to failure (Wang et al. 2014b).

Previous studies of stress change calculation for the investigation of fault interaction are related to particular faults and specific recent earthquakes, strike-slip faults, static stress changes without viscoelastic effects and/or other postseismic stress transfer mechanisms without the focus on the postseismic relaxation process. Many studies only consider a viscoelastic half-space instead of individual viscoelastic layers and/or neglect gravity and/or the regional stress field. Generally, a slip distribution is used that is not necessarily consistent with the regional stress field and derives from inverse modelling of geodetic data resulting in a dependence on local geological conditions and data coverage.

1.2 Topic and aim of this thesis

The aim of this thesis is the investigation of the interaction of intra-continental fault zones and earthquakes by calculating co- and postseismic Coulomb stress changes on dip-slip fault planes using three-dimensional finite-element models. This investigation consists of three studies. The first and the second study are parameter studies with systematic fault geometry independent of a specific earthquake. Both, models in an extensional regime with a normal fault array and models in a compressional regime with a thrust fault array are created. The first parameter study implies the investigation of the coseismic stress changes (Chapter 2) and the second one shows the postseismic stress changes (Chapter 3). In the systematic coseismic study the influence of the fault dip, dip direction, coefficient of friction and coseismic slip on the stress changes will be investigated and linked to the strain field. In the systematic postseismic study the influence of the viscosity of the lower crust and lithospheric mantle on the stress changes and the transient effect of viscoelastic relaxation will be investigated and linked to the postseismic velocities. The third study (Chapter 4) involves the application of the models to the active Wasatch fault region in the eastern Basin and Range Province (Utah) where no recent high magnitude earthquake was triggered, but where high seismic hazard for the population exists. This thesis includes a pilot study that firstly modelled an entire series of earthquake cycles for a natural fault system using a three-dimensional finite-element model. The model implements palaeo-seismological data to investigate the interaction of fault zones including the viscoelastic relaxation and co- and postseismic stress changes for palaeo-earthquakes and the future evolution. The main questions in this thesis, which also represent the content of the main chapters, are the following:

- 1) How do fault dip, fault dip direction, magnitude of coseismic slip and the friction coefficient affect the coseismic stress changes on intra-continental normal and thrust faults? (Chapter 2) (Bagge and Hampel, *Tectonophysics*, 2016)
- 2) How do viscosity of the lower crust and lithospheric mantle affect the viscoelastic relaxation and postseismic stress changes on intra-continental normal and thrust faults? (Chapter 3) (Bagge and Hampel, submitted to *International Journal of Earth Sciences*)
- 3) How can the models be applied to earthquake sequences on the Wasatch fault system in the eastern Basin and Range Province (Utah) and how are the co- and postseismic palaeo-Coulomb stress changes and the future evolution? (Chapter 4) (Bagge, Hampel and Gold, in prep., hereafter referred to as Bagge et al., in prep.)

Parameter studies independent of a specific earthquake analysing the general Coulomb stress patterns on dip-slip source and receiver fault planes are sparse and will be presented in the parameter studies. Furthermore, so far no study investigated the stress changes of a fault system over several earthquake cycles concerning to palaeo-seismic data, as it will be presented in the Wasatch fault study. The models in this thesis include a slip distribution that is not prescribed and evolves freely by the regional stress field and is therefore consistent with the tectonic background. Gravity, lithostatic pressure and isostatic effects are implemented in the three-dimensional models. These implementations are important for the investigation of dip-slip faults, which have a vertical slip component. The fault geometry and orientation of each fault are modifiable and the determination of discrete fault planes reveals the calculation of stress changes on the fault planes, for which the change in stress is relevant. In addition, the models are using a linear, temperature-independent Maxwell viscoelasticity. Although this rheology is a simplification, the implementation of viscoelastic layers itself is an advantage compared to the commonly used homogeneous elastic half-space models based on Okada (1992) because the models in this thesis can be used to analyse transient Coulomb stresses caused by postseismic viscoelastic relaxation. The focus of this thesis lays on the coseismic stress changes and on the postseismic stress changes caused by viscoelastic relaxation, hence, other mechanisms of stress transfer are neglected. Seismic waves and dynamic stress triggering are not modelled or investigated in this thesis. The poroelastic properties are not defined, but the effective coefficient of friction is applied, which considers the poroelastic stress changes, assuming that the pore pressure is proportional to the normal stress (Cocco and Rice 2002). Afterslip modelling is not required in this thesis because the model setup determines that coseismic slip is complete in the coseismic phase. Another advantage of the models in this thesis is that they allow the general comparison between normal and thrust faults due to a similar model setup in the parameter studies. The models are changeable in many parameters (e.g. rheology, geometry) and therefore, they are very well suitable for parameter studies (Chapter 2-3) as well as for the application to natural fault systems (Chapter 4).

1.3 Method of numerical finite-element-modelling

For the analysis of the interaction of earthquakes and the calculation of stress changes analytical methods are insufficient for the solution of complex differential equations. Therefore, numerical models have to be applied to describe complex structures and mechanisms of the earth system. Numerical models enable an approximate solution for the

calculation of processes in complex systems considering each spatial and time scale. In this thesis, the finite-element method is used, a method that belongs to the continuum methods. The area of interest is divided into a finite number of elements, which are connected with nodes so that a finite-element mesh and a continuum is defined. Every finite element receives element differential equations with the typically form

$$[k] \{U\} = \{F\}$$

where $[k]$ is the element stiffness matrix, $\{U\}$ is the vector of (unknown) nodal displacements and $\{F\}$ is the vector of applied nodal forces (Fagan 1992). The applied forces can be defined as boundary conditions. The element equations can be connected to a global equation system including the global stiffness matrix. The solution of the equation is calculated for the nodes and an interpolation delivers the solution for the elements (Fagan 1992).

In this thesis the three-dimensional finite-element models are created with the commercial software Abaqus (versions 6.13-6.14). The creation of the model requires the determination of a number of input parameters, e.g. geometry of the lithosphere and fault zones including interaction conditions, rheologies, boundary conditions and forces and finite-element mesh. Furthermore, surfaces can be defined, which are planes with high concentration of nodes for a better quality and visualisation of results on the surfaces. The forward modelling requires the definition of model steps, which can differ e.g. in time interval or boundary conditions. The determination of model steps and time intervals of the increments defines at which model times the results are calculated and provided as output. Abaqus standard outputs are e.g. coordinates (COORD), displacement (U), strain field (EE) and stress field including normal and shear stress (CPRESS, CSHEAR). Particular useful is the possibility to resolve stress and displacement on pre-defined fault planes and slip between contact surfaces, which is important for the modelling of coseismic slip and the calculation of stress changes on the fault planes. Another advantage of the use of Abaqus is the possibility of creating three-dimensional models, which is important for the modelling of dip-slip faults (horizontal and vertical component), the analysis of the stress changes on the whole fault plane and the investigation of the interaction of fault zones in all spatial directions.

1.3.1 General model setup in this thesis

The model setup of all models in this thesis can be described by a general model setup, which differs in some rheologies, boundary conditions and fault geometry. This thesis involves a normal fault model with systematic fault geometry, a thrust fault model with systematic fault geometry and the Wasatch fault model with a natural fault geometry. Figure 1.4 shows the

setup of the general finite-element model. The finite-element model and the modelling of fault zones are developed, advanced and adapted based on the models by Hetzel and Hampel (2005), Maniatis and Hampel (2008), Hampel et al. (2009) and Karow and Hampel (2010). The general model setup represents an intra-continental lithosphere, which is divided into a 15-km-thick elastic upper crust, a 15-km-thick viscoelastic lower crust and a 70-km-thick viscoelastic lithospheric mantle (Fig. 1.4). The rheological parameters used in the models represent typical values for continental lithosphere (e.g. Ranalli 1995; Turcotte and Schubert 2002). The Poisson's ratio and the Young's modulus are the same in all models. Some parameters like density and viscosity partly differ between the models. No coseismic plastic deformation occurs outside of the fault zones because the upper crust in the model behaves purely elastic. The viscoelastic behaviour is defined as linear temperature-independent Maxwell viscosity. The elastic properties of the upper crust and the viscoelastic properties of the lower crust and the lithospheric mantle are modelled using the Abaqus finite-element material properties "ELASTIC" (Type: isotropic) and "CREEP" (Law: strain hardening).

General model setup

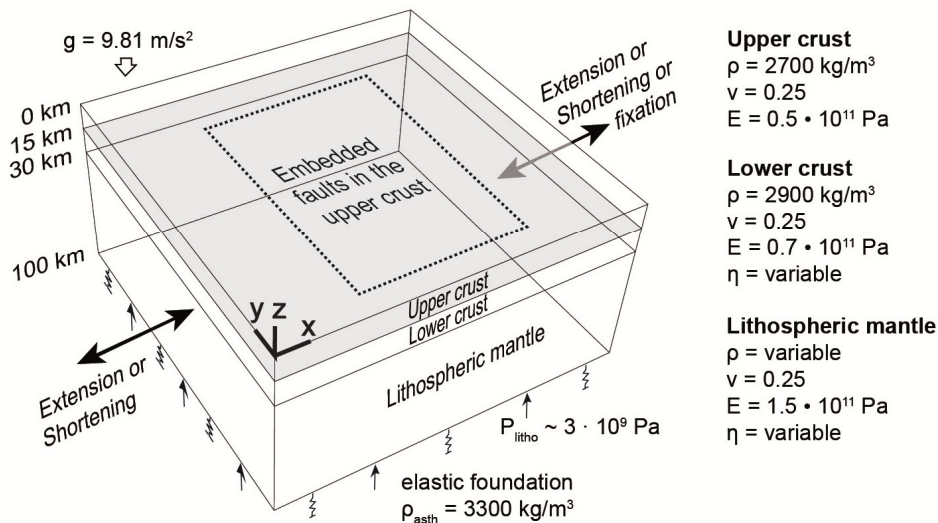


Figure 1.4: Perspective view of the three-dimensional general model setup. In all models in this thesis, the lithosphere is divided into an elastic upper crust, viscoelastic lower crust and viscoelastic lithospheric mantle (rheological parameters are ρ density, E Young's modulus, ν Poisson's ratio and η viscosity). Individual normal or thrust fault planes are embedded in the upper crust, which geometry and parameters (friction coefficient) vary for the different models in this thesis. Gravity is included as body force. Isostatic effects are implemented by a lithostatic pressure (P_{litho} , black arrows at the bottom of the model) and an elastic foundation (springs) representing an asthenosphere. All model sides as well as the bottom of the model are free to move in the vertical direction. Model sides in the xz -plane are fixed in the y -direction. At the model sides in the yz -plane, a velocity boundary condition is applied in the x -direction to extend (normal fault models) or shorten (thrust fault models) the model, which initiates slip on the faults.

Loads in the models are applied as gravity (body force) and lithostatic pressure. Isostatic effects are implemented as lithostatic pressure and elastic foundation representing the asthenosphere. Boundary conditions are applied to define the behaviour of the model sides. The xz -planes are fixed in the y -direction, while the bottom is free to move in the horizontal

and vertical directions. A velocity boundary condition is applied on the yz-planes. In case of the normal fault model, the model is extended and in case of the thrust fault model shortened, both by a defined extension or shortening rate, which partly differs between the models, but is constant in each model run. While in the parameter study the velocity boundary condition is applied on both model sides, in the Wasatch fault model the extension is only applied at one model side and the other side is fixed.

Fault zones are embedded in the upper crust, which geometries and properties partly differ in the models. The faults are modelled as frictional contact interfaces between the footwall and hanging wall of each fault. Slip initiation on the individual fault planes is controlled by the Mohr–Coulomb criterion (Scholz 2002)

$$|\tau_{\max}| = C + \mu\sigma_n$$

where τ_{\max} is the critical shear stress, C is the cohesion, σ_n is the normal stress and μ the friction coefficient, which differs between 0.3 and 0.6 in the models. The cohesion is zero in the models relating to the condition that fault slip is manually controlled by changing the boundary conditions on the fault planes from locked to unlocked (Abaqus Keywords *ROUGH and *FRICTION) (cf. Hampel and Hetzel, 2012, 2015).

The finite-element model is meshed by linear tetrahedron elements (Abaqus Family: 3D stress). Linear elements imply that nodes are only located at the corners of the elements. The node distance is defined in a range between ~3 km at the model edges and ~1 km at the fault zones.

1.3.2 Temporal evolution of the model

Figure 1.5 illustrates the temporal evolution of the cumulative displacement on the source fault and receiver faults. The model is divided in quasi-static analysis steps. First, an isostatic equilibrium is established. In the next analysis step the extension or shortening of the model starts and all faults are free to move to produce a continuous fault slip. The extension or shortening is applied during all following model steps. When a constant fault slip rate is reached, the earthquake cycle starts. In the preseismic phase all faults are locked for stress accumulation. In the coseismic phase the receiver faults are still locked, but the source fault is unlocked, which causes sudden coseismic slip on the source fault (model earthquake). The duration of the preseismic phase, the applied extension or shortening rate and the coefficient of friction determine the size of coseismic slip and magnitude of the earthquake. In the postseismic phase all faults are locked and the stress accumulation by the extension or shortening rate is superposed by the effects of the viscoelastic relaxation. For the parameter

studies one earthquake cycle on the source fault is modelled. In contrast, the Wasatch fault study contains a number of successive earthquake cycles for the individual fault segments based on palaeo-seismological data (for details see Chapter 4), which implies alternating coseismic phases and interseismic (postseismic) phases.

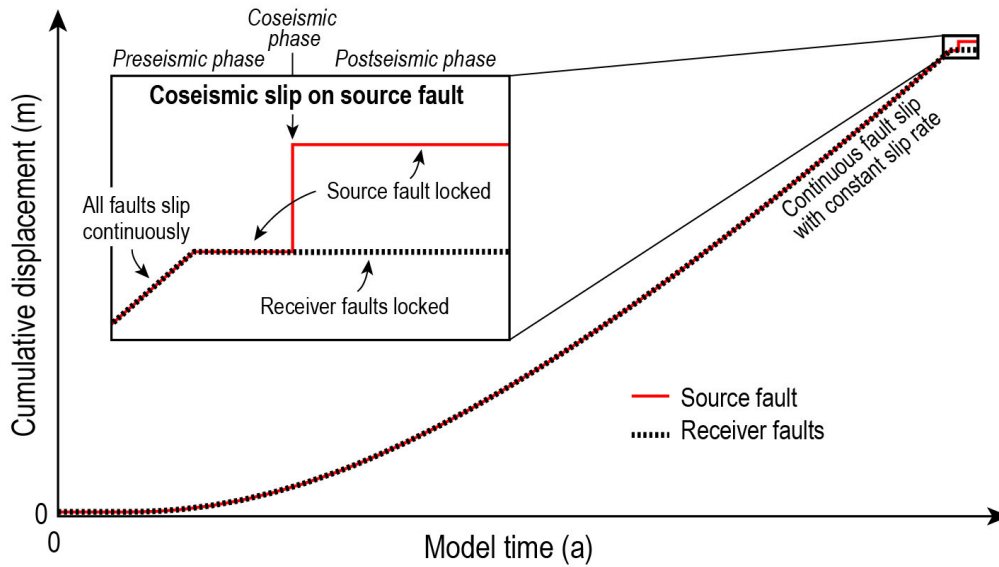


Figure 1.5: Schematic illustration of the temporal evolution of the cumulative displacement on source and receiver faults. After all faults have reached a constant fault slip rate, the earthquake cycle starts (inset).

2 Three-dimensional finite-element modelling of coseismic Coulomb stress changes on intra-continental dip-slip faults

(The content of this chapter was published as Bagge and Hampel, *Tectonophysics*, 2016)

Abstract

Investigating fault interaction plays a crucial role in seismic hazard assessment. The calculation of Coulomb stress changes allows quantifying the stress changes on so-called receiver faults in the surrounding of the fault that experienced the earthquake. A positive stress change implies that the earthquake brought the receiver fault closer to failure while a negative value indicates a delay of the next earthquake. So far, most studies focussed on stress changes for particular faults and earthquakes. Here we present a general analysis of the Coulomb stress changes on intra-continental dip-slip faults using finite-element models with normal and thrust fault arrays, respectively. Our models allow calculating coseismic ("static") stress changes on pre-defined fault planes, whose dip and position can be varied. Gravity and ongoing regional deformation (i.e. shortening or extension) are included. The results for thrust and normal faults show that synthetic receiver faults located in the hanging wall and footwall of the source fault exhibit a symmetric stress distribution, with large areas of negative and small areas of positive Coulomb stress changes. In contrast, faults positioned in along-strike prolongation of the source fault and outside of its immediate hanging wall and footwall undergo mostly positive stress changes. The stress changes are largest at the fault tip that is closer to the source fault. Our results show that the stress change distribution depends on the fault dip while the magnitude depends on the friction coefficient and the amount of coseismic slip. The Coulomb stress changes can be explained by the spatial distribution of the coseismic strain, which shows domains of horizontal extension and shortening that alternate both at the surface and with depth. Our models allow identifying the general patterns of Coulomb stress changes on dip-slip faults, which are often concealed by the peculiarity of the specific fault or earthquake in nature.

Keywords: three-dimensional numerical modelling, fault interaction, coseismic Coulomb stress change, intra-continental normal and thrust faults

2.1 Introduction

Earthquakes on intra-continental faults pose a substantial seismic hazard to populated areas, however, their potential to cause moderate to large earthquakes has received less attention than the earthquake hazard at plate boundaries (England and Jackson 2011). This is at least partly due to the fact that faults in continental interiors have usually much lower slip rates (typically $\leq 1\text{-}2$ mm/a) and hence longer earthquake recurrence intervals than plate boundary faults. As a consequence, no historic records may be available to document their capability to produce earthquakes. Recent examples of devastating intra-continental earthquakes include the 2003 Bam (Iran) (Fu et al. 2004), 2009 L'Aquila (Italy) (Serpelloni et al. 2012) and the 2008 Wenchuan (China) (Shan et al. 2013, Wang et al. 2014a) earthquakes. In addition to the immediate damage, a large earthquake on a source fault can also cause stress changes on adjacent faults (= receiver faults), which may ultimately trigger or delay other earthquakes. Hence, investigating the interaction of faults plays a crucial role in the assessment of future seismic risks. The stress change due to an earthquake is commonly calculated as the change in the Coulomb failure stress ΔCFS (e.g. Freed 2005, Stein et al. 1992, Stein 1999, 2003):

$$\Delta\text{CFS} = \Delta\tau - \mu'\Delta\sigma_n$$

where $\Delta\tau$ is the change in shear stress (positive in direction of slip of the source fault), μ' is the effective coefficient of friction and $\Delta\sigma_n$ is the change in normal stress (positive if fault is clamped). If ΔCFS is positive, the receiver fault has been brought closer to failure; a negative value of ΔCFS implies that the next earthquake is delayed. Note that already a Coulomb stress change of 1 bar (0.1 MPa) on the receiver faults may trigger an earthquake on the receiver faults (King et al. 1994).

Analysis of Coulomb stress changes were first widely applied to strike-slip faults, at least partly because the vertical orientation of the fault planes facilitated the calculation of the stress changes. For example, King et al. (1994) showed that the 1992 $M = 7.4$ strike-slip Landers earthquake was triggered by the $M = 6.5$ strike-slip Big Bear aftershock and a static Coulomb stress change of 0.3 MPa. An interaction between the 1999 strike-slip Hector Mine earthquake and the Landers earthquake was controversially discussed, because the Hector Mine earthquake was located in the transition zone between stress-triggering and stress-shadow zones of the Landers earthquake. In this discussion, other mechanisms invoked for the link between the Landers and Hector-Mine earthquakes were dynamic stress changes (caused by seismic waves) and postseismic relaxation, which may cause transient Coulomb stress changes (e.g. Cianetti et al. 2005, Freed 2005, Freed and Lin 2001, Masterlark and Wang

2002). Many other calculations of coseismic Coulomb stress changes on strike-slip faults exist; for example, the 1999 $M_w = 7.4$ Izmit earthquake at the dextral strike-slip North Anatolian fault was successfully predicted by Stein et al. (1997) using the calculation of the coseismic Coulomb stress changes.

First studies on Coulomb stress changes on dip-slip faults were carried out in Italy after the 1980 Irpinia normal fault earthquake and revealed similar triggering effects as for strike-slip faults. Due to the 1980 Irpinia (Italy, southern Apennines) normal fault earthquake, the coseismic Coulomb stress increased on the nearby dextral Potenza fault, which was ruptured by earthquakes in 1990 and 1991 (Nostro et al. 1997). Similarly, the 2004-2008 normal fault earthquake sequence at the South Lunggar Rift (Tibet) was explained by the Coulomb stress changes (Ryder et al. 2012). The 2004 earthquake increased the Coulomb stress at the synthetic receiver fault on the same side of the graben, which experienced an earthquake in 2005. As a consequence of the 2005 earthquake, the Coulomb stress increased both antithetic receiver faults on the other side of the graben, which were ruptured in 2008 (Ryder et al. 2012). Similar fault interactions after major earthquakes were inferred for contractional tectonic settings. For example, Lin et al. (2011) linked the majority of the aftershocks of the 2003 $M_w = 6.9$ thrust fault Zemmouri (Algeria) earthquake to an increase in coseismic Coulomb stress change. The analysis of static Coulomb stress changes after the 2008 $M_w = 7.9$ Wenchuan earthquake, which ruptured the Beichuan and Pengguan reverse faults (Jia et al. 2010), showed that this oblique thrust event caused considerable positive and negative static Coulomb stress changes on faults in the region (Luo and Liu 2010, Parsons et al. 2008, Toda et al. 2008, Wang et al. 2014a).

In contrast to the number of studies that calculated Coulomb stress changes for particular faults and earthquakes, studies analysing general Coulomb stress patterns on dip-slip source and receiver faults are sparse. Maps of Coulomb stress changes for strike-slip faults parallel to the source fault were presented by King et al. (1994). Based on the thrust and strike-slip fault array that included the source fault of the 2003 Zemmouri earthquake, Lin et al. (2011) calculated the Coulomb stress changes for different positions of the receiver faults relative to the source fault. Recently, Wang et al. (2014a) showed in a systematic investigation using the setting of the 2008 Wenchuan earthquake that Coulomb stress changes are sensitive to the coseismic slip of source fault, the friction coefficient as well as the orientation of the receiver fault. The correct slip distribution is particularly important, because the stress change highly depends on the slip distribution on the source fault (Wang et al. 2014a). With respect to the slip distribution, it should be noted that many models directly

prescribe the coseismic slip in a simplified way, for example, by defining the way in which the coseismic slip decreases from a maximum value in the fault centre to zero at the fault edges. Other models use the slip distributions derived from inverse modelling of geodetic data, which implies that the slip distribution highly depends on the local geological conditions and on the data coverage.

Here we present three-dimensional finite-element models to investigate – independent of a specific fault or earthquake – the general patterns of coseismic Coulomb stress changes for arrays of normal and thrust faults, respectively. Each fault array consists of a source fault in the centre and ten receiver faults located along-strike of the source fault as well as in its hanging wall and footwall. Slip on the source fault is not prescribed but evolves freely as a function of the length of the preseismic phase and the rate of regional extension or shortening. In other words, the coseismic slip on our model source fault evolves self-consistently throughout the entire model run. We use our models to perform a systematic study about the spatial distribution of the coseismic Coulomb stress change and to link these stress changes to the distribution of the coseismic strain at the model surface and at depth. Based on a series of experiments, we evaluate the effects of fault dip and dip direction (synthetic, antithetic), friction coefficient and coseismic slip on the coseismic Coulomb stress changes.

2.2 Model setup

We use three-dimensional finite-element models generated by the commercial software Abaqus (version 6.13). All models are 200 x 200 km wide and represent a 100-km-thick continental lithosphere (Fig. 2.1), which is subdivided in a 15-km-thick elastic upper crust, a 15-km-thick viscoelastic lower crust and a 70-km-thick viscoelastic lithospheric mantle. The elastic parameters (Young's modulus E , Poisson's ratio ν), the density ρ and the viscosity η of the layers are shown in Figure 2.1. Viscoelastic behaviour is implemented as linear, temperature-independent Maxwell viscoelasticity. Although this rheology represents a simplification of the actually depth-dependent and possibly non-linear viscoelastic behaviour of the lower crust and lithospheric mantle (e.g. Freed and Bürgmann 2004, Ellis et al. 2006), the implementation of viscoelastic layers itself is an advantage compared to the commonly used homogeneous elastic half-space models based on Okada (1992) because our models can be used to analyse transient Coulomb stresses caused by postseismic viscoelastic relaxation in future studies. Our models also include isostatic effects, which we simulate by applying a lithostatic pressure of $3 \cdot 10^9$ Pa and an elastic foundation to the model bottom. The property of the elastic foundation represents an asthenosphere with a density of 3200 kg/m^3 . Gravity is

included as a body force (acceleration due to gravity: $g = 9.81 \text{ m/s}^2$). The model sides in the xz -plane are fixed in the y -direction, while the bottom is free to move in the vertical and horizontal directions.

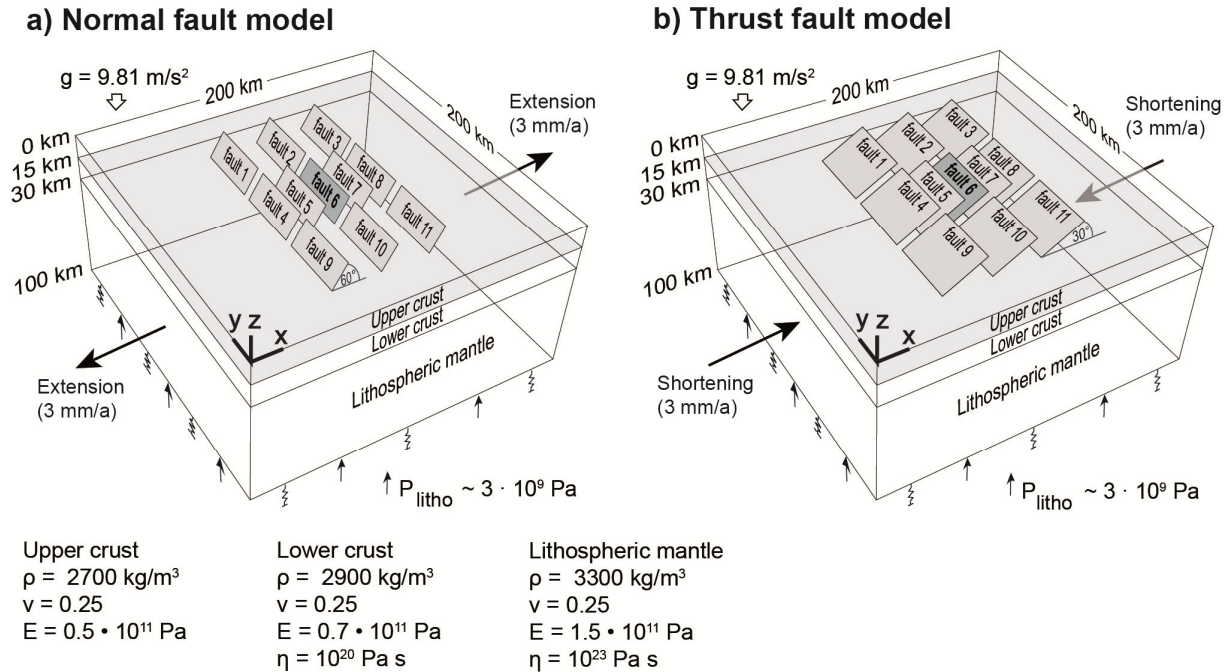


Figure 2.1: Perspective view of the three-dimensional reference models with (a) 60°-dipping normal faults and (b) 30°-dipping thrust faults. In both reference models, the lithosphere is divided into an elastic upper crust, viscoelastic lower crust and viscoelastic lithospheric mantle (rheological parameters are ρ density, E Young's modulus, ν Poisson's ratio and η viscosity). The source fault (dark grey) and the ten receiver faults (light grey) are embedded in the upper crust. In the reference models, the 40-km-long faults have a friction coefficient of $\mu = 0.6$. Gravity is included as body force. Isostatic effects are implemented by a lithostatic pressure (P_{litho} , black arrows at the model bottom) and an elastic foundation (springs) representing an asthenosphere. All model sides as well as the bottom of the model are free to move in the vertical direction. Model sides in the xz -plane are fixed in the y -direction. At the model sides in the yz -plane, a velocity boundary condition is applied in the x -direction to extend or shorten the model at a total rate of 6 mm/yr, which initiates slip on the faults.

We created two reference models with arrays of normal faults (dip: 60°; Fig. 2.1a) and thrust faults (dip: 30°; Fig. 2.1b), respectively. All faults are 40 km long and extend from the model surface to the bottom of the upper crust. The faults are modelled as frictional contact interfaces between the footwall and hanging wall of each fault. Note that no coseismic plastic deformation occurs outside of the fault zones, because the upper crust in our model behaves purely elastic. The minimum distance between the faults is 15 km in the x -direction (e.g. between faults 4 and 5) and 5 km in the y -direction (e.g. between tips of faults 1 and 4). The fault in the centre (fault 6; see Fig. 2.1) represents the source fault, which will experience the coseismic slip during the modelled earthquake cycle. The other faults in its surrounding represent the receiver faults, for which the Coulomb stress changes induced by the earthquake will be analysed (see Figure 2.1 for the spatial configuration of the receiver faults). The general distance between the faults in the x -direction is 30 km, which is a typical spacing

between faults, for example, in the Basin and Range Province (Wernicke et al. 2000). To capture the Coulomb stress changes near the source fault, we placed two additional model faults (5, 7) in the hanging wall and footwall of the source fault at a distance of 15 km. By applying a velocity boundary condition at the model sides in the yz -plane, the model either is extended or shortened at a total rate of 6 mm/a, which initiates slip on the faults. Slip initiation is controlled by the Mohr-Coulomb criterion $|\tau_{\max}| = C + \mu\sigma_n$, where τ_{\max} is the critical shear stress, C is the cohesion (zero in our model), σ_n is the normal stress and μ the friction coefficient, which has a value of 0.6 in the reference model. Additional experiments were run with a value of 0.4. These values represent intermediate coefficients of friction for intra-continental faults, which range from about 0.3 to 0.8 (Townend and Zoback 2000, Collettini et al. 2009, Hurd and Zoback 2012, Niemeijer and Collettini 2014). Apart from that, friction coefficients of 0.4 and 0.6 are commonly used in Coulomb stress calculations (e.g. Nostro et al. 1997, Lin et al. 2011, Ryder et al. 2012), which facilitates the comparison with these previous studies. In contrast, the friction coefficient may approach zero on mature plate boundary faults with large displacements, such as the San Andreas fault (e.g. Chéry et al. 2004, Coble et al. 2014). The model is meshed by linear tetrahedral elements with an approximate edge length of 1 km near the faults. Away from the faults, the element edge length increases to 3 km.

A model run consists of quasi-static analysis steps. First, isostatic equilibrium is established. Afterwards, the extension or shortening of the model starts, which continues during all following model steps. In the initial model phase (i.e. before the earthquake cycle), the faults are unlocked and accumulate slip until they have reached a constant slip rate (cf. Hampel and Hetzel 2012, Hampel et al. 2013). The earthquake cycle then starts with a preseismic phase, in which all faults are locked while extension or shortening of the model continues. In the following coseismic phase, we unlock the source fault (fault 6), which results in sudden slip (= model earthquake) of 2 m, which represents an $M_w \approx 7$ earthquake on the 40-km-long model fault (cf. Wells and Coppersmith 1994). Note that the coseismic slip on the source fault develops freely (i.e. is not prescribed on the fault plane) and has an elliptical distribution with a maximum slip of 2 m in the reference model. All changes between locked and unlocked states of the faults are achieved by changing the boundary conditions on the fault planes (Abaqus Keywords *ROUGH and *FRICTION) (cf. Hampel and Hetzel 2012, 2015). The size of the earthquake is controlled by the applied far-field extension/shortening rate, the duration of the preseismic phase and the friction coefficient of the source fault plane. No coseismic plastic deformation occurs outside of the fault zones, because the upper crust in

our model behaves purely elastic. Apart from the two reference models, we also ran experiments with blind thrust and normal faults, a friction coefficient $\mu = 0.4$, a coseismic slip of 1 m, 45°-dipping faults and antithetic receiver faults, respectively. Note that the change in dip direction was realized such that position of the synthetic and antithetic receiver faults is the same at a depth of 7.5 km.

2.3 Model results

2.3.1 Coseismic displacement fields in the normal and thrust fault reference models

Figure 2.2 shows the vertical and total horizontal coseismic displacement of the model surface and the coseismic slip on the source fault plane (fault 6) obtained from the normal (Fig. 2.2a, c, e, g) and thrust (Fig. 2.2b, d, f, h) fault reference models. In the normal fault model, subsidence occurs in the hanging wall, whereas uplift is observed in the footwall (Fig. 2.2a). In the thrust fault model, the coseismic vertical displacement shows mainly uplift of the hanging wall and minor subsidence in the footwall (Fig. 2.2b). The total horizontal

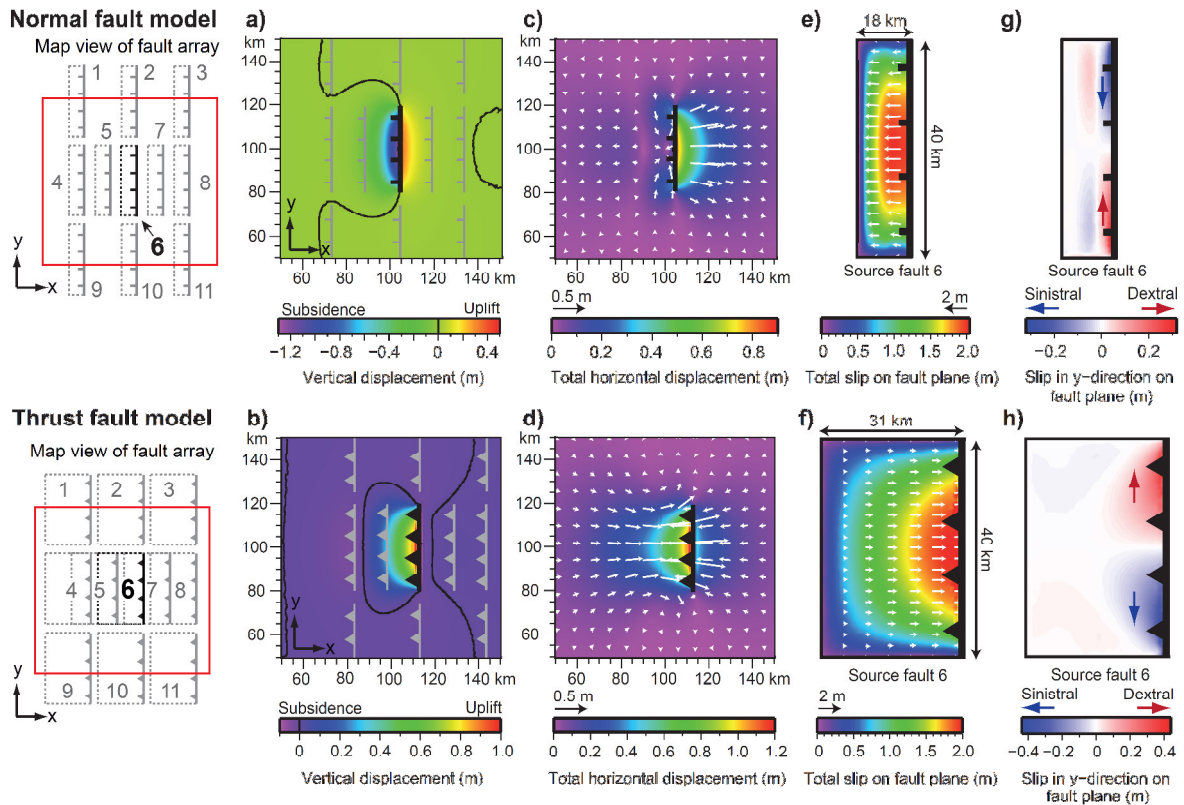


Figure 2.2: Coseismic displacements in the normal and thrust fault reference models shown in map view for the central part of the model surface (indicated by red box). (a, b) Vertical displacement. For reference, the location of the receiver faults is also shown. (c, d) Total horizontal displacement (shown by colour-code and as white arrows). (e, f) Total coseismic slip on the source fault (fault 6). (g, h) Coseismic slip in the y-direction (i.e. parallel to the fault's strike) on the source fault.

displacement is highest in the footwall of the normal fault model (Fig. 2.2c) and in the hanging wall of the thrust fault model (Fig. 2.2d). Although the total horizontal displacement is dominated by movements in the x-direction, there are also significant movements in the y-direction (i.e. parallel to the strike of the faults) in the areas around the tips of the source fault. As a consequence, the total displacement vectors in the hanging wall and footwall of the source fault either point toward or radially away from each other (Fig. 2.2c, d). On the fault plane of the surface-breaking source fault, a typical elliptical slip distribution develops, with a maximum displacement of 2 m and zero displacement at the fault tips and edges (Fig. 2.2e, f). The slip distribution shows a strike-slip motion in the upper part of the fault plane, with contrasting sense of movement in the normal and thrust fault models (Fig. 2.2g, h).

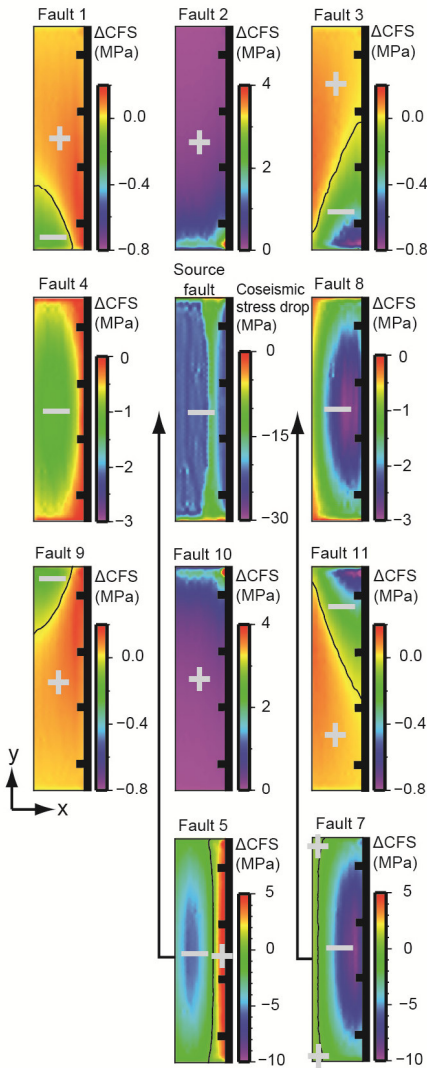
2.3.2 Coseismic (= "static") Coulomb stress changes

In all models, the coseismic slip on fault 6 leads to Coulomb stress changes on the receiver fault planes, which range from a few bar to several MPa (Figs. 2.3-2.8). Both positive and negative Coulomb stress changes are observed. The change in the sign can occur both along-strike of the fault as well as in down-dip direction. Note that we have calculated the Coulomb stress changes assuming that a positive stress change promotes slip on the receiver fault in the direction of slip of the source fault. As our Coulomb stress calculations do consider both, the coseismic stress change and the background stress, a negative Coulomb stress change implies that slip on the receiver fault in the slip direction of the source fault is hampered, including the possibility that the receiver fault may experience the opposite sense of slip compared to the source fault (cf. Asano et al. 2011). Additional model runs with unlocked receiver faults showed that the negative Coulomb stress changes in our models are not large enough to activate the receiver faults with a slip sense opposite to the source fault.

In all models (Figs. 2.3-2.8), faults located in the hanging wall and footwall of the source fault (faults 4-8) experience primarily negative Coulomb stress changes with a symmetric distribution on each fault plane. Only receiver faults close to the source fault show significant positive stress changes in some parts of their fault plane. Faults 2 and 10 positioned in the along-strike prolongation of the source fault undergo exclusively positive Coulomb stress changes and the changes are largest at the fault tip that is closer to the source fault, resulting in an asymmetric Coulomb stress change distribution. Receiver faults 1, 3, 9 and 11 show mostly positive Coulomb stress changes, except for an area closer to the source fault where high values of negative stress changes occur. As a consequence, these faults show an asymmetric stress change distribution. Note that the distribution of Coulomb stress changes

on fault 1, 2 and 3 are mirror images to fault 9, 10 and 11. In the following, we will describe the Coulomb stress patterns obtained from the different normal and thrust fault models in more detail.

a) Normal fault reference model



b) Thrust fault reference model

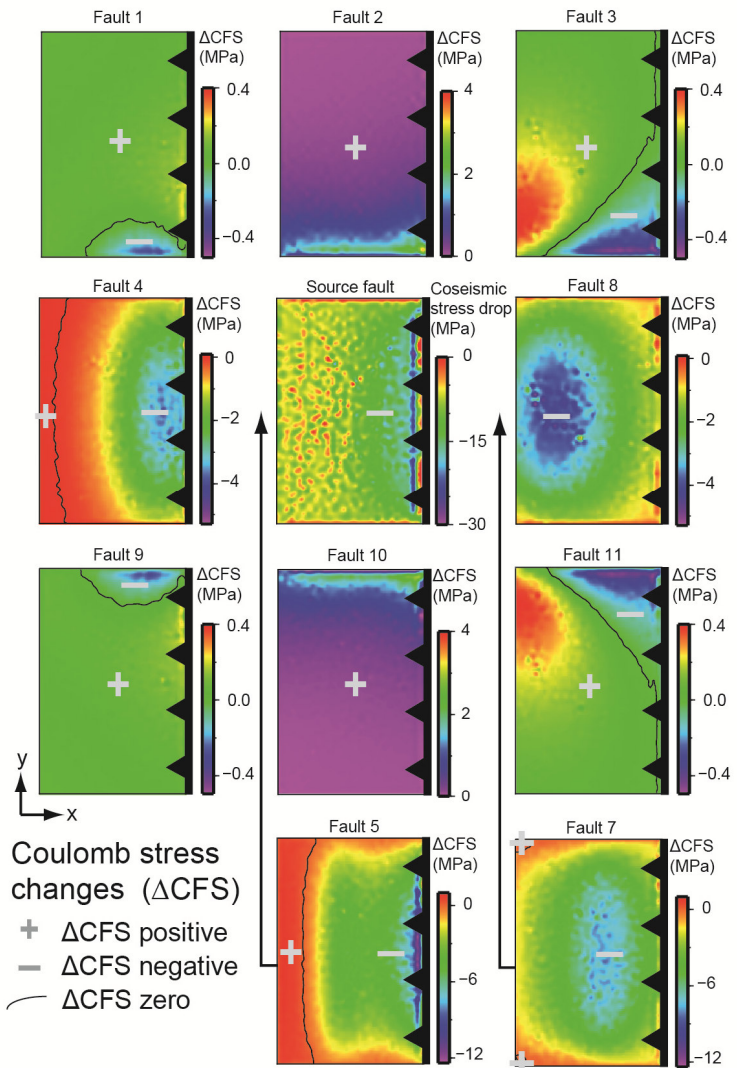


Figure 2.3: Coseismic Coulomb stress changes (ΔCFS) on the fault planes 1 to 11 in map view for the (a) normal fault and (b) thrust fault reference model. Note that the distance between the fault planes is not to scale. The real distance between the surface traces of the faults is 30 km in the x-direction and 5 km in the y-direction. Four different colour scales are used for the Coulomb stress changes, with scales being the same for faults 1, 3, 9 and 11, for faults 4 and 8, for faults 5 and 7 and for faults 2 and 10, respectively. Areas of positive Coulomb stress change (+) and negative stress change (-) are separated by a black line where $\Delta CFS = 0$.

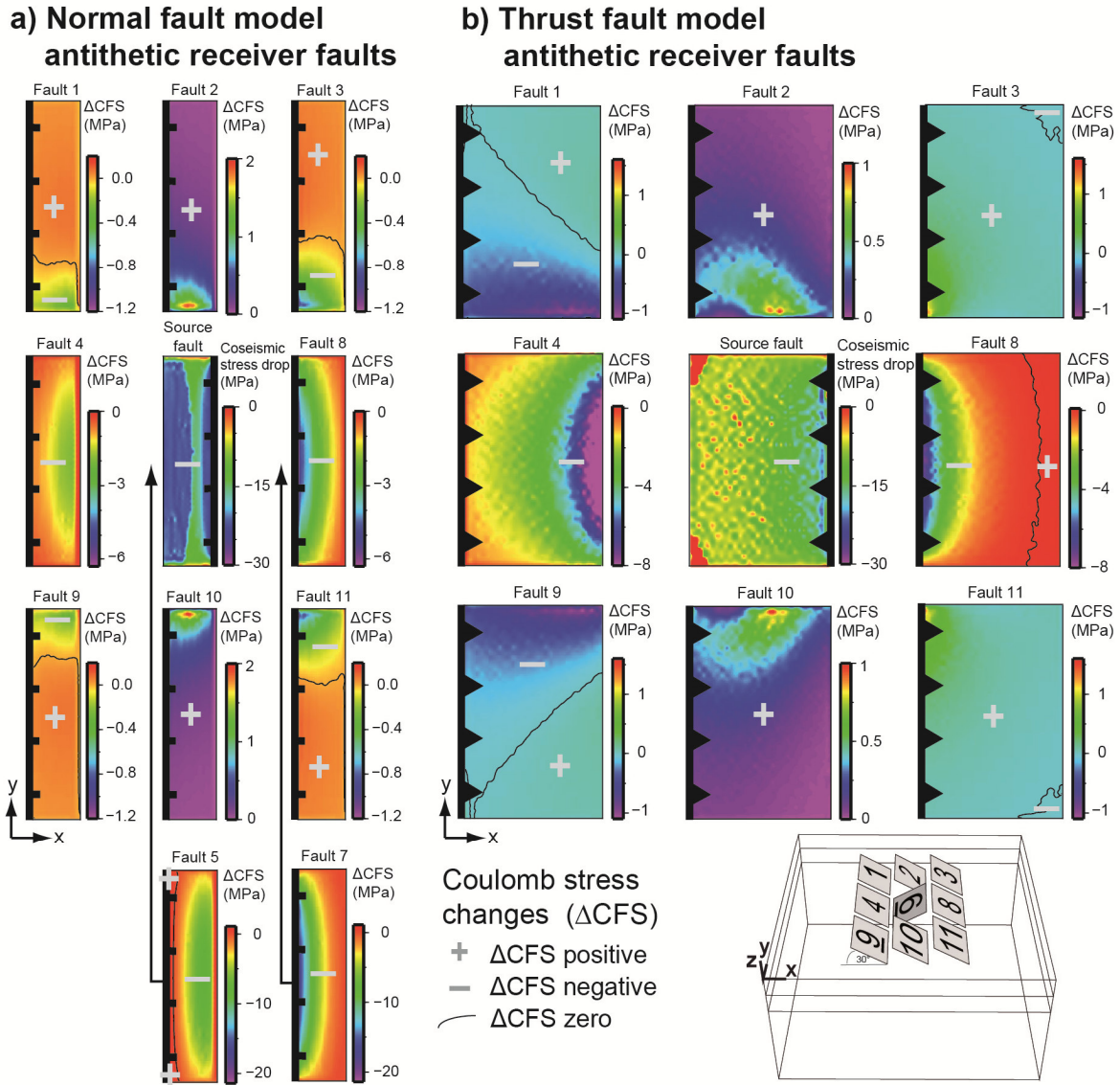


Figure 2.4: Coseismic Coulomb stress changes (ΔCFS) on the fault planes 1 to 11 in map view for the (a) normal fault and (b) thrust fault model with antithetic receiver faults. The distance between the fault planes is not to scale (note that the thrust fault model does not contain faults 5 and 7 because they would intersect with neighbouring faults; the configuration of the antithetic thrust faults is shown in the inset map). Four different colour scales are used for the Coulomb stress changes, with scales being the same for faults 1, 3, 9 and 11, for faults 4 and 8, for faults 5 and 7 and for faults 2 and 10, respectively. Areas of positive Coulomb stress change (+) and negative stress change (-) are separated by a black line where $\Delta CFS = 0$.

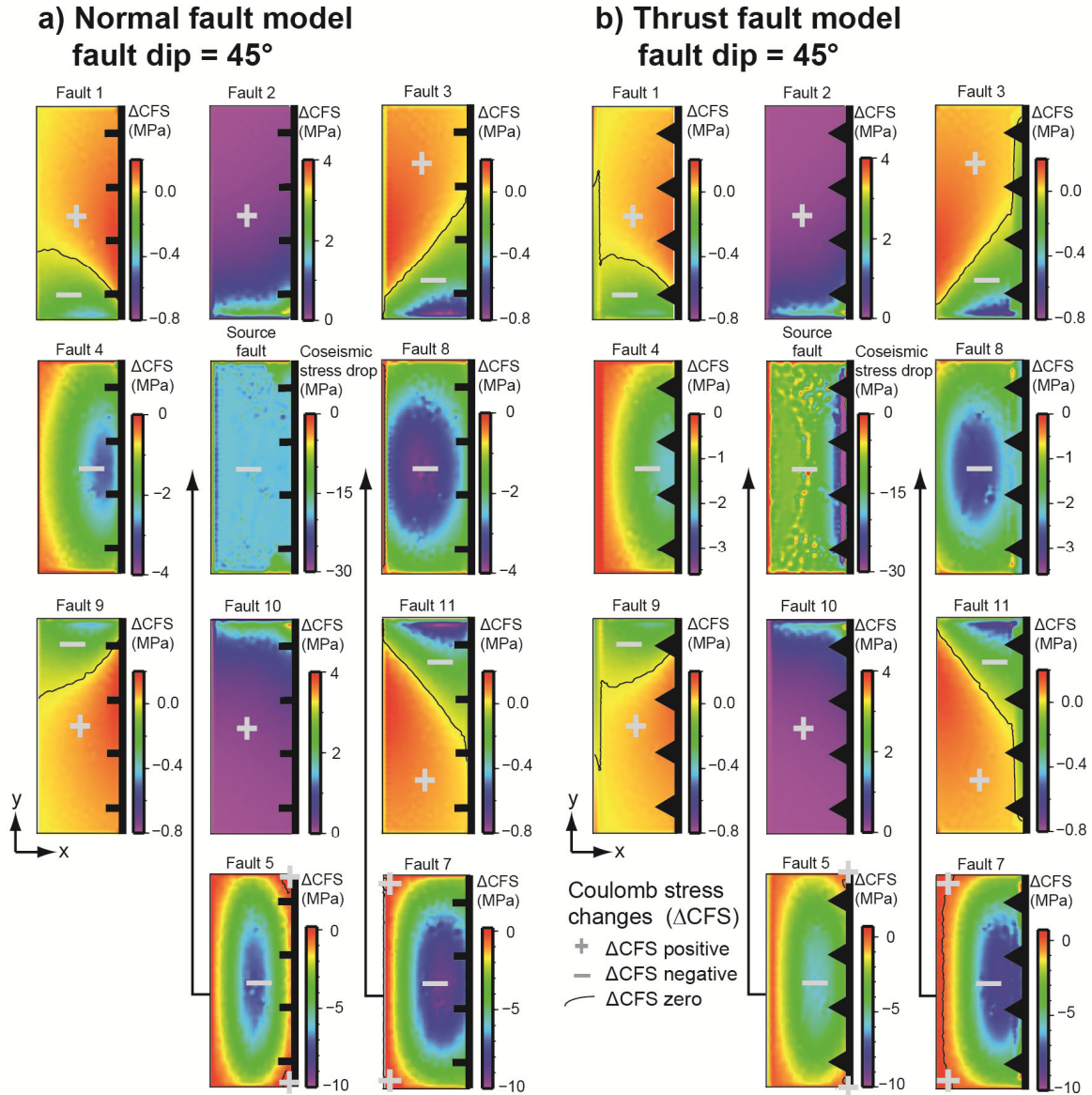
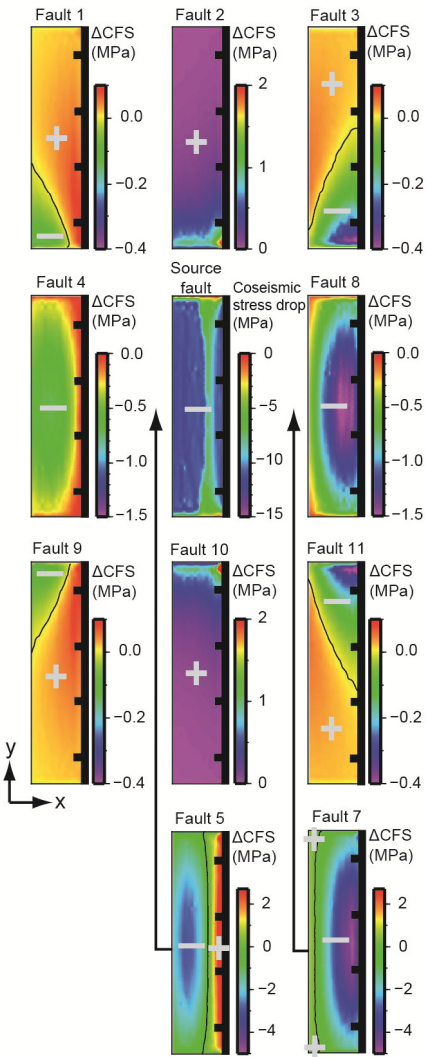


Figure 2.5: Coseismic Coulomb stress changes (ΔCFS) on the fault planes 1 to 11 in map view for the (a) normal fault and (b) thrust fault model with 45°-dipping receiver faults. The distance between the fault planes is not to scale to allow a better visualisation. Four different colour scales are used for the Coulomb stress changes, with scales being the same for faults 1, 3, 9 and 11, for faults 4 and 8, for faults 5 and 7 and for faults 2 and 10, respectively. Areas of positive Coulomb stress change (+) and negative stress change (-) are separated by a black line where $\Delta CFS = 0$.

a) Normal fault model
coseismic slip = 1m



b) Thrust fault model
coseismic slip = 1m

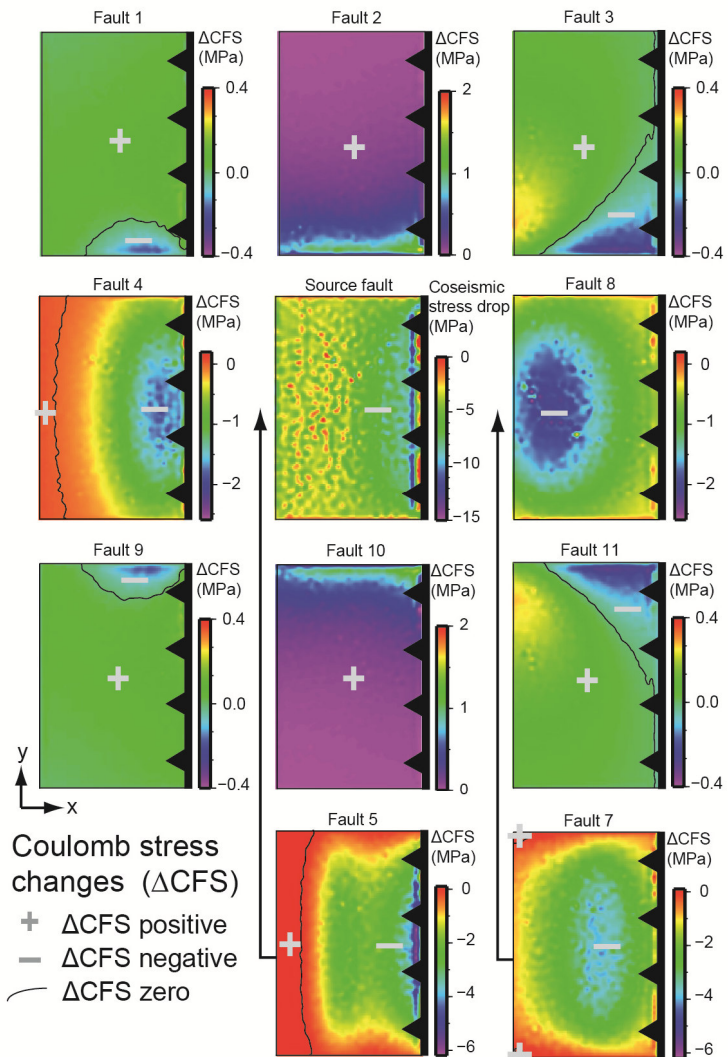
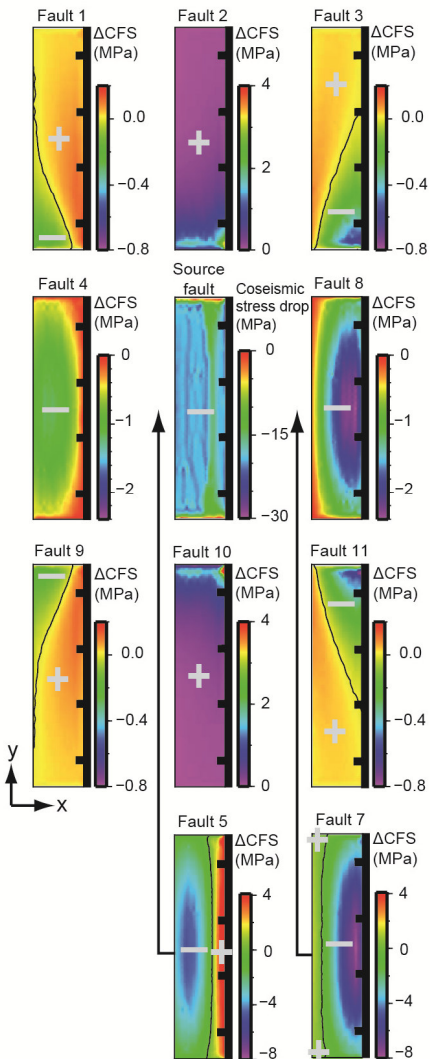


Figure 2.6: Coseismic Coulomb stress changes (ΔCFS) on the fault planes 1 to 11 in map view for the (a) normal fault and (b) thrust fault model with a coseismic slip of 1 m. The distance between the fault planes is not to scale to allow a better visualisation. Four different colour scales are used for the Coulomb stress changes, with scales being the same for faults 1, 3, 9 and 11, for faults 4 and 8, for faults 5 and 7 and for faults 2 and 10, respectively. Areas of positive Coulomb stress change (+) and negative stress change (-) are separated by a black line where $\Delta CFS = 0$.

a) Normal fault model
friction coefficient $\mu = 0.4$



b) Thrust fault model
friction coefficient $\mu = 0.4$

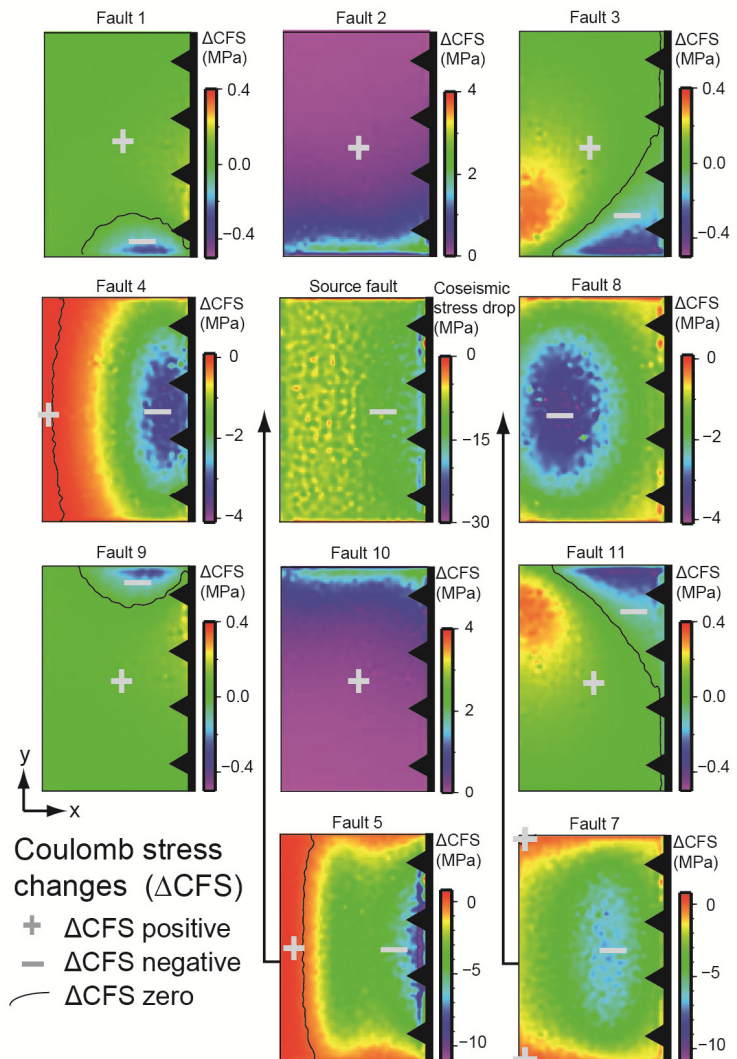


Figure 2.7: Coseismic Coulomb stress changes (ΔCFS) on the fault planes 1 to 11 in map view for the (a) normal fault and (b) thrust fault model with a friction coefficient of $\mu = 0.4$. The distance between the fault planes is not to scale to allow a better visualisation. Four different colour scales are used for the Coulomb stress changes, with scales being the same for faults 1, 3, 9 and 11, for faults 4 and 8, for faults 5 and 7 and for faults 2 and 10, respectively. Areas of positive Coulomb stress change (+) and negative stress change (-) are separated by a black line where $\Delta CFS = 0$.

a) Blind normal fault model

b) Blind thrust fault model

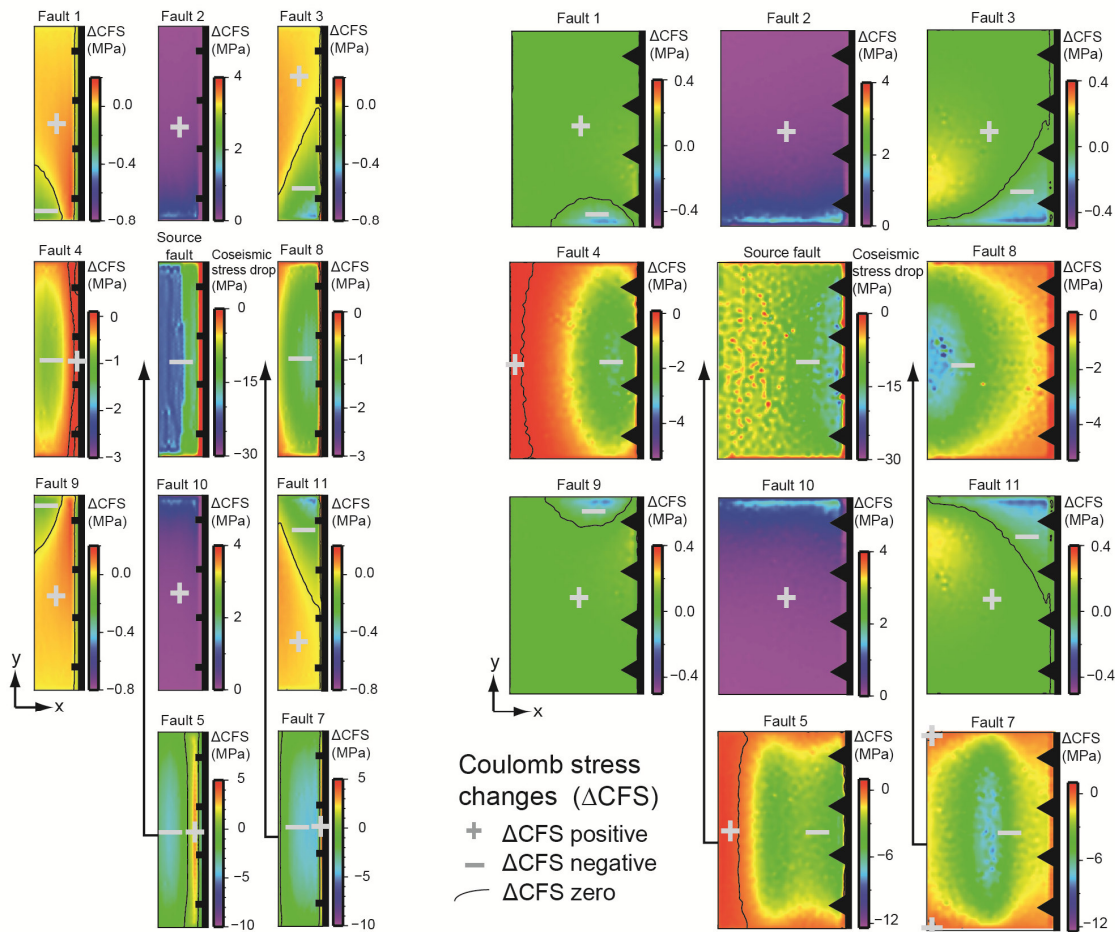
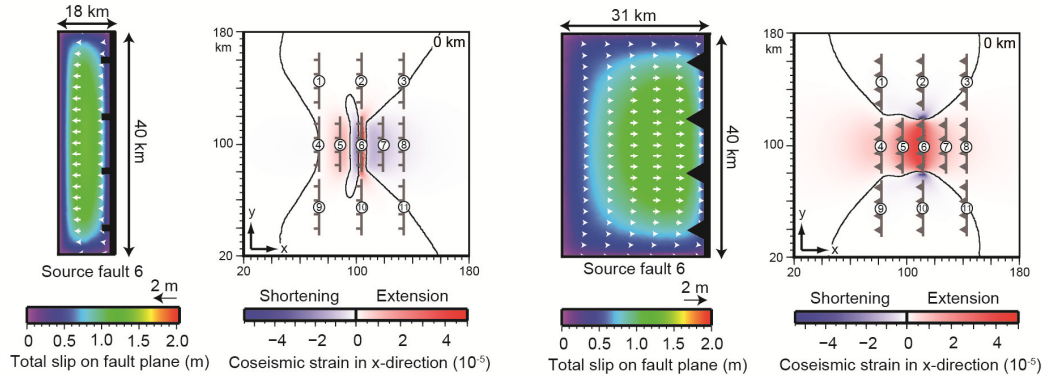


Figure 2.8: Results from models with (a) blind normal faults and (b) blind thrust faults. Shown are in the upper row the total coseismic slip on the source fault plane (fault 6) (shown by colour-code and as white arrows) and the coseismic horizontal strain in x-direction at the model surface. Note that only a part of the model surface is shown. Areas of extension and shortening are shown in red and blue, respectively. Black line marks the location of zero coseismic strain. Lower part of figure shows the coseismic Coulomb stress changes (ΔCFS) on the fault planes 1 to 11 in map view. The distance between the fault planes is not to scale to allow a better visualisation. Four different colour scales are used for the Coulomb stress changes, with scales being the same for faults 1, 3, 9 and 11, for faults 4 and 8, for faults 5 and 7 and for faults 2 and 10, respectively. Areas of positive Coulomb stress change (+) and negative stress change (-) are separated by a black line where $\Delta CFS = 0$.

2.3.2.1 Normal fault models

In the normal fault reference model (fault dip: 60° ; synthetic receiver faults; coseismic slip: 2 m; $\mu = 0.6$), the source fault shows a coseismic stress drop of up to 24.6 MPa (Fig. 2.3a). Of all receiver faults, fault 5, which is located 15 km away from the source fault in its hanging wall, shows the maximum increase in Coulomb stress of up to 5.1 MPa. Similarly, high positive stress changes of up to 4 MPa are observed on faults 2 and 10, whose fault planes are completely located in a stress triggering zone. The highest stress increase occurs in the area that is closest to the source fault. Fault 7 also shows an increase in coseismic Coulomb stress with more than 1 MPa in the lower part of the fault. On faults 1, 3, 9 and 11, the stress increases by up to 0.16 MPa. Note that the highest values are found in the upper part of the receiver faults 1 and 9, whereas the maximum stress increase on faults 3 and 11 occurs in the lower part of their fault planes. All four faults also show areas with negative Coulomb stress changes of up to -0.8 MPa. On fault 4 and 8, negative Coulomb stress changes occur with maximum values of -1.4 MPa and -2.9 MPa, respectively. The areas with the largest decrease in Coulomb stress of all receiver faults are found in the lower area of fault 5 (-5.7 MPa) and in the shallow area of fault 7 (-9.6 MPa).

The thrust and normal models with 45° -dipping faults generally show similar Coulomb stress patterns as the reference models (Fig. 2.5a). In detail, some differences are recognizable with respect to the distribution of positive and negative Coulomb stress changes. For example, the stress shadow zones on faults 1 and 9 reach the top edge of the fault, which is not the case in the normal fault reference model. With a dip of 45° , fault 5 shows only two areas of positive stress changes at its tips, whereas in the reference model the top edge of the receiver fault 5 is completely located in a stress triggering zone. If the coseismic slip is reduced to 1 m (i.e. half of the coseismic slip in the reference models), the Coulomb stress changes also decrease by $\sim 50\%$ (Fig. 2.6a). A lower friction coefficient ($\mu = 0.4$) reduces the Coulomb stress changes by up to $\sim 30\%$ (Fig. 2.7a). Faults 5 and 7 show maximum values that are 1 and 1.7 MPa lower than to the reference model, whereas the differences in the stress change on fault 2, 8 and 10 is on the order of 0.5-0.7 MPa. The differences on the other faults are less than ~ 0.1 MPa.

In an experiment with blind normal faults (maximum coseismic slip: 1.4 m) the spatial distribution of the Coulomb stress change considerably differs from the normal fault reference model, especially in the upper part of the fault planes (Fig. 2.8a). In the upper part of faults 4 and 7, small stress triggering zones arise with Coulomb stress changes up to 0.09 MPa (fault 4) and 0.3 MPa (fault 7), whereas the surface area of the fault 1, 5 and 9 exhibit small

stress shadow zones. The zone of highest Coulomb stress increase (3.6 MPa) is located at fault 5 in the upper area of the fault plane, in contrast to the normal fault reference model.

The models with antithetic receiver faults (Fig. 2.4a) show that the dip orientation changes both the magnitude and distribution of the Coulomb stress changes. Compared to the reference model, the largest differences regarding the stress change distribution occur on fault 7 and faults 1, 3, 9 and 11. Whereas the synthetic receiver fault 7 exhibits a zone of positive Coulomb stress change, the antithetic receiver fault is completely located in a stress shadow zone. For antithetic faults 1, 3, 9 and 11, the transition between the negative and positive Coulomb stress changes (zero line) is oriented perpendicular to the fault's strike. The zone of positive Coulomb stress changes in the surface area of fault 5 occurs both on the synthetic and antithetic fault.

2.3.2.2 Thrust fault models

The source fault in the thrust fault reference model (fault dip: 30°; synthetic receiver faults; coseismic slip: 2 m; $\mu = 0.6$) experiences a coseismic stress drop of up to 28.4 MPa (Fig. 2.3b). Faults 2 and 10 are completely located in stress triggering zones with Coulomb stress changes up to 3.5 MPa. Faults 1, 3, 9 and 11 are divided in zones with positive (up to 0.4 MPa) and negative (up to -0.5 MPa) Coulomb stress changes. Compared to the normal fault reference model, the zones with decrease in stress on thrust faults 1 and 9 are closer to the surface. The synthetic receiver faults in the hanging wall and footwall of the source fault are mostly located in stress shadow zones with maximum negative stress changes ranging from -4.1 MPa (fault 4) to -12.3 MPa (fault 5). In the lower part of the fault planes 4 and 5, zones of positive Coulomb stress changes of up to 0.1 and 0.9 MPa, respectively, exist.

In the experiment with 45°-dipping thrust faults, the overall pattern of the stress changes is similar to the reference model (Fig. 2.5b). Notable differences exist on faults 4 and 5, whose lower parts are located in a stress shadow zone while slightly positive values are observed in the respective areas in the reference models. Also, the size of the areas with high positive stress changes on faults 1, 3, 9 and 11 decreases for a dip of 45°. As for the normal faults, a reduction of the coseismic slip to 1 m leads to a ~50% decrease of stress change magnitudes (Fig. 2.6b). In the experiment with a friction coefficient of $\mu = 0.4$, the magnitude of the Coulomb stress changes is reduced by up to ~20% compared to the reference model (Fig. 2.7b). The largest differences in the stress change exist on faults 5, 7 and 8 (~1 MPa) and on faults 2, 4 and 10 (0.1-0.6 MPa). The differences on the other faults are less than 0.1 MPa.

In the blind thrust fault model (maximum coseismic slip: 1.3 m), the Coulomb stress change distribution slightly differs from the thrust fault reference model (Fig. 2.8b). All significant stress triggering and shadow zones also exist as in the reference model. In detail, the stress shadow zone of fault 1 and 3 reaches the surface at the fault tip near to the source fault and the location of highest stress increase on fault 8 is at greater depth than in the thrust fault reference model.

A change to an antithetic dip direction of the thrust faults (Fig. 2.4b) leads to more pronounced modifications in the Coulomb stress distribution than in the model with normal faults (note that faults 5 and 7 are excluded from the array with antithetic faults because the fault planes would intersect with the neighbouring faults). Thrust faults 3 and 11 are located almost completely in stress triggering zones. Faults 1 and 9 show an asymmetric Coulomb stress distribution with a large area of negative Coulomb stress changes up to -1.1 MPa while the size of the area with positive stress changes (≤ 0.1 MPa) has become smaller. In contrast to the synthetic fault 4, which showed positive and negative stress changes, the antithetic fault 4 is completely located in a stress shadow zone. Fault 8, on the contrary, shows a zone of positive stress changes in its lower part, which was not present in the model with synthetic faults.

2.4 Discussion

2.4.1 General patterns of Coulomb stress changes and influence of different parameters

Our study about fault interaction on intra-continental normal and thrust faults reveals the general patterns of coseismic Coulomb stress changes that are induced on the surrounding receiver faults by the earthquake on the source fault. On most faults, the magnitude of the stress changes is in the range of a few percent of the coseismic stress drop on the source fault, which is on the order of 20-30 MPa, in agreement with values derived for strong natural earthquakes on intra-continental faults (e.g. Hanks 1977, Kanamori and Anderson 1975, Scholz 2002). Higher positive and negative stress changes of a few MPa occur on faults 2, 5, 7 and 10 because they are located close to the source fault.

The distribution of the coseismic Coulomb stress changes are strikingly similar for thrust and normal faults, which is best seen in the models with 45°-dipping faults (Fig. 2.5). For both faults, primarily negative Coulomb stress changes occur on faults in the hanging wall and footwall of the source fault, whereas receiver faults along-strike of the source fault experience exclusively positive stress changes. Mixed distributions occur on faults 1, 3, 9

and 11. If normal and thrust faults have dips of 60° and 30° , respectively (Fig. 2.3), the stress distribution significantly changes on most receiver faults, which implies that the dip of the receiver faults is one of the parameters that strongly controls the Coulomb stress changes. More specifically, a change in the dip can alter the size of the areas with positive and negative stress changes or place a fault plane, which would otherwise experience both positive and negative stress changes, entirely in a stress-triggering or stress-shadow zone. For example, the 45° -dipping normal fault 5 undergoes only a small stress increase at the fault tips whereas the 60° -dipping normal fault 5 experiences a high stress increase at the surface (Figs. 2.5a, 2.3a). For both normal and thrust faults, the stress changes on the individual receiver fault planes also strongly depend on their position relative to the source fault. Our results further reveal that the influence of the earthquake does not decrease in a simple manner with increasing distance from the source fault but that the magnitude of the Coulomb stress changes varies both along-strike of the receiver faults and with depth. This is in general agreement with previous studies that evaluated stress patterns for different configurations based on specific natural fault arrays, although a direct comparison is hindered by the differences in the coseismic slip, the fault geometry, and/or the ways of visualizing the results (e.g. Lin et al. 2011, Nostro et al. 1997, 2001, Ryder et al. 2012). For example, Nostro et al. (1997, 2001) and Ryder et al. (2012) calculated maps of Coulomb stress changes at 7 km and 7.5 km depth, respectively, caused by a normal faulting earthquake. Both author teams obtain two major lobes of positive Coulomb stress changes around the tips of the source fault and two major lobes of negative stress changes in the hanging wall and footwall of the source fault. Our model results show, however, that a normal fault located close to the source fault in its hanging wall can experience high positive Coulomb stress changes along its entire surface trace (fault 5 in Fig. 2.3a). A small zone of positive stress change is present in the cross-sections shown by Nostro et al. (1997) and Ryder et al. (2012), however, the profiles do not allow specifying the lateral extent. Coulomb stress changes for some synthetic and antithetic configurations of 45° -dipping thrust faults were analysed by Lin et al. (2011). Their results shown in map view at 10 km depth and along profiles across the faults generally agree with our models but also show important differences. For example, Lin et al. (2011) obtain for both synthetic and antithetic receiver faults zones of positive Coulomb stress changes in the hanging wall and to a lesser extent also in the footwall of the source fault, which are not present in our models (Figs. 2.4b, 2.5b, 2.8b). The differences cannot be explained by the different positions of our receiver faults compared to Lin et al. (2011) because our modelled coseismic strain fields (Figs. 2.10c-d, 2.11c-d) show that the entire hanging wall and footwall

around source fault 6 undergoes coseismic extension almost down to the bottom of the upper crust, which would ultimately cause negative Coulomb stress changes on any receiver fault located in this area (see Chapter 2.4.2 below). Rather, we speculate that the difference arises from the fact that Lin et al. (2011) define a rectangular, tapered slip distribution with zero slip at all four model edges, while our model includes a surface-breaking or blind faults with an elliptical slip distribution (Figs. 2.2, 2.8). Altogether, our results underline that both the magnitude and sign of the Coulomb stress changes cannot easily be extrapolated between different depth levels and that the calculation of stress changes for individual fault planes can reveal important details in the Coulomb stress changes.

Apart from the position of the receiver fault and their dip, the dip direction also plays a role for the distribution of the Coulomb stress changes. With the change from a synthetic to antithetic dip direction (Figs. 2.3, 2.4), a reversal of the sign or a significant increase or decrease of the stress change can occur on the fault planes (e.g. normal faults 5 and 7; thrust faults 4 and 8). The effect is more pronounced on thrust faults than on normal faults. Nevertheless, the general pattern with zones of positive stress change on receiver faults in the hanging wall and footwall of the source fault and negative stress changes on faults along-strike of the source fault is also present in the antithetic fault models. This finding is in agreement with the results by Lin et al. (2011) and Ryder et al. (2012) for configurations with antithetic receiver faults.

In contrast to the dip and dip direction, a change in the coseismic slip or in the friction coefficient primarily affects the magnitude of the Coulomb stress changes and only to a lesser extent their spatial distribution. A decrease in both parameters leads to a decrease both of the coseismic stress drop and the Coulomb stress changes on the receiver faults. In case of a lower coseismic slip, this can be explained by the fact that the short-term response is dominated by the elastic layer, in which case the stress change scales linearly with the coseismic slip. In other words, for triggering an earthquake with only 1 m of slip less time (50%) is needed for the preseismic stress build-up than in the model with 2 m of slip. Therefore, the preseismic stress build-up as well as the coseismic stress release at the source and the Coulomb stress changes on receiver faults are reduced by 50%. A lower friction coefficient leads to lower Coulomb stress changes because the resistance to coseismic slip is reduced. Therefore, the coseismic stress drop on the source fault is lower, which implies that also the Coulomb stress changes on the receiver faults are smaller. These findings support the results by Wang et al. (2014a) who identified the dip, the amount of coseismic slip and the

friction coefficient as the main parameters that control the Coulomb stress changes caused by the 2008 Wenchuan earthquake.

In our model, the upper crust is purely elastic and no plastic deformation occurs outside of the source fault plane. We speculate that if part of the coseismic deformation was taken up by plastic deformation of the crust, this would reduce the amount of coseismic slip on the source fault if all other parameters remain unchanged. With less slip, the Coulomb stress changes should become lower on the receiver faults (cf. Fig. 2.6). On the other hand, the plastic deformation in the crust might weaken the rocks in the surrounding of the source fault and locally modify the principal stresses (e.g. Chéry et al. 2004), which might bring other faults closer to failure.

All our modelled Coulomb stress changes arise from idealized coseismic slip distributions, which are free from the individual heterogeneities that would arise in nature, e.g. from the specific earthquake rupture process, local variations in rock strength and frictional properties. Hence our results provide a basis for identifying deviations from the general Coulomb stress changes if, for example, local geological conditions lead to a more heterogeneous slip distribution. For example, we would expect shifts of the Coulomb stress change maxima and minima for an asymmetric slip distribution, as derived for the 2009 L'Aquila earthquake (e.g. Cheloni et al. 2010, Serpelloni et al. 2012).

2.4.2 Correlation between static stress changes and coseismic displacement and strain fields

Our modelled static Coulomb stress changes can be explained in the light of the coseismic displacement and strain fields (Figs. 2.2, 2.10). Note that the distribution of the coseismic strain caused by the earthquake on source fault 6 does not depend on the number of faults present in the models, despite the differences in the cumulative vertical displacement fields (for details see Figure 2.9; see also Hampel and Hetzel (2015, their Figure 2.2)). Although the coseismic displacement fields are fundamentally different for normal and thrust faults (Fig. 2.2), slip on both types of faults is mostly inhibited if the receiver faults are located directly in the hanging wall and footwall of the source fault, because the coseismic displacements in the upper crust generally counteract the sense of slip on the receiver faults. This is also evident from the coseismic strain fields, which show co-existing domains of extension and shortening in both models (Fig. 2.10) (e.g. Hampel and Hetzel 2015).

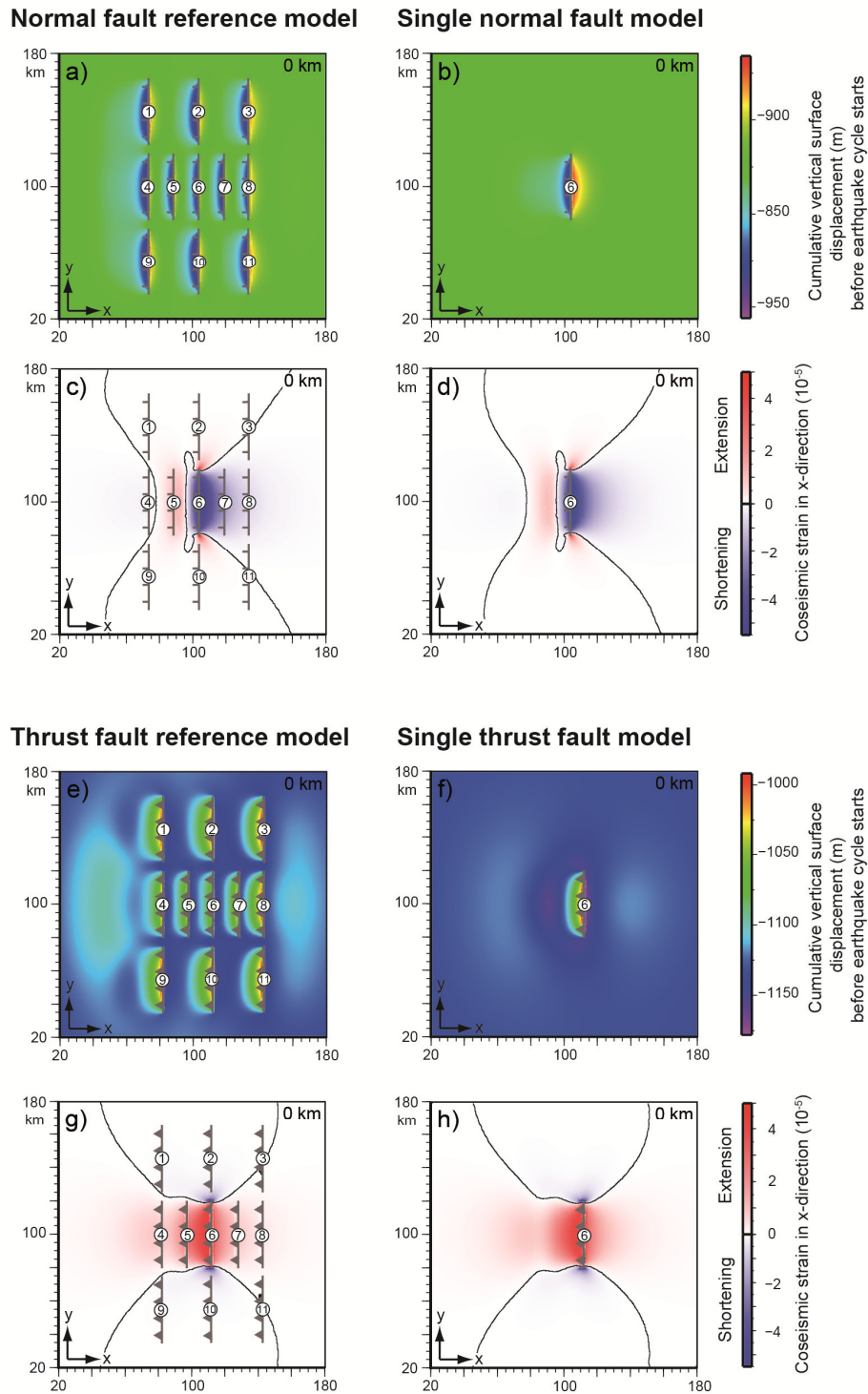


Figure 2.9: Comparison between the reference models and „single-fault“ models, in which only fault 6 is active while slip accumulation on all other faults is prohibited. All other model parameters and boundary conditions are the same in both models. Cumulative vertical displacements at the model surface before the earthquake cycle starts in (a) the normal fault reference model and (b) the single normal fault model. Coseismic horizontal strain in x-direction at the model surface in (c) the normal fault reference model and (d) the single normal fault model. Cumulative vertical displacements at the model surface before the earthquake cycle starts in (e) the thrust fault reference model and (f) the single thrust fault model. Coseismic horizontal strain in x-direction at the model surface in (g) the thrust fault reference model and (h) the single thrust fault model. In the figures showing the coseismic strain (c, d, g, h) the areas of extension and shortening are shown in red and blue, respectively. Black line marks the location of zero coseismic strain. In all figures the positions of the faults are indicated by normal and thrust fault map symbols and fault numbers. Note that only a part of the model surface is shown.

In the normal fault model, domains of extension (positive strain) and shortening (negative strain) spatially correlate with positive and negative Coulomb stress changes, respectively. In the thrust fault model, the opposite holds, i.e. positive and negative Coulomb stress changes are associated with shortening and extension, respectively. In particular, the high negative Coulomb stress changes observed on receiver faults located in the hanging wall and footwall of the source fault can be related to areas of horizontal shortening (normal fault model) and extension (thrust fault model). In the normal fault model, horizontal shortening attains values of about $-5 \cdot 10^{-5}$ in the footwall of the source fault, whereas in the thrust fault model the maximum values of horizontal extension ($\sim 5 \cdot 10^{-5}$) occur in the hanging wall. The strain distribution also explains why normal fault 5 exhibits a positive Coulomb stress change in its upper part (Fig. 2.3a): it is located in a shallow zone of extensional strain between zones of

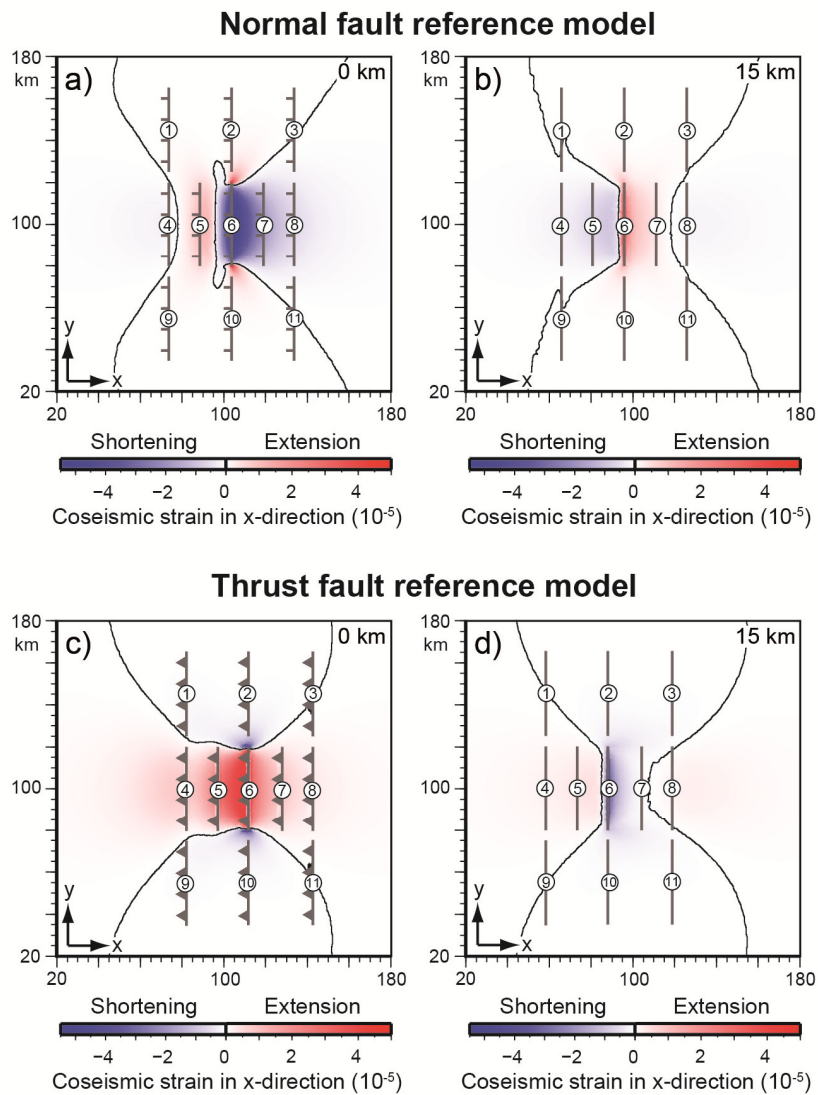


Figure 2.10: Coseismic horizontal strain in x-direction in the normal fault reference model (a) at the surface and (b) at 15 km depth and in the thrust fault reference model (c) at the surface and (d) at 15 km depth. Note that only a part of the model is shown. Areas of extension and shortening are shown in red and blue, respectively. Black line marks the location of zero coseismic strain. The position of the faults at depth is indicated by black lines with fault numbers.

shortening. For a fault dip of 45° , the zones of shortening are connected, with the consequence that extension and positive Coulomb stress changes occur only near the fault tips (Figs. 2.5a, 2.12a). Regardless of the type of fault (normal or reverse, surface-breaking or blind), its dip or dip direction, our models indicate that Coulomb stress changes greater than 0.1 MPa can be expected in areas where the coseismic strain at the surface exceeds absolute values of $\sim 0.4 \cdot 10^{-7}$ to $\sim 2 \cdot 10^{-7}$. Near the tips of the source fault, zones of large extensional strain ($5 \cdot 10^{-5}$; normal fault model) and large contractional strain ($-3.5 \cdot 10^{-5}$; thrust fault model) are observed throughout the upper crust (Figs. 2.10, 2.11). As a consequence, slip is promoted on receiver faults located in these areas (faults 2, 10), which are hence completely located in stress-triggering zones. As the total amount of strain decreases with increasing distance from the source fault, the magnitude of the stress change

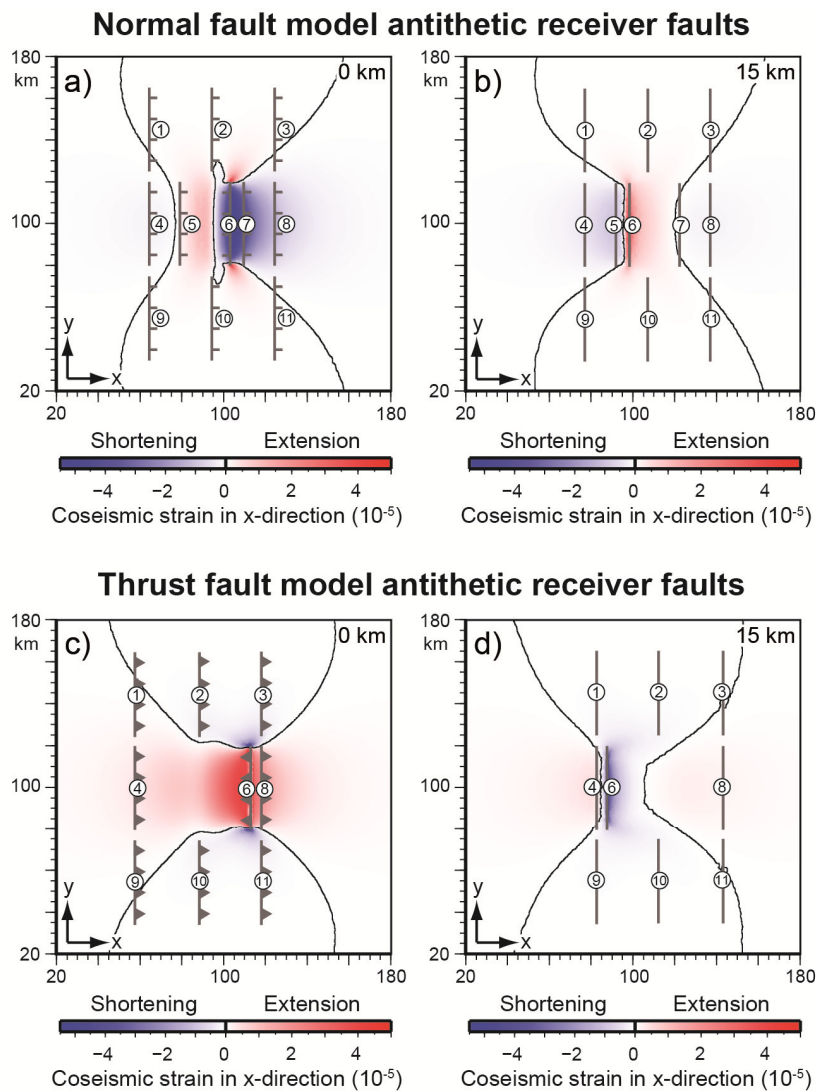


Figure 2.11: Coseismic horizontal strain in x -direction in the normal fault model with antithetic receiver faults (a) at the surface and (b) at 15 km depth and for the thrust fault model with antithetic receiver faults (c) at the surface and (d) at 15 km depth. Note that only a part of the model is shown. Areas of extension and shortening are shown in red and blue, respectively. Black line marks the location of zero coseismic strain. The position of the faults at depth is indicated by black lines with fault numbers.

also decreases away from the source fault, leading to asymmetric Coulomb stress distribution on the receiver (e.g. Figs. 2.3, 2.4). In all models, the lines of zero strain cross the planes of faults 1, 3, 9 and 11, either at the surface or at shallow depth (Figs. 2.10, 2.11, 2.12). These are the fault planes that are divided into areas with significant positive and negative Coulomb stress changes in all models (Figs. 2.3-2.8).

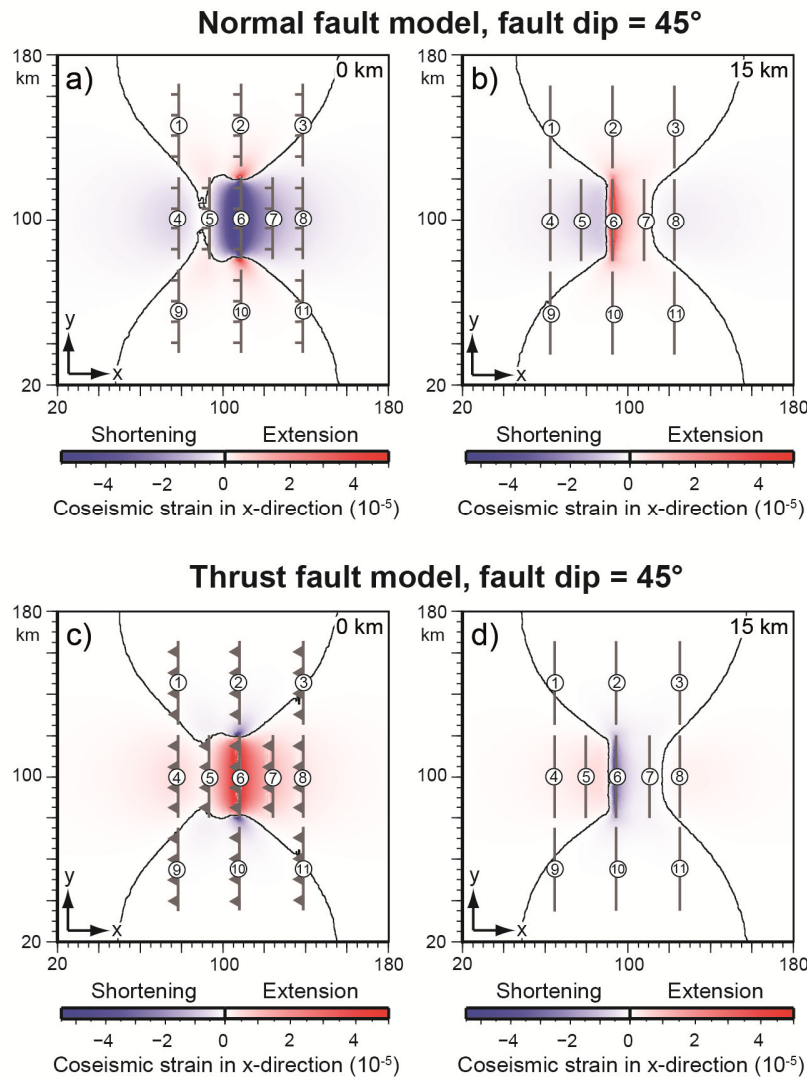


Figure 2.12: Coseismic horizontal strain in x-direction in the normal fault model with 45°-dipping receiver faults (a) at the surface and (b) at 15 km depth and for the thrust fault model with 45°-dipping receiver faults (c) at the surface and (d) at 15 km depth. Note that only a part of the model is shown. Areas of extension and shortening are shown in red and blue, respectively. Black line marks the location of zero coseismic strain. The position of the faults at depth is indicated by black lines with fault numbers.

2.4.3 Comparison with static Coulomb stress patterns derived from natural earthquakes

Regardless if normal or thrust fault, the highest positive stress changes in our models arise in the areas around the source fault's tips as well as in smaller zones on those receiver fault that

are located directly in the hanging wall and footwall of the source fault. In the following, we present examples from the literature, in which subsequent earthquakes are shown to be located in these areas of positive static Coulomb stress changes. Note that we focus on relationships between positive Coulomb stress changes and earthquake triggering, since correlations between negative Coulomb stress changes and reduced seismicity are obviously more uncertain and difficult to assess. Such an evaluation would require, for example, information about the timing of the last earthquake and the rate of interseismic loading of the respective receiver fault, which is not readily available. Links between areas of seismic quiescence and negative Coulomb stress changes were discussed, for example, by Bhloscaidh et al. (2014) for the case of the San Jacinto Fault Zone after the 1992 Landers earthquake.

An example for a historical sequence of normal faulting earthquakes, in which almost each event occurred in the stress triggering zones of the previous earthquake, was presented by Nostro et al. (1997). Between 1688 and 1980, several SE-NW striking normal faults in the southern Apennines were ruptured by large earthquakes, most of which occurred in the stress-triggering zones northwest or southeast of the previous source fault. For example, the 1694 Irpinia event occurred southeast of the fault that was ruptured by the 1688 Benevento earthquake. The two earthquakes lead to positive Coulomb stress changes in a 40 to 50 km wide region between the tips of the source faults. The next 1702 and 1732 earthquakes ruptured in this stress-triggering zone. In 1805 and 1857, two earthquakes ruptured in the stress triggering zones at the opposite tips of the source faults of the 1688 and 1694 earthquakes, respectively. Notably, the sequence of seismic events apparently continued to propagate to the northwest, with a potential link to the 1915 and 1984 earthquakes in the central Apennines (Nostro et al. 1997). An exception from this sequence of presumably triggered events is the 1930 earthquake that occurred in a stress-shadow zone of the previous events (Nostro et al. 1997). The fault that later ruptured during the 1980 Irpinia earthquake was located partly in stress-triggering and stress-shadow zones. The 1980 event itself presumably triggered within tens of seconds another earthquake on an antithetic receiver fault located in the hanging wall ~14 km away from the source fault. This may correspond to the positive Coulomb stress change observed in the upper part of our model fault 5 (Fig. 2.4a). Later, the 1997 Umbria-Marche earthquake sequence further north in the central Apennines may provide another potential example for static Coulomb stress triggering, as it occurred on SE-NW-striking faults located in the area between the southeastern end of the fault ruptured by the 1984 Gubbio earthquake and the northwestern end of the fault ruptured by the 1979 Norcia earthquake (Cocco et al. 2000). Apart from the static Coulomb stress changes, other

mechanisms might be important for earthquake triggering as well. For example, the Umbria-Marche earthquake sequence could also have been triggered by a fluid pressure pulse, which was generated by the coseismic release of a known deep source of trapped high-pressure carbon dioxide and associated with pore pressure changes in excess of the static Coulomb stress changes (Miller et al. 2004).

An example for a potentially triggered thrust fault event is provided by the 2013 $M_w = 6.6$ Lushan (China) earthquake on the southern part of the Longmenshan fault (Wang et al. 2014b, Parsons and Segou 2014). It took place ~45 km southwest of the southern end of the NE-SW striking Beichuan and Pengguan thrust faults. These faults failed during the 2008 $M_w = 7.9$ Wenchuan earthquake, which was associated with 9-10 m of oblique reverse slip (e.g. Lin et al. 2009, Jia et al. 2010, 2014). After the 2008 Wenchuan earthquake, several author teams calculated the static Coulomb stress changes for the region (Parsons et al. 2008, Toda et al. 2008, Luo and Liu 2010, Wan and Shen 2010, Nalbant and McCloskey 2011, Wang et al. 2014a). All studies generally obtained stress-triggering zones in the regions southwest and northeast of Pengguan and Beichuan faults, which would also be expected from our results (Fig. 2.3), although our model does not consider oblique shortening. The 2013 Lushan earthquake occurred in the southwestern stress-triggering zone of the 2008 event, suggesting that the positive static Coulomb stress changes brought the Longmenshan fault closer to failure (e.g. Jia et al. 2014, Parsons and Segou 2014, Wang et al. 2014b). In other regions of positive stress changes (e.g. south of the city of Chengdu; Parsons and Segou 2014) caused by the 2008 Wenchuan event, no earthquakes have been triggered so far. This highlights that the actual triggering of earthquakes does not only depend on the actual Coulomb stress change but also on other factors including the status of the receiver fault with respect to its earthquake cycle. For example, for a fault in its early interseismic period, the Coulomb stress changes may not be sufficient to trigger the next earthquake.

2.5 Conclusions

Using three-dimensional finite-element models, in which slip on the model faults is not prescribed and which include gravity and far-field tectonic deformation, we have evaluated the general patterns of coseismic Coulomb stress changes on intra-continental normal and thrust faults. Our results show that the spatial distribution of the stress-shadow and stress-triggering zones is similar for both types of faults. The magnitude and sign of the stress changes can vary along-strike of the receiver faults as well as with depth, resulting in asymmetric stress change distributions. Positive Coulomb stress changes can be expected near

the tips of the source fault and on faults located beyond the nearby hanging wall and footwall of the source fault. In the latter areas, negative Coulomb stresses prevail although some faults also show small areas of positive Coulomb stress changes, where earthquakes could be triggered. The observed Coulomb stress changes can be explained by the coseismic strain distribution. In the normal fault model, stress-shadow and stress-triggering zones correlate with regions of contractional and extensional strain. The opposite holds for the thrust fault model. The spatial distribution of the Coulomb stress changes is primarily governed by the position of the receiver fault relative to the source fault, the fault dip and dip direction. In contrast, the amount of coseismic slip and the friction coefficient only affect their magnitude.

The principle setup of our model is versatile and can be adjusted to a variety of different receiver fault configurations, including combinations of pure dip-slip and oblique normal and thrust faults. Rather than plotting maps of Coulomb stress changes, which are only valid for receiver faults of a particular geometry, our models allow resolving the Coulomb stress changes and their spatial variations on individual fault planes. In future studies, we will use our models to explore other mechanisms of fault interactions, including Coulomb stress changes due to postseismic relaxation in the lower crust and lithospheric mantle.

3 Postseismic Coulomb stress changes on intra-continental dip-slip faults due to viscoelastic relaxation in the lower crust and lithospheric mantle: insights from 3D finite-element modelling

(This chapter has been submitted to the International Journal of Earth Sciences)

Abstract

Earthquakes in the brittle upper crust induce viscoelastic flow in the lower crust and lithospheric mantle, which can persist for decades and lead to significant Coulomb stress changes on receiver faults located in the surrounding area of the earthquake source fault. As most previous studies calculated the Coulomb stress changes for a specific earthquake in nature, a general investigation of postseismic Coulomb stress changes independent of local geological conditions is still lacking for intra-continental dip-slip faults. Here we use finite-element models with normal and thrust fault arrays, respectively, to show that postseismic viscoelastic flow considerably modifies the original coseismic Coulomb stress patterns through space and time. Depending on the position of the receiver fault relative to the source fault, areas with negative coseismic stress changes may exhibit positive postseismic stress changes and *vice versa*. The lower the viscosity of the lower crust or lithospheric mantle, the more pronounced are the transient stress changes in the first years. For example, a viscosity of 10^{18} Pa s leads to a stress increase of up to ~ 22 bar in the first postseismic year, whereas a viscosity of 10^{20} Pa s causes positive stress changes of up to ~ 5 bar. The layer with the lowest viscosity has the largest influence on the stress changes. Furthermore, the evolution of postseismic Coulomb stress changes is controlled by the superposition of the transient stress changes caused by viscoelastic relaxation (leading to stress increase or decrease) and the interseismic strain accumulation (leading to a stress increase). Stress changes induced by viscoelastic relaxation can outweigh the interseismic stress increase such that negative Coulomb stress changes can persist for decades. On some faults, postseismic relaxation and interseismic strain accumulation can act in concert to enhance already positive Coulomb stress changes. Our model results show that the pattern of postseismic Coulomb stress changes is caused by postseismic perturbations in the velocity field, which originate in the viscoelastic layers but also affect the brittle upper crust.

Keywords: postseismic Coulomb stress changes, viscoelastic relaxation, numerical modelling

3.1 Introduction

The calculation of Coulomb stress changes after a major earthquake has become an important tool to evaluate the future seismic hazard of a region. In general, positive Coulomb stress changes bring receiver faults closer to failure, while a negative value indicates a delay of the next earthquake (Stein 1999). Coulomb stress changes can arise from a variety of processes during and after the earthquake (e.g. Freed 2005). As a consequence of the coseismic slip on the source fault, receiver faults may experience positive or negative static Coulomb stress changes, depending on the position relative to the source fault (King et al 1994, Nostro et al. 1997, Lin et al. 2011, Bagge and Hampel 2015). The magnitude of the static stress changes typically does not exceed a few percent of the coseismic stress drop, i.e. it is often much less than 1 MPa (Lin and Stein 2004, Lin et al. 2011, Nostro et al. 1997, Ryder et al. 2012, Stein 1999). On the other hand, Coulomb stress changes can also be caused by seismic waves (Belardinelli et al. 1999, Pollitz et al. 2012), postseismic fluid flow (Cocco and Rice 2002, Miller et al. 2004, Piombo et al. 2005) and postseismic viscoelastic relaxation (Freed and Lin 1998, Gourmelen and Amelung 2005, Nostro et al. 2001, Pollitz 1997). Postseismic relaxation is the transient response of the viscoelastic layers in the lithosphere to the sudden coseismic slip in the brittle upper crust and acts on timescales of months to decades, depending on the viscosity of the excited layers (Cattania et al. 2015, Chéry et al. 2001, Ellis and Stöckhert 2004, Freed and Lin 2001, Hampel and Hetzel 2015, Sun et al. 2014). In the early postseismic phase, the effect of viscoelastic relaxation on displacements and Coulomb stress changes may be intermingled with afterslip but the effect of the local afterslip rapidly decreases while the effect of viscoelastic relaxation increases with time and acts on a larger regional scale (Cattania et al. 2015, Diao et al. 2014, Hampel and Hetzel 2015). Modelling and geodetic data of the 2011 $M_w = 9.0$ Tohoku-Oki earthquake (Japan) showed that viscoelastic relaxation plays a dominant role over afterslip even during short-term postseismic deformation (Sun et al. 2014).

While there is a large number of studies on coseismic Coulomb stress changes (e.g. King et al. 1994, Lin and Stein 2004, Nostro et al. 1997, Parsons et al. 2008), stress changes due to postseismic viscoelastic relaxation have less often been quantified, and mostly for strike-slip faults (e.g. Freed and Lin 2001, Masterlark and Wang 2002, Smith and Sandwell 2006). Fewer studies were dedicated to the postseismic stress interaction between normal faults or thrust faults (e.g. Freed and Lin 1998, Nalbant and McCloskey 2011, Nostro et al.

2001, Wang et al. 2014b). Interactions between normal faults due to postseismic relaxation have been investigated by Nostro et al. (2001). Using self-gravitating and stratified spherical Earth models with viscoelastic layers, they calculated co- and postseismic stress changes on timescales up to centuries and on spatial scales up to several 100 km to evaluate the influence of the rheological stratification and the thickness of the layers. They compared their models with the normal faults in the Apennines (Italy) and concluded that the relaxation tends to increase the Coulomb stresses. Freed and Lin (1998) investigated – based on a potential connection between the 1971 San Fernando and 1994 Northridge thrust fault earthquakes – the time-dependent stress changes caused by relaxation in the viscous lower crust and upper mantle using two-dimensional finite element models. Their results indicate that postseismic creep generates a stress triggering zone at the base of the upper crust. Finally, several studies have computed postseismic Coulomb stress changes after the 2008 Wenchuan (China) oblique thrust fault earthquake (Chen et al. 2011, Luo and Liu 2010, Nalbant and McCloskey 2011, Wang et al. 2014b). Using a finite-element model comprising an upper crust and a viscoelastic layer representing both lower crust and lithospheric mantle, Luo and Liu (2010) studied the effects of the 2008 earthquake resolved on the major faults of southeastern Tibet. On a larger scale, Chen et al. (2011) used a finite-element block model to calculate the Coulomb stress changes on major strike-slip and thrust fault for the entire Tibetan Plateau, however, for all thrust faults (except the Beichuan thrust) a vertical dip was assumed. Nalbant and McCloskey (2011) focused on the region around the 2008 earthquake and included previous earthquakes as well as a rheologically stratified lithosphere. All analyses came to the general conclusion that positive stress changes can be expected for the region southwest and northeast of the location of the 2008 event. Indeed, in April 2013, a $M = 6.6$ thrust earthquake occurred southwest of the fault that was ruptured during the 2008 event (Wang et al. 2014b), i.e. in the region, where positive Coulomb stress changes had been predicted for thrust faults (Chen et al. 2011, Luo and Liu 2010, Nalbant and McCloskey 2011, Parsons et al. 2008, Wang et al. 2014b).

In contrast to previous studies, which were mostly dedicated to a specific setting or earthquake, the scope of our study is a better understanding of the general patterns of postseismic Coulomb stress changes on normal and thrust faults. Using three-dimensional finite-element models with arrays of 11 normal or thrust faults, we analyse the spatiotemporal evolution of postseismic Coulomb stress changes on individual fault planes caused by viscoelastic relaxation in space and time. In different experiments, we varied the viscosities of the lower crust and lithospheric mantle. Our analysis includes an evaluation of the differences

between the two types of faults as well as the relative importance between stress changes arising from viscoelastic relaxation and stress changes caused by ongoing extension or shortening. In a second step, we link the Coulomb stress changes to the postseismic movements in the crust and lithospheric mantle to explain the obtained stress change distributions.

3.2 Model setup

For our parameter study, we used the commercial finite-element software Abaqus (version 6.14) to create three-dimensional models with normal and thrust fault arrays, respectively (cf. Bagge and Hampel 2015). Each model represents a 200 x 200 km wide and 100-km-thick continental lithosphere, which consists of an elastic upper crust, a viscoelastic lower crust and a viscoelastic lithospheric mantle. The thickness and rheological parameters of the layers (density ρ , Poisson's ratio ν , Young's modulus E and viscosity η) are shown in Figure 3.1. Viscoelastic behaviour is implemented as linear, temperature-independent Maxwell viscoelasticity. We ran experiments with different viscosities of the lower crust and lithospheric mantle (Tab. 3.1). Our choice of viscosities and viscosity contrasts is based on laboratory experiments, geophysical data, forward modelling of geodetic data and other numerical modelling studies (Brace and Kohlstedt 1980, Burov and Watts 2006, Chen and Molnar 1983, Gourmelen and Amelung 2005, Kaufmann and Amelung 2000, Klemperer 2006, Nishimura and Thatcher 2003, Shi et al. 2015).

Table 3.1: Viscosities of the lower crust and lithospheric mantle in the models used for this study.

Model name	Fault type	Viscosity of lower crust η_{lc} (Pa s)	Viscosity of lithospheric mantle η_{lm} (Pa s)	Viscosity structure
NP1	normal	10^{20}	10^{23}	$\eta_{lc} < \eta_{lm}$
TP1	thrust			
NP2	normal	10^{18}	10^{22}	
TP2	thrust			
NP3	normal	10^{18}	10^{23}	
TP3	thrust			
NP4	normal	10^{21}	10^{19}	$\eta_{lc} > \eta_{lm}$
TP4	thrust			
NP5	normal	10^{22}	10^{19}	
TP5	thrust			
NP6	normal	10^{22}	10^{21}	
TP6	thrust			

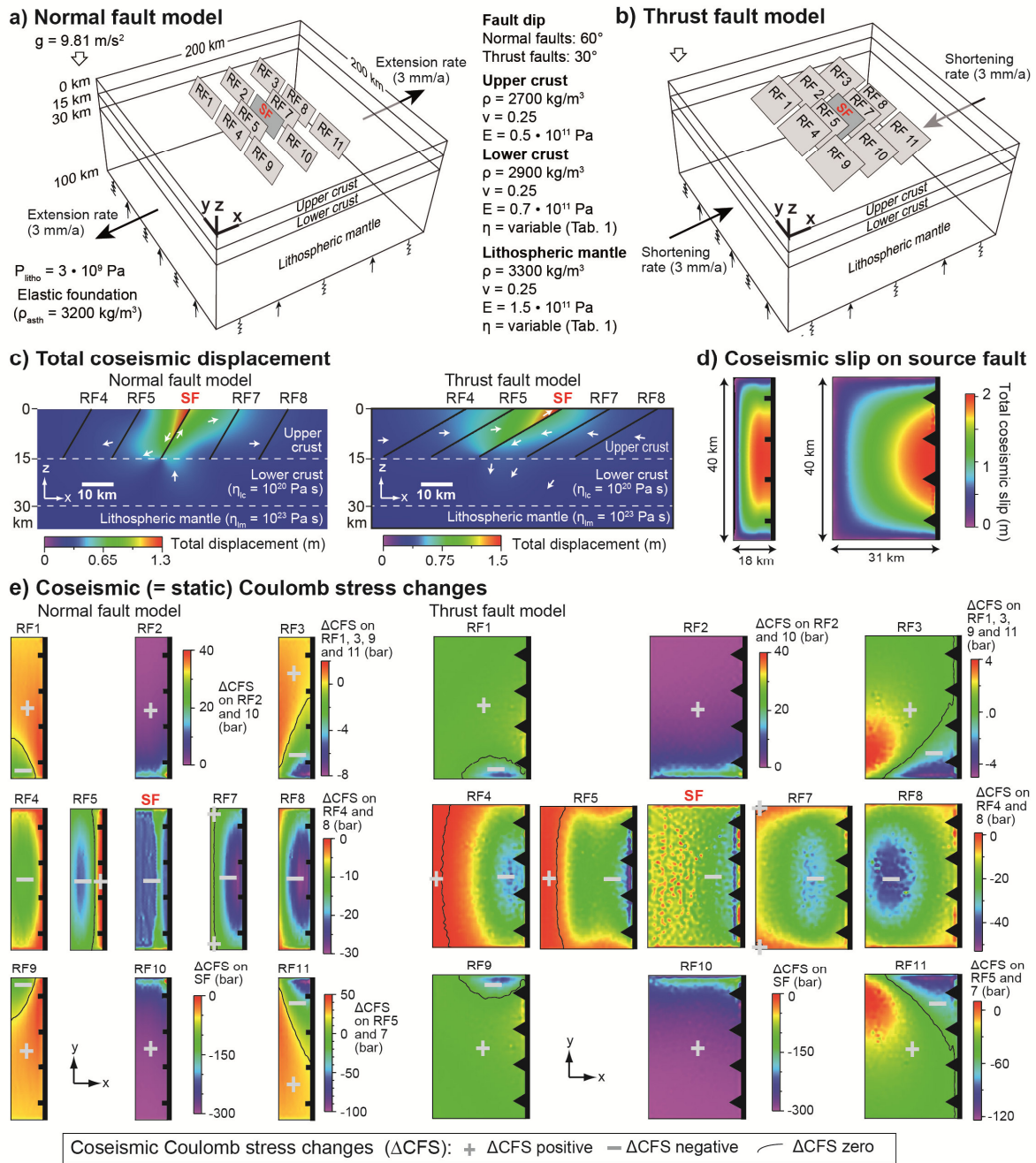


Figure 3.1: Perspective view of the three-dimensional models with arrays of 40-km-long (a) normal faults and (b) thrust faults. A source fault (SF) and ten receiver faults (RF) are embedded in the upper crust. A velocity boundary condition is applied to the model sides in the yz-plane to extend or shorten the model at a total rate of 6 mm/a, which initiates slip on the faults. Abbreviations are ρ density, E Young's modulus, ν Poisson's ratio, η viscosity, g acceleration due to gravity, P_{litho} lithostatic pressure and ρ_{asth} density of the asthenosphere. (c) Cross-sections through the central part of the model showing the total coseismic displacement field. (d) Coseismic slip distribution on the normal and thrust source faults. Maximum slip is 2 m. (e) Coseismic Coulomb stress changes caused by a model earthquake on the source fault. See text for details. Modified from Bagge and Hampel (2015).

In the model centre, a source fault (fault 6 in Fig. 3.1) that will experience the coseismic slip during the analysis, and ten surrounding receiver faults are embedded in the upper crust. The 60°-dipping normal faults (Fig. 3.1a) and 30°-dipping thrust faults (Fig. 3.1b) are 40 km long and extend from the model surface to the bottom of the upper crust. Following

natural spatial configurations of faults, for example, in the Basin and Range Province (Haller et al. 2004), the Aegean region (Roberts and Michetti 2004) and the foreland of the Tibetan (Meyer et al. 1998, Hetzel et al. 2004), we apply distances between the faults of ≥ 15 km in the x-direction and ≥ 5 km in the y-direction. Gravity is implemented as body force. Isostatic effects are simulated by applying a lithostatic pressure of $3 \cdot 10^9$ Pa and an elastic foundation to the model bottom. The model sides in the xz-plane are fixed in the y-direction. Model sides and bottom are free to move in the vertical direction. All models are meshed by linear tetrahedral elements with an edge length of 1 km near the faults, which increases to 3 km at the model margins.

Each model run consists of a series of quasi-static analysis steps. After reaching a state of isostatic equilibrium, the model is extended or shortened at a total rate of 6 mm/a (Fig. 3.1a, b) throughout the remaining model time, which generates the tectonic background deformation and initiates slip on the faults. Slip initiation is controlled by the Mohr-Coulomb criterion $|\tau_{\max}| = c + \mu\sigma_n$, where τ_{\max} is the critical shear stress, c is the cohesion (zero in our model), σ_n is the normal stress and μ the coefficient of friction (0.6 in our model). After all faults have reached a constant slip rate, the earthquake cycle is simulated in three steps (cf. Hampel and Hetzel 2012, 2015, Hampel et al. 2013). In the preseismic phase, all faults are locked. In the coseismic phase, we unlock only the source fault (fault 6 in Figure 3.1), which leads to sudden slip (= model earthquake). Note that the slip distribution is not prescribed but develops self-consistently in accordance with the strain accumulated during the preseismic phase. In the models of this study, we define the duration of the preseismic phase such that the maximum coseismic slip is 2 m on the 40-km-long fault during the coseismic phase, which is equivalent to a $M_w \approx 7$ earthquake (Wells and Coppersmith 1994). All receiver faults remain locked during the coseismic phase. In the postseismic phase, we lock all faults again. Note that no afterslip occurs on fault 6 during the postseismic phase, as the fault fully relaxes during the coseismic phase (Ellis et al. 2006).

Figure 3.1c-e shows the coseismic displacement field, the coseismic slip distribution and the resulting static Coulomb stress changes as derived from the normal and thrust fault models with a viscosity of 10^{20} and 10^{23} Pa s for the lower crust and lithospheric mantle, respectively (Bagge and Hampel 2015). Note that the coseismic displacements and stress changes do not depend on the viscosity structures and are hence the same in all models of this study. They provide the common basis for our analysis of the postseismic Coulomb stress changes, for which we varied the viscosities of the lower crust and lithospheric mantle in different experiments (Tab. 3.1). The coseismic displacements – plotted with their magnitude

and direction along a cross-section through the central part of the model – show the typical footwall uplift and hanging wall subsidence in the normal fault model and hanging wall uplift and footwall subsidence in the thrust fault model (Fig. 3.1c). The coseismic slip on fault 6 reaches its maximum in the centre of the fault's surface trace and has an elliptical distribution (Fig. 3.1d). Figure 3.1e illustrates the resulting coseismic Coulomb stress changes on the model fault planes. We calculated the Coulomb stress change ΔCFS by $\Delta CFS = \Delta\tau - \mu'\Delta\sigma_n$, where $\Delta\tau$ is the change in shear stress (positive in direction of source fault slip), μ' is the effective coefficient of friction and $\Delta\sigma_n$ is the change in normal stress (positive if fault is clamped) (e.g. Freed 2005, Stein et al. 1992, Stein 1999, 2003). A positive stress change implies that slip is promoted on the receiver faults in the direction of the slip of the source fault and the direction given by the regional stress field. In contrast, a negative Coulomb stress change means that slip on the fault in direction of the slip on the source fault is hampered. The earthquake in our model with 2 m of coseismic slip leads to static Coulomb stress changes on the receiver faults, which range from a few bar to several MPa (Fig. 3.1e). Both positive and negative Coulomb stress changes are observed, with changes in the sign occurring both along-strike of individual receiver fault as well as in their down-dip direction (Bagge and Hampel 2015). Generally, faults located in the hanging wall and footwall of the source fault (RF4-8) experience primarily negative coseismic stress changes with a symmetric distribution on each fault plane. Receiver faults RF5 and 7 located close to the source fault show significant positive stress changes in some parts of their fault plane. Faults RF2 and 10 positioned in the along-strike prolongation of the source fault undergo exclusively positive Coulomb stress changes and exhibit an asymmetric Coulomb stress change distribution. Receiver faults RF1, 3, 9 and 11 also show an asymmetric stress change distribution, with mostly positive stress changes but also high values of negative stress changes (Fig. 3.1e). Note that the distribution of Coulomb stress changes on RF1, 2 and 3 are mirror images to RF9, 10 and 11.

3.3 Model results

3.3.1 Postseismic Coulomb stress changes in the first year after the earthquake

In the first year after the earthquake, the original distribution of the coseismic Coulomb stress changes undergoes considerable modifications on most receiver faults (Figs. 3.2, 3.3). Depending on the viscosity structure of the lithosphere and the position of the receiver fault relative to the source fault, the sign of the Coulomb stress changes can be reversed on some

faults. For example, receiver fault RF7 was characterized by mainly negative coseismic stress changes but during the first postseismic year mainly positive stress changes occur on receiver fault RF7 in both thrust and normal fault models. A common characteristic of both coseismic and postseismic stress changes is that the stress change distribution is symmetric on faults RF4-8 but asymmetric on faults RF1-3 and 9-11. The order of magnitude of the postseismic Coulomb stress changes on the receiver faults ranges between 0.1 and 25 bar. Postseismic Coulomb stress changes on the source fault are generally an order of magnitude higher than on the receiver faults and have a positive sign in all models. In the following, we will describe the Coulomb stress changes resulting from the different viscosity structures of the model lithosphere in more detail.

In the normal (NP1) and thrust (TP1) models with viscosities of 10^{20} and 10^{23} Pa s for the lower crust and lithospheric mantle, respectively, all faults – except RF5 – experience positive stress changes (Figs. 3.2a, 3.3a). Faults RF1-3 and 9-11 exhibit a homogeneous Coulomb stress distribution with an average stress increase of 0.2 bar. In contrast, faults in the hanging wall and footwall of the source fault (RF4, 7, and 8) show a gradient in the positive stress changes. On RF4, the magnitude of the positive stress change increases towards the surface, whereas on RF7 and 8 the Coulomb stress change increases towards the downdip edge of the fault. The highest stress increase occurs in the lower part of RF7 in the normal fault model (0.3 bar) and in the upper part of RF5 in the thrust fault model (0.5 bar). In contrast to the other ten faults, receiver fault RF5 also shows negative stress changes, which occur in two separate areas on the fault plane. In the normal fault model, the highest stress decrease (-0.18 bar) occurs in a large stress shadow zone in the upper part of the fault; in its lower part, a second, smaller stress shadow zone is observed (Fig. 3.2a). In the thrust fault model, negative stress changes occur in the lower part of the fault, where they reach a value of up to -0.1 bar, and in the fault centre (Fig. 3.3a).

Models with a lower crustal viscosity of 10^{18} Pa s but different viscosities of the lithospheric mantle (NP2/3, TP2/3) show almost the same pattern and magnitudes of the Coulomb stress changes (Fig. 3.2b, c; Fig. 3.3b, c). Compared to models NP1 and TP1, the Coulomb stress changes are 1-2 orders of magnitude higher and almost all faults experience both positive and negative stress changes. Only the source fault and the normal faults RF3 and 11 show solely positive stress changes. Notably, many areas that experienced a coseismic stress increase show a postseismic stress decrease and *vice versa*. Only faults 1 and 9 show roughly the same distribution of stress triggering and shadow zones as during the coseismic phase. In the normal fault model, the highest values of stress increase occur on receiver faults

RF7 (7.9 bar) and on RF5 (5.5 bar). Positive stress changes of up to ~ 4 bar are observed on RF4 and 8 as well as in the surface corners of RF1 and 9 (Fig. 3.2b, c). Compared to the normal fault models, positive Coulomb stress changes in the thrust fault models reach much higher values, for example on RF5 (21.9 bar), RF7 (17.3 bar) and RF8 (14.9 bar). On thrust faults RF1-4 and 9-11, maximum values vary between 1.4 and 4.7 bar. The largest stress decrease occurs on fault RF5, which shows -22.7 bar in the normal fault models (Fig. 3.2b, c) and -11.7 bar in the thrust fault models (Fig. 3.3b, c). On the normal fault RF5, the maximum value occurs in a broad stress shadow zone that reaches the surface; a smaller zone with negative stress changes is located near the down-dip edge of the fault. On thrust fault RF5, the highest stress decrease occurs near the down-dip edge of the fault; a second stress shadow zone with almost the same magnitudes is located in the fault centre. Other stress shadow zones occur in the lower parts of normal faults RF4 (-9.7 bar) and RF1 and 9 (-2.0 bar), in the upper parts of RF7 and 8 (-2 bar), and in the distal part of RF2 and 10 (-8.7 bar). In the thrust fault model, two stress shadow zones exist on RF1, 4 and 9, one at the surface area and the other in the lower part of the faults, where maximum values of up to -6.9 bar (RF4) and -2.4 bar (RF1 and 9) are reached. On thrust faults RF2 and 10, the stress shadow zone runs across the fault centre and is located between two stress triggering zones. In contrast, thrust faults RF7 (-4.7 bar) and 8 (-2.1 bar) show a similar stress change distribution as their counterparts in the normal fault model, with zones of stress decrease near the surface.

Postseismic Coulomb stress changes in the models NP4/5 and TP4/5, in which the lower crust has a higher viscosity than the lithospheric mantle ($\eta_{lc} = 10^{21}$ or 10^{22} Pa s; $\eta_{lm} = 10^{19}$ Pa s), show a pronounced and large stress triggering zone in the central part of the fault array, i.e. on the source fault, the upper part of RF5, the lower parts of RF7 and 8 and in the parts of RF2 and 10 that are located close to the source fault (Fig. 3.2d, e; Fig. 3.3d, e). In these areas, the stress increases reach maximum values between 0.3-2.1 bar. Stress shadow zones are found in both models in the lower part of RF5 (normal fault: -0.3 bar; thrust fault: -0.9 bar) and in the upper parts of RF3, 8 and 11. Receiver fault RF7 shows solely positive stress changes in the normal fault model, whereas its upper part is located in a stress shadow zone in the thrust fault model. Another difference between the two fault models is the location of the stress triggering zone on RF4, which occurs in the upper part of the normal fault but in the lower part of the thrust fault. In contrast, RF1 and 9 show stress triggering zones in their parts that are located close to RF4 in both types of models.

Finally, the results from the models with a lower crustal viscosity of 10^{22} Pa s and a lithospheric mantle viscosity of 10^{21} Pa s (NP6, TP6) show that all faults of the array

including the source fault experience an almost homogeneous distribution of positive Coulomb stress changes on the order of 0.2 bar. No stress shadow zones occur in these models.

Normal fault models: Postseismic Coulomb stress changes during the first year after the earthquake

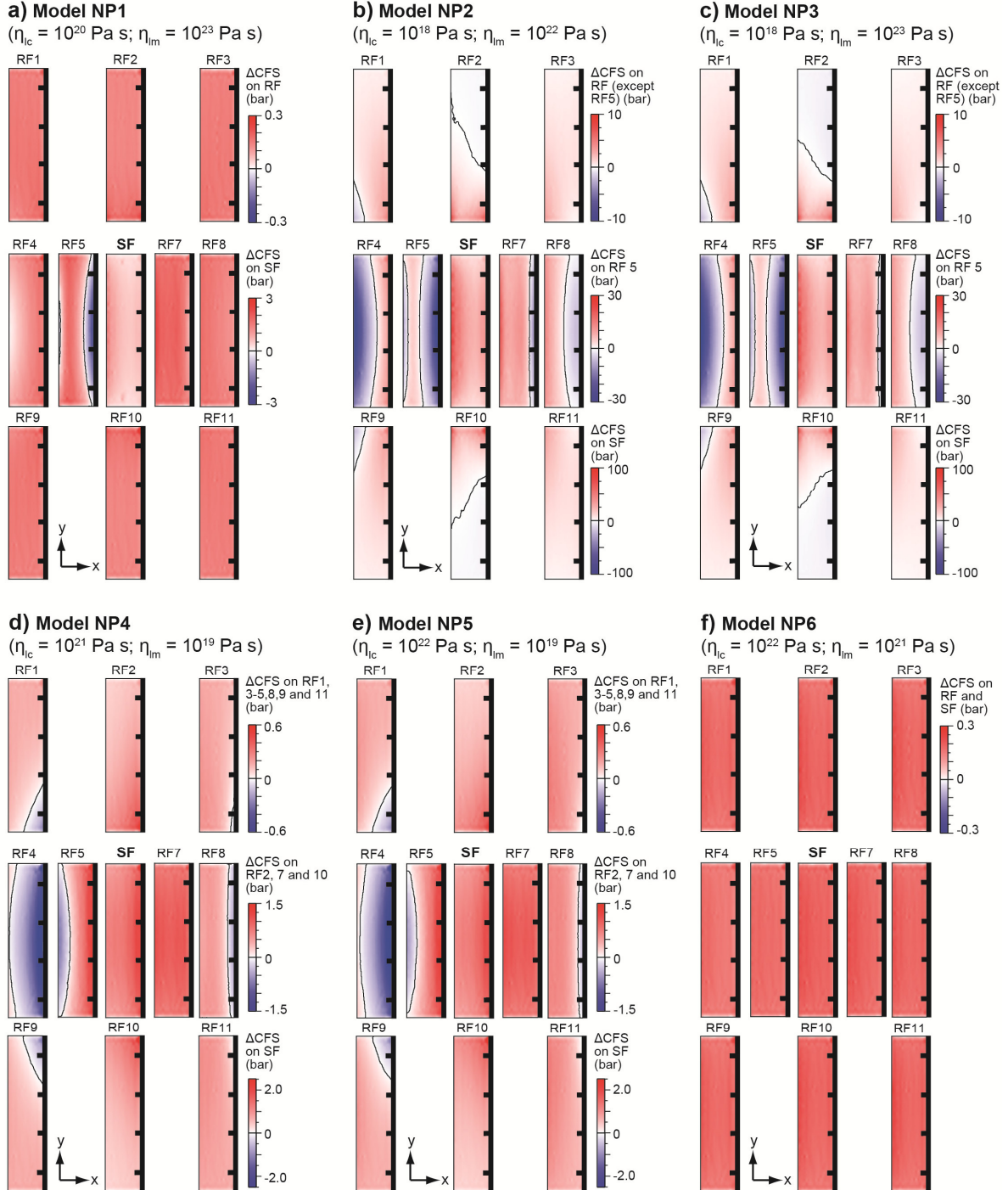


Figure 3.2: Postseismic Coulomb stress changes (ΔCFS) on receiver faults (RF) in the first year after the earthquake on the source fault (SF) as derived from normal fault model (a) NP1 ($\eta_{lc} = 10^{20} \text{ Pa s}; \eta_{lm} = 10^{23} \text{ Pa s}$), (b) NP2 ($\eta_{lc} = 10^{18} \text{ Pa s}; \eta_{lm} = 10^{22} \text{ Pa s}$), (c) NP3 ($\eta_{lc} = 10^{18} \text{ Pa s}; \eta_{lm} = 10^{23} \text{ Pa s}$), (d) NP4 ($\eta_{lc} = 10^{21} \text{ Pa s}; \eta_{lm} = 10^{19} \text{ Pa s}$), (e) NP5 ($\eta_{lc} = 10^{22} \text{ Pa s}; \eta_{lm} = 10^{19} \text{ Pa s}$) and (f) NP6 ($\eta_{lc} = 10^{22} \text{ Pa s}; \eta_{lm} = 10^{21} \text{ Pa s}$). Note that the distance between the faults is not to scale. The distance in the x-direction between the fault surface traces is 15 km in the centre row (RF4-8) and 30 km in the upper (RF1-3) and lower (RF9-11) rows of the fault array. The distance in the y-direction is 5 km. Areas with positive Coulomb stress changes (red) and negative stress changes (blue) are separated by a black line where $\Delta\text{CFS} = 0$.

Thrust fault models: Postseismic Coulomb stress changes during the first year after the earthquake

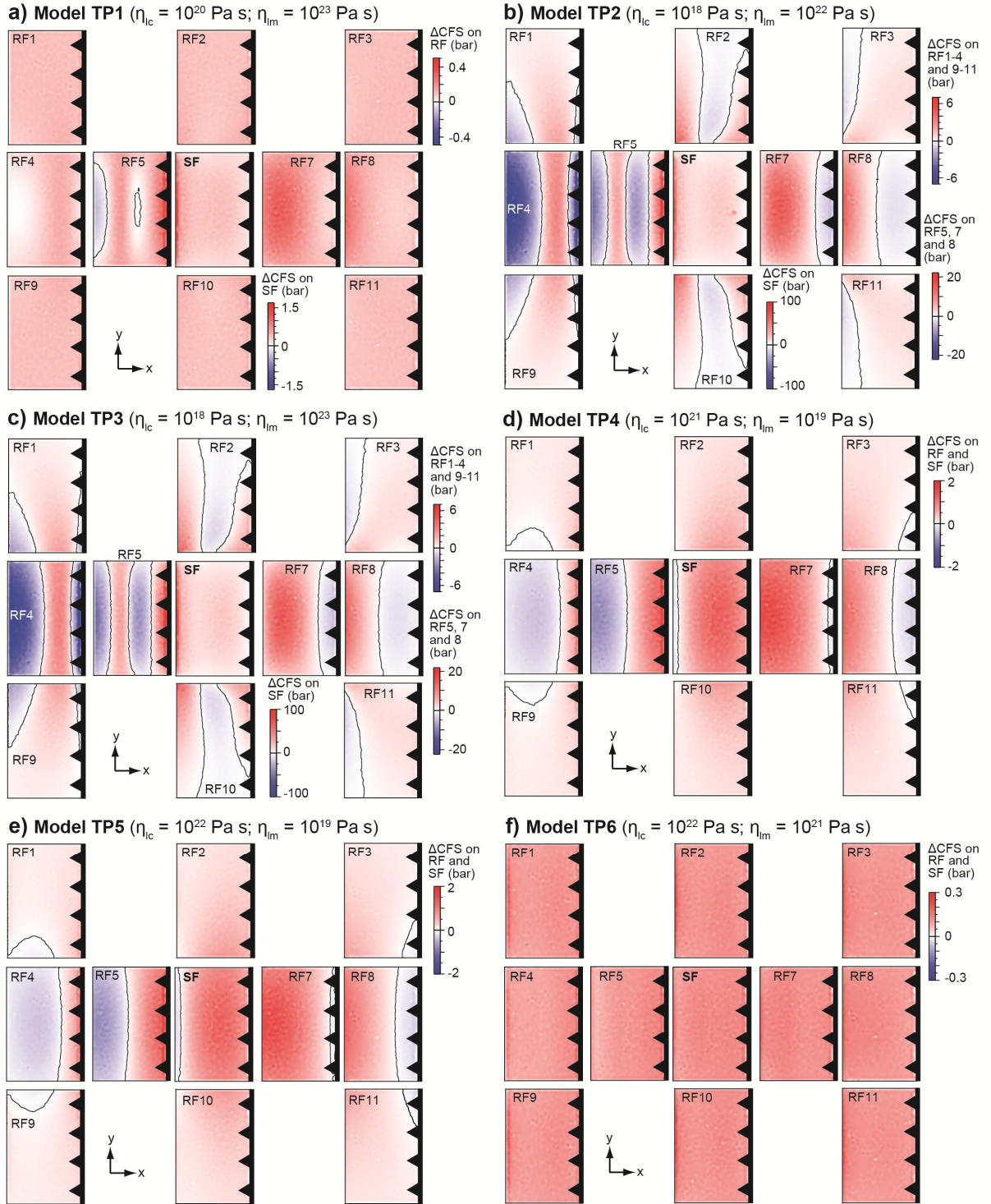


Figure 3.3: Postseismic Coulomb stress changes (ΔCFS) on receiver faults (RF) in the first year after the earthquake on the source fault (SF) as derived from thrust fault model (a) TP1 ($\eta_{lc} = 10^{20}$ Pa s; $\eta_{lm} = 10^{23}$ Pa s), (b) TP2 ($\eta_{lc} = 10^{18}$ Pa s; $\eta_{lm} = 10^{22}$ Pa s), (c) TP3 ($\eta_{lc} = 10^{18}$ Pa s; $\eta_{lm} = 10^{23}$ Pa s), (d) TP4 ($\eta_{lc} = 10^{21}$ Pa s; $\eta_{lm} = 10^{19}$ Pa s), (e) TP5 ($\eta_{lc} = 10^{22}$ Pa s; $\eta_{lm} = 10^{19}$ Pa s) and (f) TP6 ($\eta_{lc} = 10^{22}$ Pa s; $\eta_{lm} = 10^{21}$ Pa s). Note that the distance between the faults is not to scale. The distance in the x-direction between the fault surface traces is 15 km in the centre row (RF4-8) and 30 km in the upper (RF1-3) and lower (RF9-11) rows of the fault array. The distance in the y-direction is 5 km. Areas with positive Coulomb stress changes (red) and negative stress changes (blue) are separated by a black line where $\Delta CFS = 0$.

3.3.2 Postseismic Coulomb stress changes in the 10th and 20th years after the earthquake

Depending on the viscosity structure of the lithosphere, the pattern and magnitude of the postseismic Coulomb stress changes show a different evolution through time. In the models NP1 and TP1 ($\eta_{lc} = 10^{20}$ Pa s; $\eta_{lm} = 10^{23}$ Pa s), neither the distribution nor the magnitudes of the stress changes are considerably altered until the 10th and 20th years after the earthquake (Figs. 3.4a, 3.5a). Similarly, the positive stress changes remain constant at a value of ~ 0.2 bar in the models NP6 and TP6 (Figs. 3.6c, 3.7c). In contrast, the models involving lower viscosities either of the lower crust or the lithospheric mantle exhibit considerable changes in the distribution and magnitudes of the Coulomb stress changes. Models with a viscosity of $\eta_{lc} = 10^{18}$ Pa s (NP2/3, TP2/3) show similar evolutions, regardless of the viscosity of the lithospheric mantle (cf. Figs. 3.4b, 3.5b with Figs. 3.6a and 3.7a). In these models, most stress shadow zones of the first year have shifted their position on the fault plane (e.g. RF1, 9) or turned into stress triggering zones in the 10th year (e.g. RF2, 10). On some faults, the distribution of positive and negative stress changes in the 10th year is inverse to the first year (e.g. normal RF7, thrust fault RF4). One of the faults, on which the stress change pattern remained almost constant, is RF8, which still shows a stress shadow zone in its upper part. This stress shadow zone disappears until the 20th year in the normal fault model (Fig. 3.4b); in the thrust fault, the area becomes smaller (Fig. 3.5b). In contrast, the zone of negative stress changes that was present in the lower part of normal fault RF5 during the first year has disappeared. In the thrust fault model, the source fault experiences a stress decrease in its lower half, which is not observed in the normal fault model. Generally, the magnitude of the stress change on the faults has dropped by an order of magnitude (Figs. 3.4, 3.5). For example, the maximum of the stress increase on fault RF5 dropped from 5.5 bar to 0.7 bar in the normal fault model and from 21.9 bar to 1.2 bar in the thrust fault model. The highest positive stress changes in the 10th year on receiver faults occur on normal fault RF7 (0.9 bar) and thrust fault RF5 (1.2 bar). The largest stress decrease is observed on normal fault RF4 (-0.7 bar) and on thrust fault RF7 (-0.5 bar).

Models with a low viscosity of the lithospheric mantle (NP4/5, TP4/5) show an almost identical evolution for the two different viscosities of the lower crust (Figs. 3.4c, 3.5c, 3.6b, 3.7b). In these models, the overall spatial distribution of stress triggering and shadow zones has remained almost the same between the first and 10th year but the stress shadow zones have become smaller or disappeared. There are no new stress shadow zones. This trend is also observed in the 20th year (e.g. RF4). Compared to the models with a low viscosity of the

Normal fault models: Postseismic Coulomb stress changes
10th year after earthquake **20th year after earthquake**

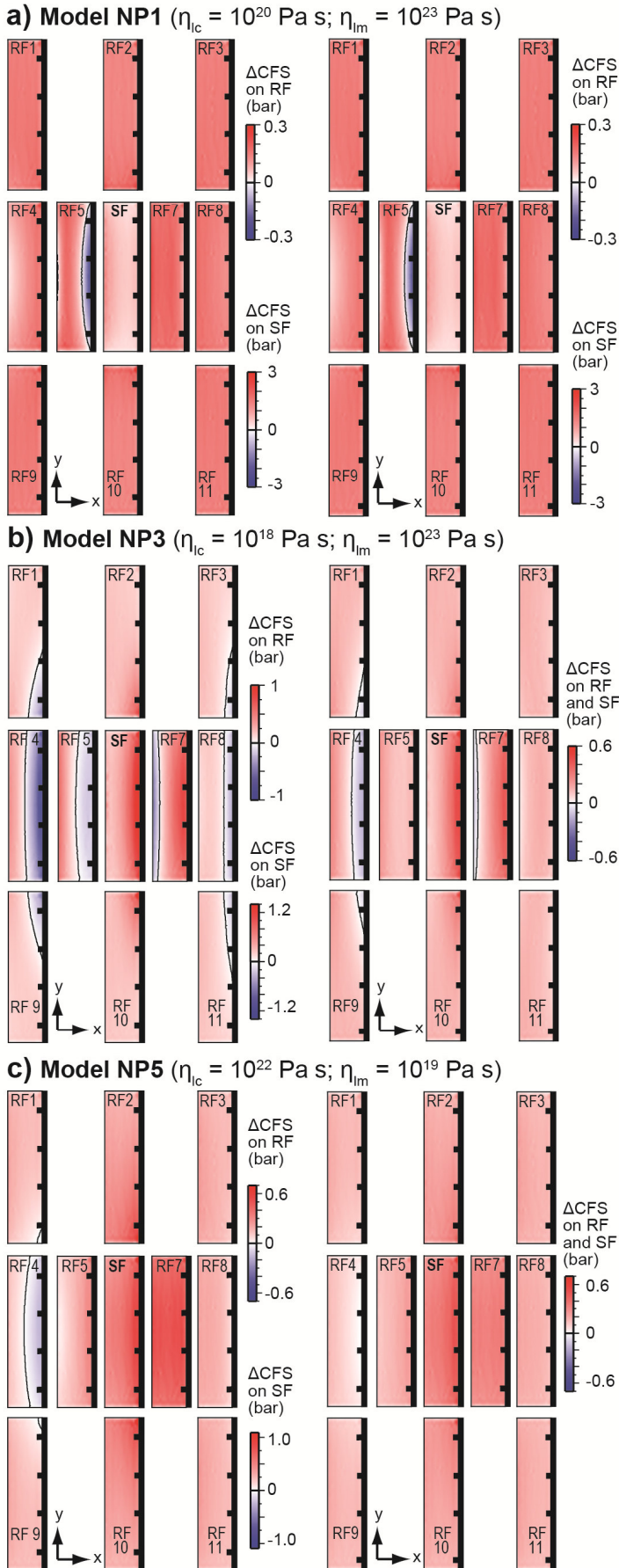


Figure 3.4: Postseismic Coulomb stress changes (ΔCFS) on receiver faults (RF) in the 10th and 20th year after the earthquake on the source fault (SF) as derived from normal fault model (a) NP1 ($\eta_{lc} = 10^{20}$ Pa s; $\eta_{lm} = 10^{23}$ Pa s), (b) NP3 ($\eta_{lc} = 10^{18}$ Pa s; $\eta_{lm} = 10^{23}$ Pa s) and (c) NP5 ($\eta_{lc} = 10^{22}$ Pa s; $\eta_{lm} = 10^{19}$ Pa s). For results from models NP2, NP4 and NP6 see Figure 3.6. Note that the distance between the faults is not to scale. The distance in the x-direction between the fault surface traces is 15 km in the centre row (RF4-8) and 30 km in the upper (RF1-3) and lower (RF9-11) rows of the fault array. The distance in the y-direction is 5 km. Areas with positive Coulomb stress changes (red) and negative stress changes (blue) are separated by a black line where $\Delta CFS = 0$.

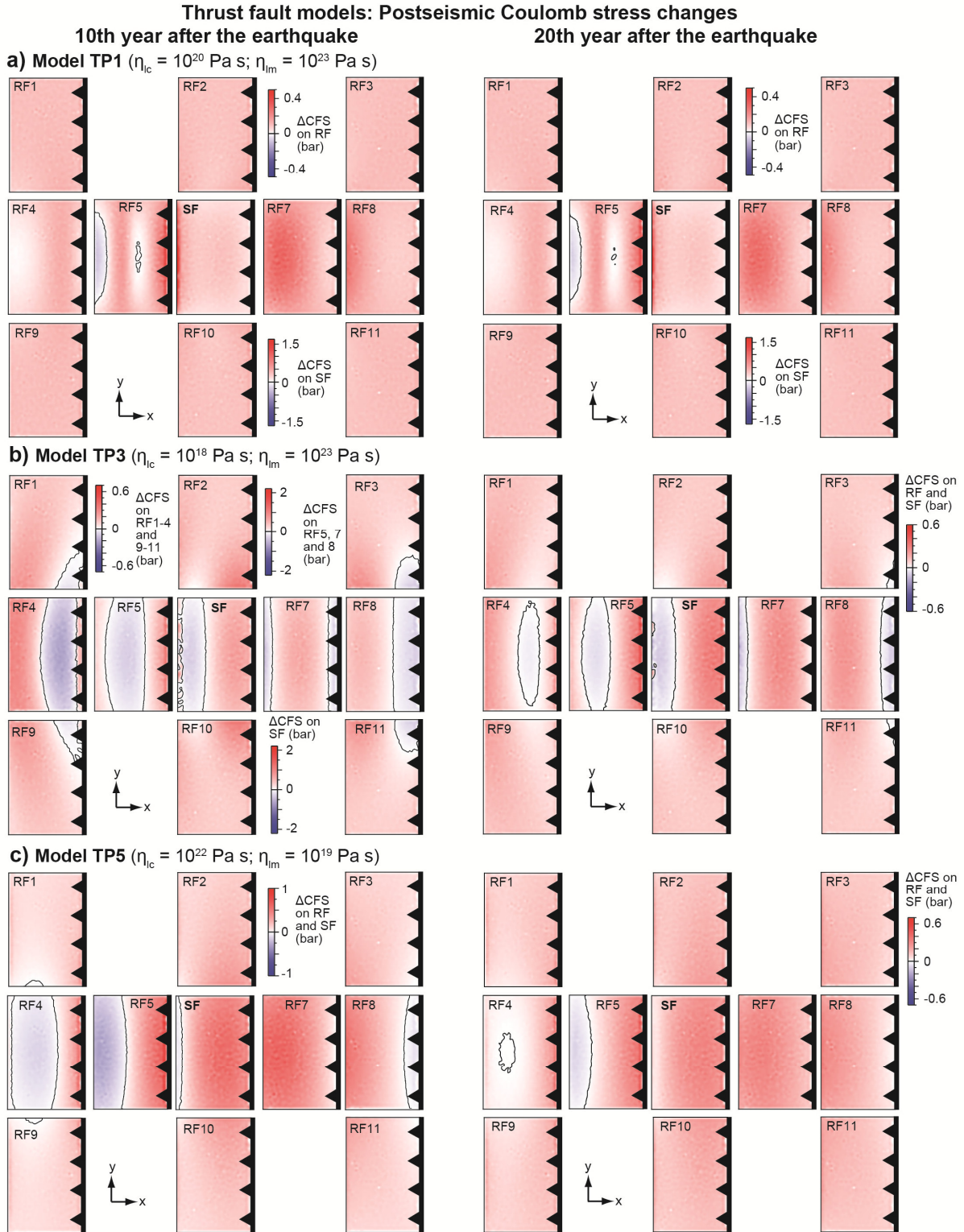
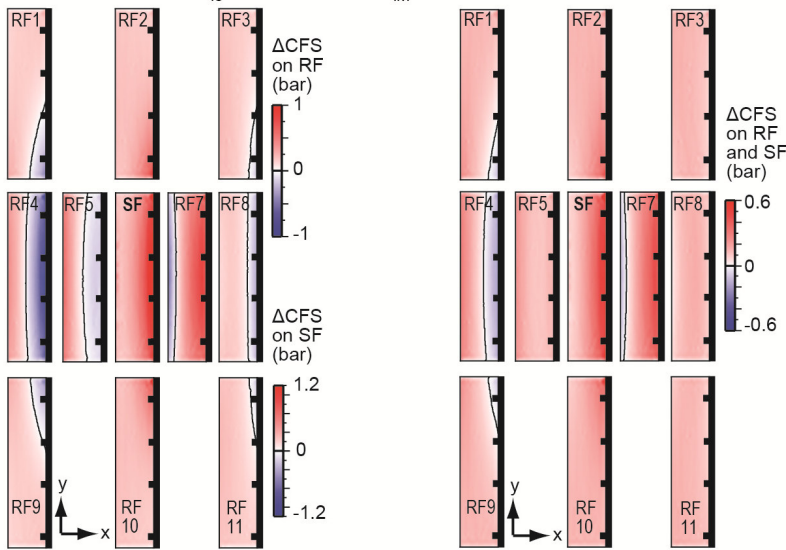


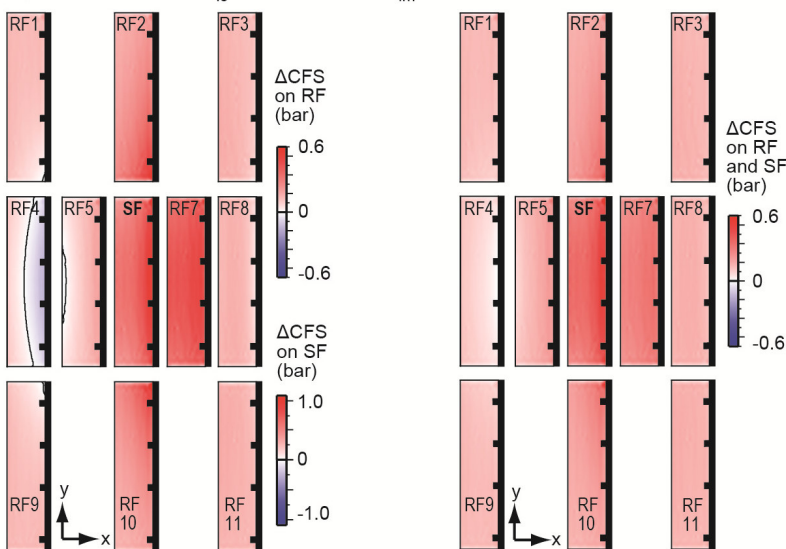
Figure 3.5: Postseismic Coulomb stress changes (ΔCFS) on receiver faults (RF) in the 10th and 20th year after the earthquake on the source fault (SF) as derived from thrust fault model (a) TP1 ($\eta_{lc} = 10^{20}$ Pa s; $\eta_{lm} = 10^{23}$ Pa s), (b) TP3 ($\eta_{lc} = 10^{18}$ Pa s; $\eta_{lm} = 10^{23}$ Pa s) and (c) TP5 ($\eta_{lc} = 10^{22}$ Pa s; $\eta_{lm} = 10^{19}$ Pa s). For results from models TP2, TP4 and TP6 see Figure 3.7. Note that the distance between the faults is not to scale. The distance in the x-direction between the fault surface traces is 15 km in the centre row (RF4-8) and 30 km in the upper (RF1-3) and lower (RF9-11) rows of the fault array. The distance in the y-direction is 5 km. Areas with positive Coulomb stress changes (red) and negative stress changes (blue) are separated by a black line where $\Delta CFS = 0$.

Normal fault models: Postseismic Coulomb stress changes 10th year after the earthquake 20th year after the earthquake

a) Model NP2 ($\eta_{lc} = 10^{18}$ Pa s; $\eta_{lm} = 10^{22}$ Pa s)



b) Model NP4 ($\eta_{lc} = 10^{21}$ Pa s; $\eta_{lm} = 10^{19}$ Pa s)



c) Model NP6 ($\eta_{lc} = 10^{22}$ Pa s; $\eta_{lm} = 10^{21}$ Pa s)

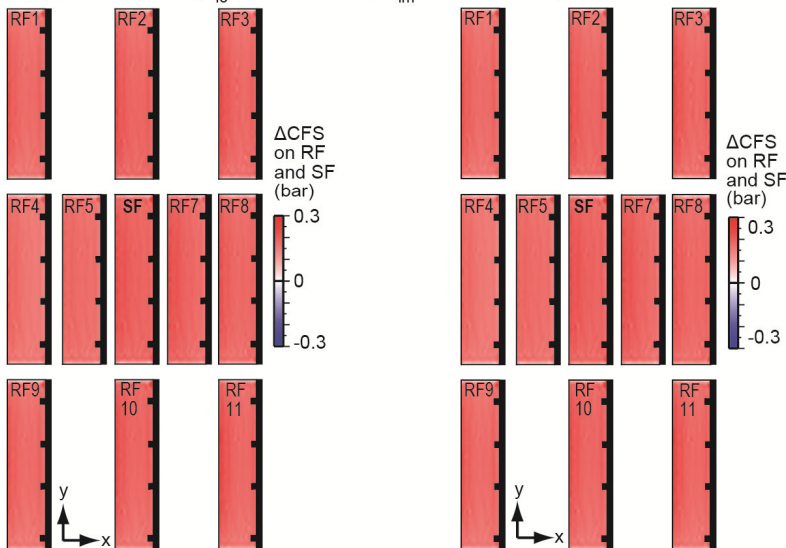


Figure 3.6: Postseismic Coulomb stress changes (Δ CFS) on receiver faults (RF) in the 10th and 20th year after the earthquake on the source fault (SF) as derived from normal fault model (a) NP2 ($\eta_{lc} = 10^{18}$ Pa s; $\eta_{lm} = 10^{22}$ Pa s), (b) NP4 ($\eta_{lc} = 10^{21}$ Pa s; $\eta_{lm} = 10^{19}$ Pa s) and (c) NP6 ($\eta_{lc} = 10^{22}$ Pa s; $\eta_{lm} = 10^{21}$ Pa s). Note that the distance between the faults is not to scale. The distance in the x -direction between the fault surface traces is 15 km in the centre row (RF4-8) and 30 km in the upper (RF1-3) and lower (RF9-11) rows of the fault array. The distance in the y -direction is 5 km. Areas with positive Coulomb stress changes (red) and negative stress changes (blue) are separated by a black line where Δ CFS = 0.

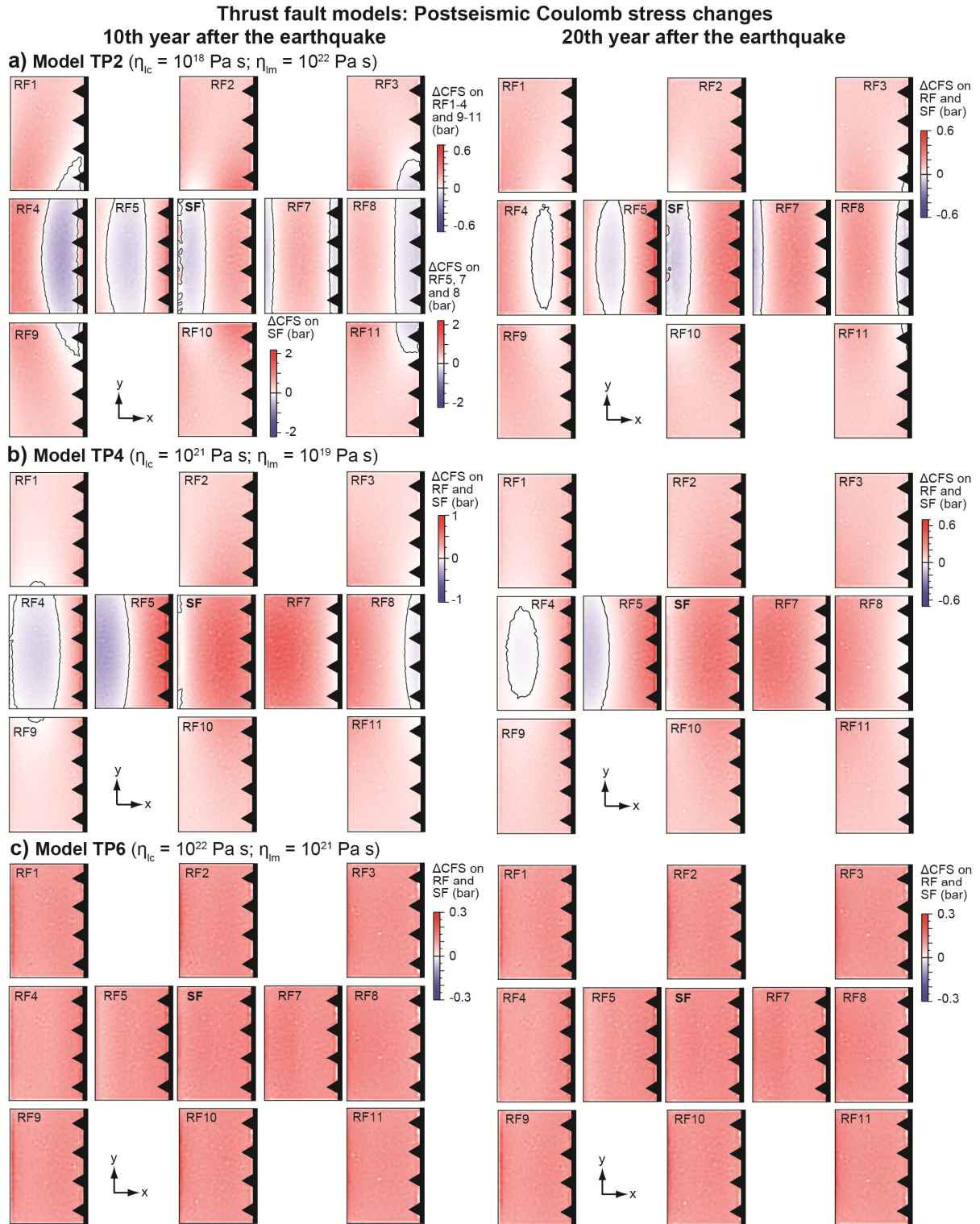


Figure 3.7: Postseismic Coulomb stress changes (ΔCFS) on receiver faults (RF) in the 10th and 20th year after the earthquake on the source fault (SF) as derived from thrust fault model (a) TP2 ($\eta_{lc} = 10^{18}$ Pa s; $\eta_{lm} = 10^{22}$ Pa s), (b) TP4 ($\eta_{lc} = 10^{21}$ Pa s; $\eta_{lm} = 10^{19}$ Pa s) and (c) TP6 ($\eta_{lc} = 10^{22}$ Pa s; $\eta_{lm} = 10^{21}$ Pa s). Note that the distance between the faults is not to scale. The distance in the x-direction between the fault surface traces is 15 km in the centre row (RF4-8) and 30 km in the upper (RF1-3) and lower (RF9-11) rows of the fault array. The distance in the y-direction is 5 km. Areas with positive Coulomb stress changes (red) and negative stress changes (blue) are separated by a black line where $\Delta CFS = 0$.

lower crust, the difference between the magnitudes of the stress changes in the first and 10th year is smaller. For example, the value of the stress decrease on both normal and thrust fault

RF4 changed from about -0.5 bar in the first year to -0.2 bar in the 10th year. The highest stress increase on the receiver faults during the 10th year occurs near the surface at the tips of RF2 and 10 (0.7 bar) in the normal fault model and on RF5 (1.0 bar) in the thrust fault model.

3.4 Discussion

Our three-dimensional finite-element models show that the postseismic Coulomb stress changes due to viscoelastic relaxation play an important role for the stress evolution on fault planes and hence the seismic hazard of a region. In our models, the maximum postseismic stress increase on the receiver faults has a value of up to 25 bar/a, which would be sufficient to trigger another earthquake. Together with the interseismic stress accumulation, the transient postseismic stress changes modify the static stress changes in a way that the net Coulomb stress changes on the receiver faults vary significantly through space and time. Depending on the viscosity of the lithospheric layers and the position of the receiver faults relative to the source fault, static stress shadow zones can, over time, turn into postseismic stress triggering zones and *vice versa*. The temporal evolution of the postseismic relaxation and stress changes are primarily controlled by the layer with the lowest viscosity. For viscosities of $\sim 10^{20}$ Pa s or less and the extension/shortening rates used in our models, transient stress changes outweigh the continuous stress increase of 0.1-0.2 bar/a due to interseismic strain accumulation for up to several decades, resulting in higher positive Coulomb stress changes or net negative stress changes on the individual receiver faults.

In the following, we discuss the differences between the coseismic and postseismic Coulomb stress changes and the differences between the normal and thrust fault models (Chapter 3.4.1). Also, we evaluate the influence of stress changes arising from viscoelastic relaxation and stress changes caused by the ongoing extension or shortening as well as the temporal evolution of stress changes and the influence of viscosity. In a second and third step, we link the Coulomb stress changes to the postseismic movements in the crust and lithospheric mantle to explain the obtained stress change distributions (Chapter 3.4.2) and compare our results with previous studies and examples from nature (Chapter 3.4.3).

3.4.1 Differences between coseismic and postseismic Coulomb stress changes on normal and thrust faults

As our model results show, considerable differences exist in the distribution of coseismic and postseismic stress changes. The coseismic stress changes are almost independent of the viscosity, whereas the postseismic stress changes strongly depend on this parameter. In the

coseismic phase, receiver faults in the along-strike direction of the source fault generally show a stress increase, while most receiver faults parallel to the source fault are dominated by negative stress changes (Fig. 3.1). In the postseismic phase, however, larger zones of positive stress changes develop on the receiver faults parallel to the source fault (Figs. 3.2, 3.3). Faults 2 and 10 generally show positive stress changes during both the coseismic and postseismic phases. On several other receiver faults, the distribution of postseismic stress triggering and shadow zones is inverse to the coseismic distribution. This is particularly pronounced in the models TP2 and TP3, e.g. where the upper part of faults RF3 and 11 undergo a coseismic stress decrease and a postseismic stress increase. Apart from the spatial pattern, coseismic and postseismic phases also differ with respect to the magnitude of the stress changes. Static stress changes on the receiver faults are in the range of -120 bar (thrust RF5) to +50 bar (normal RF5). Postseismic stress changes are generally smaller and strongly depend on the viscosity and on the time elapsed after the earthquake. For low viscosities, postseismic stress changes on receiver faults can reach maximum values of -30 bar/a (NP2/3, RF5) and +22 bar/a (TP2/3, RF5) in the first year.

Figure 3.8 illustrates how the transient stress changes due to viscoelastic relaxation evolve in different models over a time period of 100 years after the earthquake on the two receiver faults RF5 and 7. In models with low viscosity (NP3/TP3), high positive and negative Coulomb stress changes are observed during the initial postseismic phase, which decrease to the value of the interseismic stress change over a few decades. With the applied extension/shortening rate, the signal from the transient stress changes becomes negligible after ~30-40 years in the models NP3/TP3 and after ~40-50 years in the models NP5/TP5. Our results further show that the existence of a layer with low viscosity leads to high values of Coulomb stress changes, even if the other layer has a high viscosity.

Our models reveal that normal and thrust faults show remarkable differences in the postseismic stress change evolution (cf. Figs 3.4, 3.5), which can be mainly attributed to difference in fault dip. As shown by Bagge and Hampel (2015) for coseismic stress changes, a change in fault dip and hence the fault plane size leads to differences in the distribution of stress shadow and triggering zones on normal and thrust faults, whereas faults with the same dip (45°) show similar stress change patterns. With respect to the magnitude of the postseismic Coulomb stress changes, normal and thrust fault models with the same viscosity structure show the same order of magnitude, although the position of the highest stress changes may differ between the fault types.

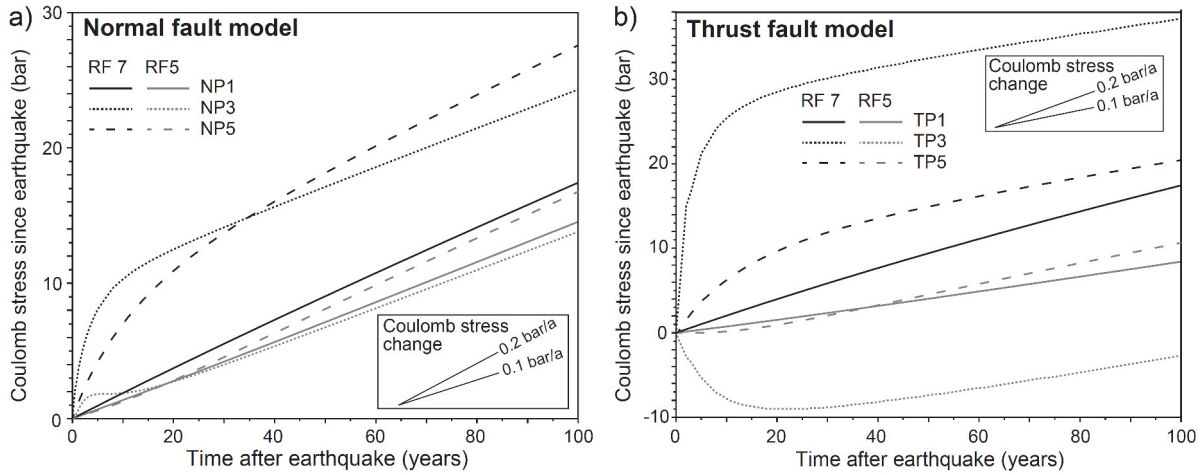


Figure 3.8: Temporal evolution of the postseismic Coulomb stress at the centres of faults RF5 and 7 for the (a) normal fault models NP1, NP3 and NP5 and (b) thrust fault models TP1, TP3 and TP5.

3.4.2 Relation between postseismic Coulomb stress changes and velocity fields

The spatio-temporal evolution of the postseismic Coulomb stress changes is linked to the postseismic movements in the lithosphere (e.g. Freed and Lin, 1998). Figure 3.9 shows the total postseismic velocity fields at different times after the earthquake for model cross-sections across the centre of the fault array (from RF4 to RF8) and illustrates how the transient movements induced by the coseismic slip evolve against the background of continuous extension or shortening. Generally, high positive or negative Coulomb stress changes occur where the postseismic movements in the footwall and hanging wall of a receiver fault result in a net relative movement that either promotes or acts against slip on the receiver fault, respectively.

In the models NP1/TP1 with a lower crust viscosity of 10^{20} Pa s and a lithospheric mantle viscosity of 10^{23} Pa s (Fig. 3.9a, b), three lobes with velocity anomalies occur near the downdip end of the source fault. The normal fault model shows two zones with increased velocities (up to 2.8 mm/a in the first year) at the boundary between upper and lower crust and a zone with decreased velocities in the down-dip prolongation of the fault plane. The spatial extent and magnitude of the positive velocity anomalies decrease slowly with time, affecting primarily the faults located in the nearby hanging wall and footwall of the source fault, whereas faults RF1-3 and 9-11 are hardly influenced (cf. Fig. 3.2). In the thrust fault model TP1, two lobes of decreased velocities emerge from the down-dip end of the source fault, which become more pronounced until the 20th year after the earthquake (Fig. 3.9b).

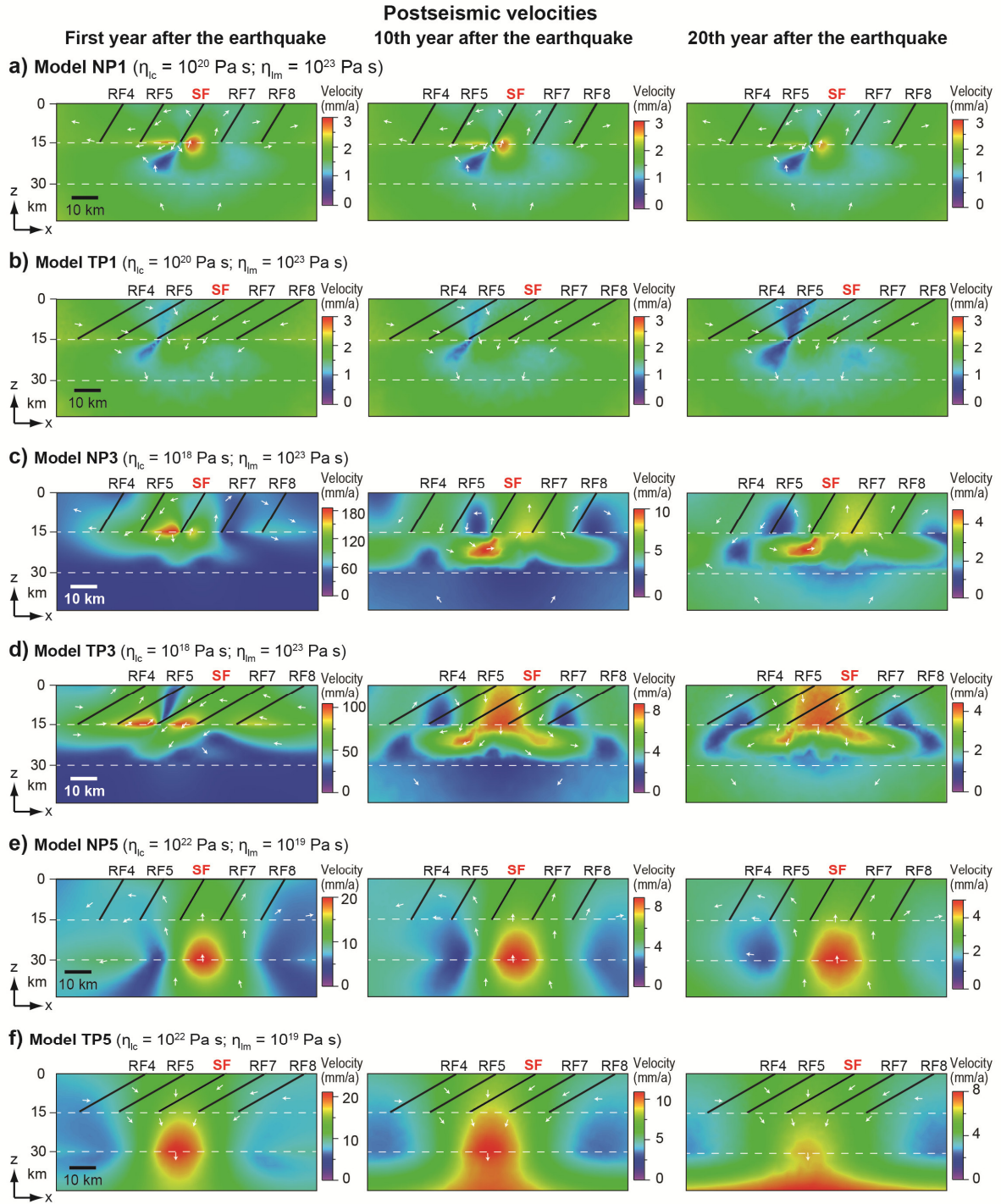


Figure 3.9: Total postseismic velocities in the first, 10th and 20th year after the earthquake shown in cross-sections across the centre of the fault array (from RF4 to RF8) for models (a) NP1, (b) TP1, (c) NP3, (d) TP3, (e) NP5 and (f) TP5, respectively. Schematic arrows show the direction of the postseismic movements. Note that only the central, upper part of the model is shown.

In the models with a low viscosity of the lower crust (NP3/TP3; Fig. 3.9c, d), velocities in the first year after the earthquake reach values of 185 mm/a in the normal fault model and 104 mm/a in the thrust fault model. The velocity perturbations occur across the entire width of the fault array. Over time, the postseismic velocities decrease but the perturbations still affect all receiver faults. At the beginning of the postseismic phase, the

largest velocity gradients occur around the down-dip end of the source fault. Until the 20th year after the earthquake, the zone with maximum velocities shifts into the lower crust in the normal fault model and into a wide zone in the footwall and hanging wall of the source fault in the thrust fault model. In contrast to models NP3/TP3, experiments with a low viscosity of the lithospheric mantle (NP5/TP5) show a broad, almost circular zone with maximum velocities of ~ 20 mm/a in the first year, which is centred on the boundary between lower crust and lithospheric mantle beneath the source fault footwall (Fig. 3.9e, f). In the normal fault model, the zone with high velocities slightly increases over time without significantly shifting its position. In the thrust fault model, however, the zone with high velocities increases in area and propagates into the lithospheric mantle until the highest velocities occur in a wide zone in the upper part of the lithospheric mantle in the 20th postseismic year. In both models, velocities remain elevated in the 20th year after the earthquake (NP5: ≤ 5 mm/a; TP5: ≤ 8 mm/a).

A comparison of the models, in which either the lower crust or the lithospheric mantle have the lowest viscosity, shows that the layer of the lowest viscosity controls where the highest postseismic velocities and hence the fastest relaxation occur in the first year after the earthquake. If the lower crust has a lower viscosity than the lithospheric mantle (Fig. 3.9a-d), the highest velocities are found in rather small zones near the down-dip end of the source fault at the transition zone between the upper and lower crust. If the lithospheric mantle has a lower viscosity than the lower crust, the zone with highest velocities is significantly larger and situated around the Moho (Fig. 3.9e, f).

3.4.3 Comparison with Coulomb stress patterns after natural earthquakes

The generalized setup of our models offers the opportunity to compare the derived principal patterns with postseismic Coulomb stress change patterns derived from models for specific natural earthquakes, where postseismic stress changes are influenced by local geological conditions. A prominent example of an earthquake, for which postseismic stress changes have been calculated, is the 2008 $M_w = 7.9$ Wenchuan (China) oblique thrust fault earthquake (Chen et al. 2011, Luo and Liu 2010, Nalbant and McCloskey 2011, Wang et al. 2014b). This earthquake probably triggered the 2013 $M_w = 6.6$ Lushan thrust earthquake, which occurred around 45 km southwest of the 2008 event (Wang et al. 2014b). The spatial relation between the faults ruptured by the two earthquakes is comparable to the position of our model receiver fault RF10 relative to the source fault. With respect to the viscosity structure, our model TP4 best matches the model used by Wang et al. (2014b). Combining our modelled coseismic

Coulomb stress changes (Fig. 3.1) with the results of model TP4 for the postseismic stress changes (Figs. 3.3, 3.7), we conclude that the fault ruptured by the Lushan earthquake experienced solely positive stress changes during and after the Wenchuan earthquake. For our $M_w \approx 7$ model earthquake, we obtain maximum static stress changes of ~ 30 bar and maximum postseismic stress changes of 0.7 and 0.4 bar in the first and tenth year after the earthquake, respectively. Our results generally agree with the predictions of positive static and postseismic stress changes (Luo and Liu 2010, Nalbant and McCloskey 2011, Parsons et al. 2008, Wang et al. 2014b) for this region, although the differences in earthquake magnitude, dip and size of the source fault and assumed lithospheric structure lead to different predictions for the stress change magnitudes. For example, Wang et al. (2014b) estimated a stress increase of 0.07 bar on the fault plane of the Lushan earthquake caused by 5 years of postseismic relaxation of the Wenchuan earthquake. Altogether, our model supports the conclusion that the Lushan earthquake was triggered by the Wenchuan earthquake. For other faults like the Longriba fault that is located in the hanging wall of the Longmenshan fault, Wang et al. (2014b) obtain a postseismic stress decrease. They evaluated the postseismic stress changes at a depth of 10 km and argue that only negligible variations occur in the depth range of 5-15 km. In our model TP4, stress shadow zones indeed occur in the lower parts of faults RF4, RF5 and RF9, but these faults also experience considerably high positive stress changes in other parts. This example underlines that it is crucial to consider the Coulomb stress change distribution on the whole fault plane.

Stress interaction between normal faults caused by viscoelastic relaxation has been investigated by Nostro et al. (2001) by using whole-Earth models with viscoelastic layers. They calculated the postseismic stress changes for the 1980 $M_w = 6.9$ Irpinia earthquake (southern Apennines) on a 60° -dipping source fault with a length of 35 km. Results were shown in map view for a depth of 17 km 100 years after the earthquake and as time-stress plots for a fixed point and a time interval of 1000 years after the earthquake. Similar to our models, the viscoelastic models by Nostro et al. (2001) show postseismic stress triggering zones in the along-strike direction of the source fault and alternating stress shadow and triggering zones in the hanging wall and footwall of the source fault. Based on a parameter study, in which Nostro et al. (2001) analysed the temporal evolution of the postseismic relaxation and the influence of the layer thickness and viscosity, but without considering background deformation, they concluded that the shallowest viscoelastic layer dominates the postseismic Coulomb stress changes. Our results additionally show that the layer with the lowest viscosity has the largest influence on the postseismic stress changes.

3.5 Conclusions

Three-dimensional finite-element modelling of the postseismic viscous flow in the lower crust and lithospheric mantle enables evaluating the spatiotemporal evolution of transient stress changes on intra-continental dip-slip faults and their dependence on the viscosity of the lithospheric layers. As experiments with different viscosity structures of the lithosphere show, the layer of the lowest viscosity has the strongest influence on postseismic Coulomb stress change patterns. Postseismic stress changes can modify static stress changes in a way that coseismic stress triggering zones can change to postseismic stress shadow zones and *vice versa*. On the other hand, the magnitude of both positive and negative coseismic stress changes can increase during the postseismic phase, implying that earthquakes on receiver faults can be additionally promoted or delayed. Our results also underline the importance of considering the combined effect of stress changes caused by the ongoing extension or shortening (leading to an interseismic stress increase) and by the postseismic relaxation (leading to stress increase or decrease). The relative contribution of postseismic relaxation and interseismic strain accumulation to the stress state on the receiver faults depends, among other factors like the regional deformation rate and the magnitude of the earthquake, on the location of the receiver fault relative to the source fault, the time elapsed after the earthquake, the fault dip and the viscosity.

4 Coulomb stress changes on the Wasatch fault (Utah)

(This chapter is based on the manuscript Bagge, Hampel and Gold, in prep.)

Abstract

The Wasatch fault zone (WFZ) constitutes the eastern boundary of the actively extending Basin and Range Province (Utah) and poses – as longest intra-continental normal fault in the United States and most active fault in Utah – a high seismic hazard for the population, e.g. in Salt Lake City. During the last ~7000 years, a series of earthquakes, partially $M \geq 7$ earthquakes, occurred on the WFZ and other nearby faults. Although the Wasatch fault zone is one of the best investigated fault zones, studies about Coulomb stress changes are still rare. Using three-dimensional finite-element models, we modelled the earthquake series of 25 single- and multi-rupture earthquakes during the last 6400 years on the segments of the central Wasatch fault zone, West Valley fault zone and Fremont-to-South-Oquirrh fault zone. To analyse the historic co- and postseismic Coulomb stress changes as well as the future evolution, we implied viscoelastic effects. Our results show that the influence of coseismic stress changes reaches all modelled fault zones with highest stress changes in a range of several tens of bar on adjacent faults and stress changes in a range of less than 1 bar on distal fault segments. Postseismic stress changes caused by viscoelastic relaxation dominate in the first year after an earthquake and decrease quickly in the first ten years. In the hundredth year, no significant effect of viscoelastic relaxation is observed. Modelled hypothetical present-day earthquakes suggest that present-day ruptures on the Brigham City segment or Salt Lake City segment could experience $M \sim 7.1$ or $M \sim 7.0$ earthquakes, respectively, which pose high seismic hazard for the metropolitan areas.

4.1 Introduction

The Wasatch fault zone (WFZ) in the actively extending Basin and Range Province (Utah) is a key example for an intra-continental normal fault with high seismic hazard. It is the longest active normal fault in the United States and the most active fault in Utah with an average Holocene slip rate of 1.3-2.0 mm/a (e.g. DuRoss and Hylland 2015, DuRoss et al. 2016, Machette et al. 1991). Nearly 80% of Utah's population lives in the region surrounding the Wasatch fault zone including Salt Lake City as the capital and most populated city (~190000 inhabitants) in Utah (Fig. 4.1). During the last ~7000 years, a series of earthquakes occurred on the WFZ and other nearby faults in the eastern Basin and Range Province, as shown by a comprehensive set of high-quality palaeo-seismic data (Chang and Smith 2002, Chang et al. 2006, DuRoss et al. 2016, 2011, DuRoss and Hylland 2015, Friedrich et al. 2003, Machette et al. 1991, Schwartz and Coppersmith 1984). During the Holocene, the different segments of the Wasatch fault zone (see Fig. 4.1) were ruptured by $M_w = 7.1-7.4$ earthquakes every ~400 years (Chang and Smith 2002, DuRoss et al. 2016, Machette et al. 1991, Malservisi et al. 2003, McCalpin and Nishenko 1996, Schwartz and Coppersmith 1984). It can be expected that devastating earthquakes will endanger the region around the Wasatch fault zone in the future.

According to the overall palaeo-seismic record, earthquakes on the fault segments of the Wasatch fault generally occurred in regular time intervals. In detail, some segments exhibited earthquake clusters as well as seismic gaps (DuRoss et al. 2016, Friedrich et al. 2003, McCalpin and Nishenko 1996, Schwartz and Coppersmith 1984). For example, a seismic gap exists for the Brigham City segment, which was not ruptured since 2400 years (DuRoss et al. 2016, Personius et al. 2012). The variability in timing of the Holocene earthquakes has been interpreted in terms of the Wallace-type recurrence model, which combines earthquake clustering on short timescales with uniform long-term strain accumulation (e.g. Malservisi et al. 2003, Wallace 1987). Compared to pre-Holocene earthquake record, the WFZ and neighbouring faults show an increase in their Holocene slip rates, probably as a response to the Late Pleistocene-Holocene regression of the Lake Bonneville (Oviatt et al. 1992), which caused isostatic rebound and stress changes in the eastern Basin and Range Province (Bills et al. 1994, Hetzel and Hampel 2005). A later three-dimensional numerical model by Karow and Hampel (2010) showed that the slip rates of the WFZ segments increased between the Bonneville highstand (~18 ka) and the Gilbert

transgression (~16 ka) and were constant during the Holocene but at a higher level than before the Lake Bonneville regression.

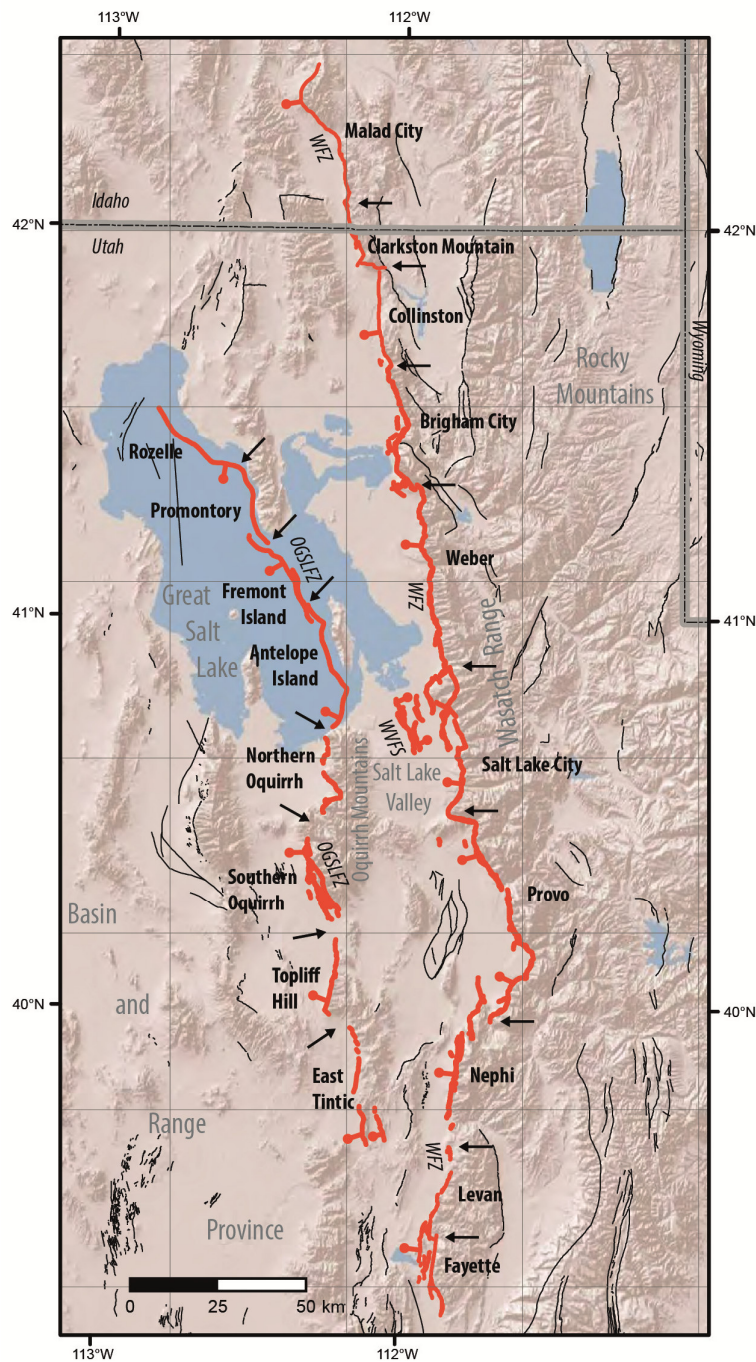


Figure 4.1: Overview of the Wasatch fault system in the eastern Basin and Range Province (Utah) by R. Gold (unpublished). Thin black lines mark quaternary active faults. Thick red lines mark the location and fault dip of primary faults: Oquirrh-Great Salt Lake fault zone (OGSLFZ), West Valley fault zone (WVZF) and Wasatch fault zone (WFZ). Fault trace data source: State of Utah (gis.utah.gov) & USGS (www.usgs.gov).

To assess the seismic hazard in the eastern Basin and Range Province, one of the crucial questions is how the WFZ segments interact with each other and with other faults in the vicinity (Fig. 4.1). Fault interaction between the Salt Lake City segment of the Wasatch fault and the antithetic West Valley fault zone west of the Wasatch fault was investigated by

DuRoss and Hylland (2015). Considering the time between the earthquakes and structural models of the fault zones, they assume that large earthquakes on the West Valley fault zone are linked to earthquakes on the Salt Lake City segment. Static Coulomb stress modelling of a scenario $M_w = 6.8$ earthquake on the Brigham City segment by Chang and Smith (2002) indicates stress decrease of up to -0.6 bar west of the Brigham City segment, whereas stress increase of up to 1.2 bar is observed on the Weber segment located in the along-strike prolongation of the Brigham City segment; an increase of stress that is sufficient to trigger another earthquake (King et al. 1994). A scenario $M_w = 7.1$ earthquake on the Provo segment implies a static stress increase of up to 1.2 bar on the Salt Lake City segment and of up to 4.0 bar on the Nephi segment, both segments are located in along-strike prolongation of the ruptured fault, whereas a nearby fault in the east is located in a stress shadow zone of up to -2 bar (Chang and Smith 2002). Although the Wasatch fault belongs to one of the best investigated fault zones (DuRoss et al. 2016, DuRoss and Hylland 2015, Chang et al. 2006, Machette et al. 1991), the database was rarely used for Coulomb stress analysis (e.g. Chang and Smith, 2002), possibly due to the lack of an historic earthquake on which Coulomb stress calculations are usually based. So far, postseismic Coulomb stress changes due to viscoelastic relaxation have not been modelled at all.

Here we present three-dimensional finite-element models to investigate the co- and postseismic Coulomb stress changes on the Wasatch fault segments and surrounding faults to analyse the interaction and stress transfer of the fault segments for high magnitude earthquakes during the last 6400 years. We consider viscoelastic relaxation, gravity and the regional deformation (extension) as constrained by GPS data (see Chapters 4.2-4.3). As in the general models of Chapters 1.3.1-1.3.2, slip on the faults is not prescribed but evolves freely as a function of the length of the preseismic phase, the rate of regional extension and the stress interaction between the faults. Because of the high quality of the available palaeo-seismic data, the modelled earthquake sequences can be evaluated in detail against the palaeo-seismic record to identify the most plausible model. This "best-fit" model will be used to analyse Coulomb stress changes for palaeo-earthquakes. Furthermore, the model will be used to analyse when the next $M \sim 7$ earthquake can be expected on the central segments of the WFZ.

4.2 Geological setting and earthquake history

The Wasatch fault zone as the most active fault in Utah is a ~ 350 km long, N-S striking and west dipping normal fault, which represents the eastern boundary of the ~ 700 km wide Basin

and Range Province and the western end of the uplifted Colorado Plateaus and the Middle Rocky Mountains (Gilbert 1928, Machette et al. 1991) (Fig. 4.1). The Salt Lake Valley, where smaller antithetic fault zones exist (West Valley fault zone, WVFZ), is bordered by the Wasatch Range and the Wasatch fault zone in the east and the Oquirrh Mountains in the west. The Oquirrh-Great Salt Lake fault zone (OGSLFZ) is located along the Oquirrh Mountains and below the Great Salt Lake.

The WFZ, OGSLFZ and the WVFZ are located in the eastern part of the Basin and Range Province and are controlled by an east-west extensional regime. Three GPS stations of the Basin and Range Geodetic Network (BARGEN) in the eastern part of the Basin and Range Province are CEDA (west), COON and HEBE (east). The 130 km wide region between CEDA and HEBE including three major normal faults (Wasatch fault zone, Oquirrh fault zone and Stansbury fault zone) is horizontally extended by a rate of 2.7 ± 0.4 mm/a (Friedrich et al. 2003, Niemi et al. 2004). Chang et al. (2006) determined a horizontal extension rate of 1.6 ± 0.4 mm/a for a 65 km wide area around the Wasatch fault.

Long normal fault zones as the Wasatch fault zone in the east as well as the Oquirrh-Great Salt Lake fault zone in the west commonly do not rupture as a whole fault but in several steps along their individual segments. Swan et al. (1980) and Schwartz and Coppersmith (1984) suggested that ruptures on the Wasatch fault take place on about at least six discrete fault segments. Based on palaeo-seismic data covering the last ~7000 years, DuRoss et al. (2016) defined five primary segments with recurrent Holocene surface-faulting earthquakes. These most active segments in the ~260 km long central part of the Wasatch fault zone are named from north to south: Brigham City segment (BCS), Weber segment (WS), Salt Lake City segment (SLCS), Provo segment (PS) and Nephi segment (NS) (Fig. 4.1). The lengths of the five Wasatch fault segments range between 35 and 56 km. In more detail, the segments of the central WFZ can be subdivided in further subsegments (DuRoss et al. 2016), which are not considered in the model for simplicity.

Similarly, the synthetic (west dipping) ~250 km long Oquirrh-Great Salt Lake fault zone, located ~25-50 km west of the Wasatch fault, is segmented and consists in the central part of the Fremont (FS), Antelope (AS), North-Oquirrh (NOS) and South-Oquirrh (SOS) segments (DuRoss et al. 2011, Olig et al. 1994) (Fig. 4.1). The Oquirrh fault in the south is about 21 km long and borders the Oquirrh Mountains. The 90 km long Great Salt Lake fault zone in the north is located under the Great Salt Lake and involves in the southern part the FS and AS. The West Valley fault zone (WVFZ) in the Salt Lake Valley by Salt Lake City

between the OGSLFZ and the WFZ includes the east dipping Granger fault zone (GFZ) and east dipping Taylorsville fault zone (TFZ) (DuRoss and Hylland 2015) (cf. Fig. 4.3b).

Major surface-rupturing earthquakes during the last ~7000 years on the central Wasatch fault zone occurred on one of the five central active faults with a recurrence rate of ~400 years and an average recurrence interval per segment in the range of 2000-4000 years (Machette et al. 1991). Figure 4.2 shows the earthquake timing probability functions for individual surface-faulting earthquakes at the central Wasatch fault zone by DuRoss et al. (2016). Using a segmented fault model they summarised some events resulting in a number of 24 earthquakes in the last ~7000 a for the five central Wasatch fault segments (Tab. 4.1): The Brigham City segment was ruptured at $5600 \text{ a} \pm 600 \text{ a}$ and at $4500 \text{ a} \pm 500 \text{ a}$, $3500 \text{ a} \pm 200 \text{ a}$ and $2400 \text{ a} \pm 300 \text{ a}$ with a mean vertical displacement of 1.7 m (1.2-2.1 m). The mean earthquake recurrence interval is $1100 \text{ a} \pm 200 \text{ a}$, whereas since 2400 a the segment did not rupture. The Weber segment, including a mean recurrence interval of $1300 \text{ a} \pm 100 \text{ a}$ experienced five earthquakes (at $5900 \text{ a} \pm 500 \text{ a}$, $4500 \text{ a} \pm 300 \text{ a}$, $3100 \text{ a} \pm 300 \text{ a}$, $1100 \text{ a} \pm 600 \text{ a}$ and $600 \text{ a} \pm 100 \text{ a}$) with a mean vertical displacement of 2.4 m (1.1-4.1 m). With the same mean recurrence interval of $1300 \text{ a} \pm 100 \text{ a}$ and a mean vertical displacement of 1.7 m (1.2-2.2 m), the Salt Lake City segment was ruptured at $5300 \text{ a} \pm 200 \text{ a}$, $4100 \text{ a} \pm 200 \text{ a}$, $2200 \text{ a} \pm 200 \text{ a}$ and $1300 \text{ a} \pm 200 \text{ a}$. At the Provo segment earthquakes occurred at $5900 \text{ a} \pm 100 \text{ a}$, $4700 \text{ a} \pm 300 \text{ a}$, $2200 \text{ a} \pm 400 \text{ a}$, $1500 \text{ a} \pm 400 \text{ a}$ and $600 \text{ a} \pm 50 \text{ a}$. The Provo segment and the Novo segment developed mean vertical displacements of 2.6 m (1.3-3.6 m) and 2.0 m (1.5-2.7 m) as well as mean recurrence intervals of $1300 \text{ a} \pm 200 \text{ a}$ and $1100 \text{ a} \pm 200 \text{ a}$, respectively. The Novo segment experienced six earthquakes at $5700 \text{ a} \pm 800 \text{ a}$, $4700 \text{ a} \pm 500 \text{ a}$, $4000 \text{ a} \pm 90 \text{ a}$, $2400 \text{ a} \pm 100 \text{ a}$, $1200 \text{ a} \pm 80 \text{ a}$ and $200 \text{ a} \pm 70 \text{ a}$. Based on the values for the vertical displacement and the recurrence interval the mean vertical slip rate is 1.6 mm/a (0.9-2.5 mm/a) on the BCS, 1.8 mm/a (0.8-3.4 mm/a) on WS, 1.3 mm/a (0.9-1.8 mm/a) on SLCS, 2.0 mm/a (0.8-3.3 mm/a) on PS and 1.8 mm/a (1.2-2.8 mm/a) on NS (DuRoss et al. 2016).

The mean vertical displacement for a Holocene earthquake on the West Valley fault zone (~0.5 m) is less than 50 % of the vertical displacement on the central Wasatch fault zone (DuRoss and Hylland 2015). Three earthquakes are documented for the last ~7000 years: at $5500 \text{ a} \pm 0.8 \text{ a}$ at the Granger fault, at $2200 \text{ a} \pm 0.2 \text{ a}$ at the Taylorsville fault and at $1400 \text{ a} \pm 0.7 \text{ a}$ again at the Granger fault, resulting in a mean recurrence interval of 2000 a for the WVFZ (DuRoss and Hylland 2015) and an average slip rate of 0.5-0.6 mm/a for the WVFZ (Keaton et al. 1993, Keaton and Currey 1993).

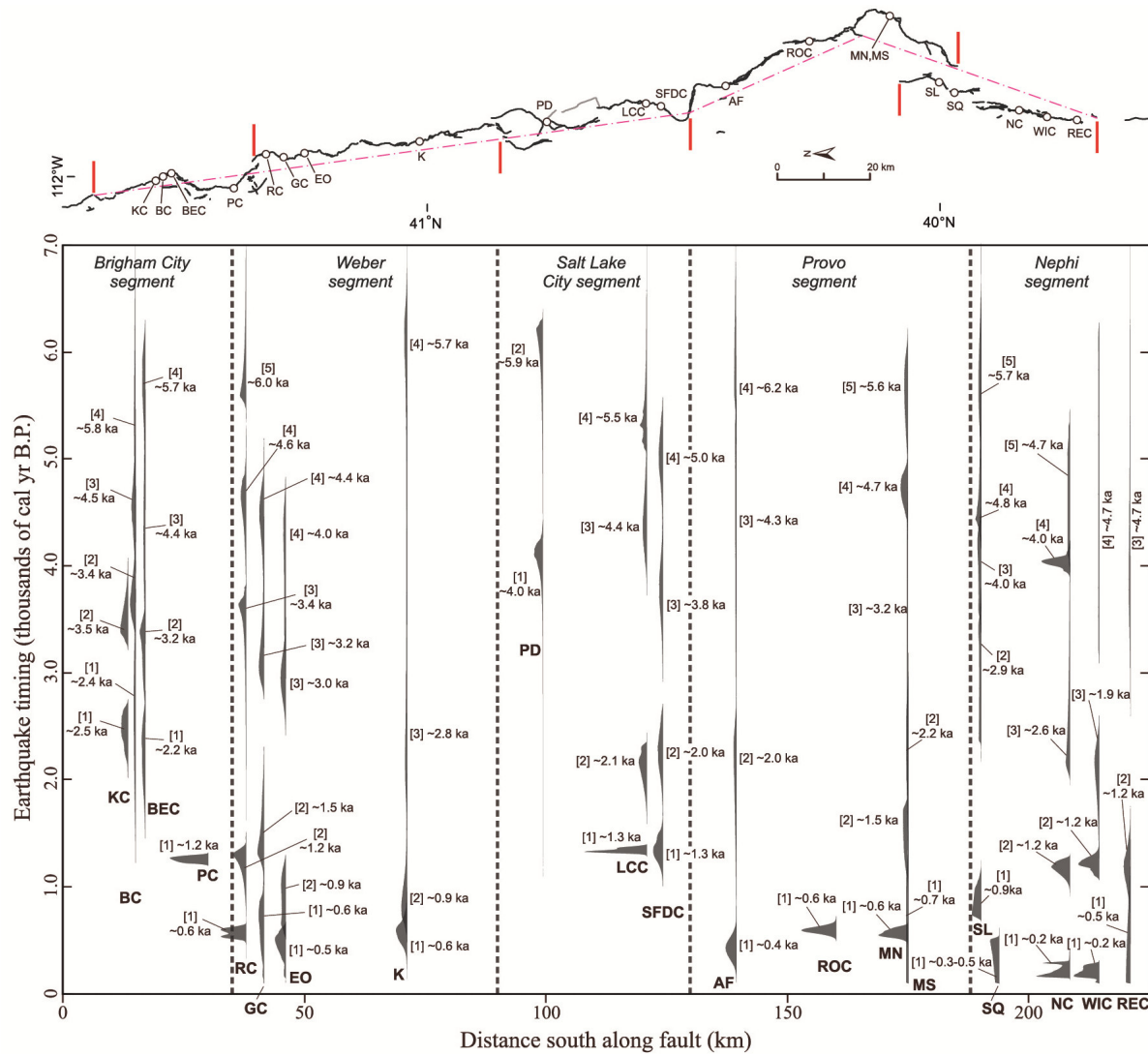


Figure 4.2: Earthquake timing probability density functions (PDFs) for individual surface-faulting earthquakes at the central Wasatch fault zone during the last 6400 a B.P. by DuRoss et al. (2016). Circles with labels mark the location of the event. Distance south along fault on the fault segments is mapped along simplified fault trace (pink line) shown in top panel (DuRoss et al. 2016).

At the North-Oquirrh segment the last earthquake occurred at 6300 a (4300-6900 a) with a vertical slip in a range of 2.0-2.7 m and an estimated slip rate of 0.1-0.2 mm/a (Olig et al. 1994, WGUEP 2016). The South-Oquirrh segment ruptured at 3000 a \pm 1900 a with a vertical slip between 1.3 and 2.2 m (Olig et al. 2001, WGUEP 2016). The Antelope segment (estimated vertical slip rate of 0.6 mm/a \pm 1.0/0.3) ruptured at 600 a \pm 240 a with a mean vertical displacement of 2.3 m \pm 0.6 m (Lund 2005). Lund (2005) assumed the same vertical slip rate of 0.3-1.6 mm/a and a recurrence interval of 1800-6600 a for the Fremont segment. During the last \sim 7000 a, the Antelope segment ruptured a second time at 6200 a \pm 240 a and the Fremont segment experienced also two earthquakes at 3150 a \pm 240 a and 6400 a \pm 200 a (WGUEP 2016). Due to the fragmentary palaeo-seismic data we inferred the same mean vertical slip of 2.3 m \pm 0.6 m for the second Antelope event and the two events on the related Fremont segment.

Table 4.1: List of 25 modelled earthquakes on the fault segments of the Fremont-to-South-Oquirrh fault zone, the WVFZ and the central Wasatch fault zone, which ruptured during the last 6400 a. Rupture events on the WVFZ include ruptures on both the Granger and Taylorsville fault zone. Time and observed mean vertical fault slip including uncertainties are based on DuRoss et al. (2016), DuRoss and Hylland (2015), WGUEP (2016), Lund (2005), Olig et al. (1994, 2001) and R. Gold personal communication. Because of a lack in palaeo-seismic data for the Fremont segment and the penultimate event of the Antelope segment we inferred the slip by the most recent Antelope segment. Modelled per event vertical fault slips are shown for models A-G (Mod A - Mod G), including the best fitting model H, which we used for further analysis in this study. Notice that the observed mean vertical fault slip is averaged over the last earthquakes and the modelled vertical fault slip describes the fault slip per event.

Model earthquake no.	Time B.P (a)	Time uncertainty (a)	Inter-seismic phase (a)	Ruptured fault segment	Observed mean vertical fault slip (m)			Modelled vertical fault slip (m)							
					min	max	pre-ferred	modelled slip < observed slip (min) modelled slip > observed slip (max) obs. slip (max) ≥ mod. slip ≥ obs. slip (min)							
								Mod A	Mod B	Mod C	Mod D	Mod E	Mod F	Mod G	Mod H
1	6400	±200	-	Fremont	1.7	2.9	2.3	1.6	1.1	1.3	2.4	1.6	1.5	1.4	1.3
2	6300	±1600	100	N-Oquirrh	2.0	2.7	2.2	2.2	1.5	1.2	3.2	2.2	2.0	1.9	1.7
3	6200	±240	100	Antelope	1.7	2.9	2.3	3.0	2.0	1.6	4.3	3.0	2.6	2.5	2.2
4	5900	±500	300	Weber	1.1	4.1	2.4	3.6	2.5	2.2	5.0	3.6	3.0	3.0	2.5
		±100		Provo	1.3	3.6	2.6	3.7	2.5	2.2	5.1	3.7	3.1	3.1	2.6
5	5700	±800	200	Nephi	1.5	2.7	2.0	4.0	2.7	2.5	5.4	4.0	3.3	3.4	2.8
6	5600	±600	100	Brigham	1.2	2.1	1.7	3.9	2.7	2.5	5.2	3.9	3.3	3.3	2.8
7	5500	±800	100	WVFZ	0.4	0.7	0.5	2.0	1.3	1.3	2.6	2.0	1.9	1.7	1.3
8	5300	±200	200	Salt Lake	1.2	2.2	1.7	4.4	3.0	3.0	5.8	4.4	3.7	3.7	3.1
9	4700	±300	600	Provo	1.3	3.6	2.6	2.4	1.6	2.2	2.6	2.4	2.3	2.0	1.9
		±500		Nephi	1.5	2.7	2.0	1.8	1.3	1.7	2.0	1.8	1.9	1.5	1.6
10	4500	±500	200	Brigham	1.2	2.1	1.7	1.8	1.2	1.7	1.9	1.8	1.8	1.5	1.6
		±300		Weber	1.1	4.1	2.4	2.7	1.9	2.5	2.9	2.7	2.6	2.3	2.2
11	4100	±200	400	Salt Lake	1.2	2.2	1.7	2.2	1.5	2.1	2.3	2.2	2.3	1.9	1.9
12	4000	±90	100	Nephi	1.5	2.7	2.0	1.2	0.8	1.2	1.2	1.2	1.3	1.0	1.1
13	3500	±200	500	Brigham	1.2	2.1	1.7	1.6	1.1	1.5	1.6	1.6	1.6	1.3	1.4
14	3150	±240	350	Freemont	1.7	2.9	2.3	2.5	1.7	2.5	2.6	2.5	2.4	2.1	2.0
15	3100	±300	50	Weber	1.1	4.1	2.4	2.4	1.7	2.4	2.4	2.4	2.4	1.4	2.0
16	3000	± 1900	100	S-Oquirrh	1.3	2.2	1.9	5.5	3.8	4.5	6.5	5.5	4.8	4.6	4.0
17	2400	±300	600	Brigham	1.2	2.1	1.7	1.7	1.2	1.7	1.7	1.7	1.7	1.4	1.5
		±100		Nephi	1.5	2.7	2.0	1.2	0.8	1.2	1.2	1.2	1.3	1.0	1.1
18	2200	±200	200	Salt Lake	1.2	2.2	1.7	2.9	2.0	2.9	3.0	2.9	2.9	2.5	2.5
		±400		Provo	1.3	3.6	2.6	4.0	2.8	4.0	4.0	4.0	3.7	3.4	3.2
		±200		WVFZ	0.4	0.7	0.5	2.2	1.5	2.2	2.2	2.2	2.3	1.9	1.9
19	1500	±400	700	Provo	1.3	3.6	2.6	1.5	1.0	1.5	1.5	1.5	1.6	1.2	1.4
20	1400	±700	100	WVFZ	0.4	0.7	0.5	0.8	0.5	0.8	0.8	0.8	0.8	0.6	0.7
21	1300	±200	100	Salt Lake	1.2	2.2	1.7	1.7	1.1	1.7	1.7	1.7	1.8	1.4	1.5
22	1200	±80	100	Nephi	1.5	2.7	2.0	2.1	1.5	2.1	2.1	2.1	2.1	1.8	1.8
23	1100	±600	100	Weber	1.1	4.1	2.4	3.4	2.4	3.4	3.4	3.4	3.3	2.9	2.8
24	600	±100	700	Weber	1.1	4.1	2.4	1.0	0.7	1.0	1.0	1.0	1.1	0.8	0.9
		±50		Provo	1.3	3.6	2.6	1.6	1.1	1.6	1.6	1.6	1.7	1.4	1.5
		±240		Antelope	1.7	2.9	2.3	6.9	4.8	6.9	7.0	6.9	6.0	5.8	5.1
25	200	±70	400	Nephi	1.5	2.7	2.0	1.7	1.2	1.7	1.7	1.7	1.8	1.4	1.5

4.3 Model setup

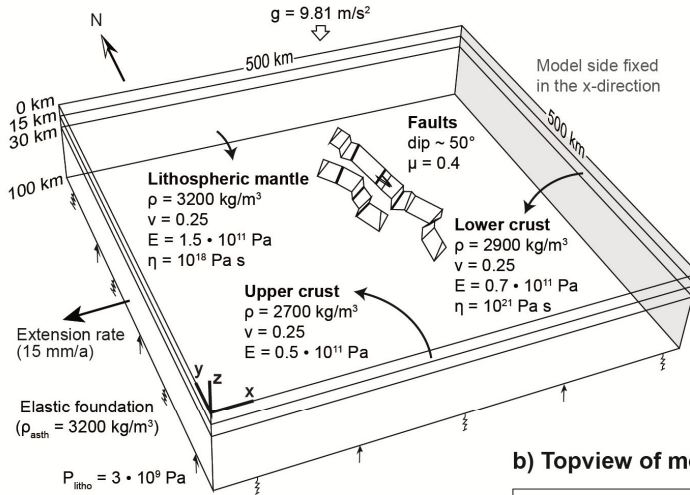
Using the commercial software Abaqus (version 6.14) we created three-dimensional finite-element models of a 100-km-thick intra-continental lithosphere representing the eastern part of the Basin and Range Province (Fig. 4.3). The model is 500 km x 500 km wide to avoid boundary effects in the region of the modelled fault zones. The lithosphere is divided into a 15-km-thick elastic upper crust, a 15-km-thick viscoelastic lower crust and a 70-km-thick viscoelastic lithospheric mantle. The rheological parameters of the layers (density ρ , Poisson's ratio ν , Young's modulus E and viscosity η) and the boundary conditions are shown in Figure 4.3a. Viscoelastic behaviour is implemented as linear, temperature-independent Maxwell viscoelasticity. We use a high lower crust viscosity of 10^{21} - 10^{22} Pa s and a low lithospheric mantle viscosity of 10^{18} Pa s, as it was used by Karow and Hampel (2010) and derived from transient crustal deformation models of the Basin and Range Province (Bills et al. 1994, Gourmelen and Amelung 2005, Kaufmann and Amelung 2000, Nishimura and Thatcher 2003).

The upper crust is cut by a normal fault system, which represents the central Wasatch fault zone, the central Oquirrh-Great Salt Lake fault zone (= Freemont-to-South-Oquirrh fault zone, FOFZ) and the West Valley fault zone (Fig. 4.3b). The West Valley fault zone westwards of the Salt Lake City segment is a fault system with a number of fault zones (see Fig. 4.1). We modelled two of these faults, the western Granger fault zone and the eastern Taylorsville fault zone. The central WFZ and the FOFZ are dipping with $\sim 50^\circ$ to the west and extend from the surface to the bottom of the upper crust, whereas the Granger fault zone and the Taylorsville fault zone are antithetic faults with a fault dip of $\sim 60^\circ$ to the east and extend from the surface to 6 km depth, where they are bordered by the SLCS. Fault dips between 45° and 60° are typical values for the faults in the eastern Basin and Range Province (Evans and Langrock 1994, Personius et al. 2012, Smith and Bruhn 1984) and have also been used in a previous model dedicated to the analysis of coseismic Coulomb stress changes (Chang and Smith 2002).

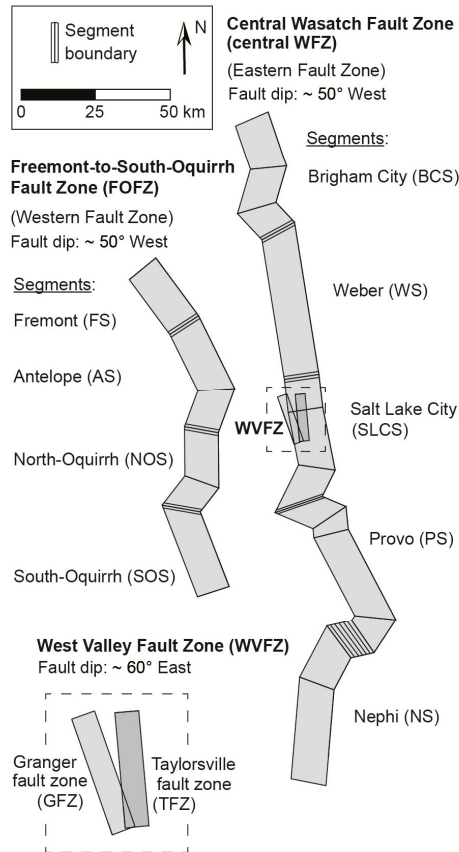
The fault segments of the central Wasatch fault zone and the Freemont-to-South-Oquirrh fault zone are separated by segment boundaries, which prohibit slip to ensure that only defined fault segments rupture during a model earthquake. The model earthquakes are determined at defined points in time by changing the source fault (= fault which ruptured during earthquake) properties from locked to unlock, which leads to sudden slip. Note that the slip distribution is not prescribed but develops self-consistently in accordance with the strain accumulated during the preseismic phase. Slip initiation is controlled by the Mohr-Coulomb

criterion $|\tau_{\max}| = c + \mu\sigma_n$, where τ_{\max} is the critical shear stress, c is the cohesion (zero in our model), σ_n is the normal stress and μ the coefficient of friction (0.3-0.4 in our model). All models are meshed by linear tetrahedral elements with an edge length of 1 km near the faults, which increases to 10 km at the model margins.

a) Setup of finite-element-model



b) Topview of modelled fault segmentation



c) Map with modelled fault segments

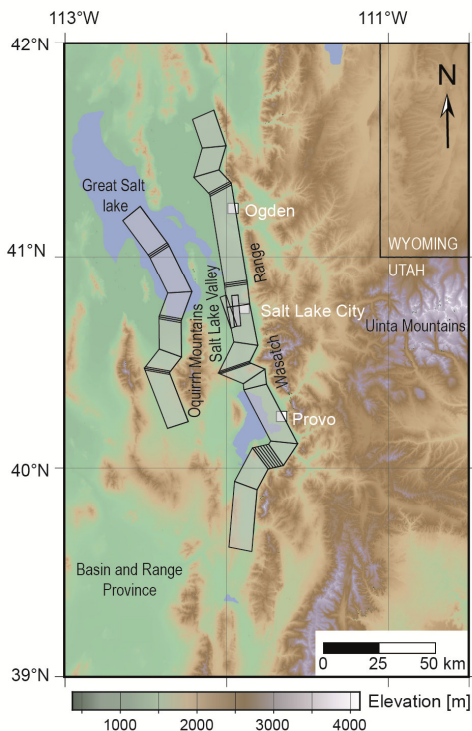


Figure 4.3: Model setup. (a) Perspective view of the three-dimensional finite-element model of the Wasatch fault. The lithosphere is divided in the upper crust, the lower crust and the lithospheric mantle. The faults are embedded in the upper crust. A velocity boundary condition is applied to one of the yz-model sides, whereas the other yz-model side is fixed in the x-direction to extend the model at a total rate of 15 mm/a, which initiates slip on the faults. Abbreviations are ρ density, E Young's modulus, ν Poisson's ratio, η viscosity, g acceleration due to gravity, P_{litho} lithostatic pressure and ρ_{asth} density of the asthenosphere. (b) Topview of the modelled fault segments of the central Wasatch fault zone as well as the Fremont-to-South-Oquirrh fault zone and two faults in the West Valley area. (c) Topographic map and the projected modelled fault zones.

A model run consists of quasi-static analysis steps and starts with the implementation of gravity as body force (9.81 m/s^2), a lithostatic pressure ($3 \times 10^9 \text{ Pa}$) and an elastic foundation to the model bottom to establish an isostatic equilibrium. Afterwards the model is extended throughout the remaining model time to generate the background deformation. The extension is applied at one of the yz-sides, whereas the other yz-side is fixed in the x-direction (see Hampel and Hetzel 2015, same effect as if extension is applied on both model sides). Considering the vertical direction, the model sides and the model bottom are free to move. The model sides in the xz-plane are fixed in the y-direction. To reach a constant fault slip rate, all faults are unlocked during the model is extended. To achieve typical fault slip rates of $\sim 0.5 \text{ mm/a}$ and $\sim 1\text{-}2 \text{ mm/a}$ at the modelled WVFZ and central WFZ, respectively (DuRoss and Hylland 2015, DuRoss et al. 2016), we applied an extension rate of 12-18 mm/a (Tab. 4.2). For our 500 km wide model extension rates between 9 and 15 mm/a correspond to slip rates of $1.6 \pm 0.4 \text{ mm/a}$ determined by Chang et al. (2006) for a 65 km wide area around the Wasatch fault zone. After all faults have reached a constant slip rate, the earthquakes cycles start, by alternating pre-/inter and coseismic phases. During the preseismic phases all faults are locked for stress accumulation. In the coseismic phases the source fault is unlocked to perform coseismic slip ("model earthquake"). Based on the data from DuRoss et al. (2016), DuRoss and Hylland (2015), WGUEP (2016), Lund (2005), Olig et al. (1994, 2001) and R. Gold personal communication, we modelled altogether 25 model earthquakes with different fault slip, magnitude and different time intervals between the earthquakes (Tab. 4.1). In some of the model earthquakes more than one fault segment ruptured (altogether 32 model rupture events).

By changing some parameters in the models, we try finding the best fitting model, where the observed and modelled coseismic slip on the fault segments has minor deviations. Model A is defined by a regional extension rate of 18 mm/a, a 2000 a long first preseismic phase, a coefficient of friction of $\mu = 0.4$ and a lower crust viscosity of $\eta_{lc} = 10^{22} \text{ Pa s}$. Six variation models B to G differ in one of these parameters from model A. Model B has an extension rate of 12 mm/a instead of 18 mm/a, whereas the other parameters remain unchanged. Model C (1000 a) and Model D (3000 a) differ in the time of the first preseismic phase from Model A. Model E has a coefficient of friction of $\mu = 0.3$ and Model F a lower crust viscosity of $\eta_{lc} = 10^{21} \text{ Pa s}$. Model G is defined by a regional extension rate of 15 mm/a, a 2000 a long first preseismic phase, a coefficient of friction of $\mu = 0.4$ and a lower crust viscosity of $\eta_{lc} = 10^{22} \text{ Pa s}$. Model H has the same properties as Model G except for a lower crust viscosity of $\eta_{lc} = 10^{21} \text{ Pa s}$.

In our study, we calculated the co- and postseismic Coulomb stress changes on the fault planes. The Coulomb stress change ΔCFS is defined by $\Delta\text{CFS} = \Delta\tau - \mu'\Delta\sigma_n$, where $\Delta\tau$ is the change in shear stress (positive in direction of source fault slip), μ' is the effective coefficient of friction and $\Delta\sigma_n$ is the change in normal stress (positive if fault is clamped) (e.g. Freed 2005, Stein et al. 1992, Stein 1999, 2003). A positive stress change implies that normal faulting slip is promoted on faults in the direction given by the regional stress field. In contrast, a negative Coulomb stress change means that normal faulting slip in the direction given by the regional stress field is hampered.

Table 4.2: Vertical fault slip rate on fault segments in our models and observed by DuRoss et al. (2016), DuRoss and Hylland (2015), Keaton et al. (1993), Keaton and Currey (2013), Lund (2005) and Olig et al. (1994). Observed vertical fault slip rates are averaged over the last earthquakes. Modelled vertical fault slip rate is the constant slip rate, which is established before the earthquake cycles start. Models differ in extension rate of 12 mm/a (Mod B), 15 mm/a (Mod H) and 18 mm/a (Mod A).

Fault segment	Observed vertical fault slip rate (mm/a)			Modelled vertical fault slip rate (mm/a)		
	min	max	preferred	Mod B	Mod H	Mod A
Fremont	0.3	1.6	0.6	0.6	0.7	0.9
Antelope	0.3	1.6	0.6	1.0	1.2	1.4
North-Oquirrh	0.1	0.2	0.15	0.8	1.0	1.2
South-Oquirrh				0.8	1.0	1.1
Brigham City	0.9	2.5	1.6	1.1	1.3	1.6
Weber	0.8	3.4	1.8	1.2	1.5	1.8
Salt Lake City	0.9	1.8	1.3	1.1	1.4	1.6
Provo	0.8	3.3	2.0	1.2	1.5	1.8
Nephi	1.2	2.8	1.8	1.2	1.4	1.7
WVZ (total)	0.5	0.6	0.55	0.4	0.6	0.7

4.4 Model results

4.4.1 Vertical fault slip per event and vertical fault slip rate over 6400 a

Table 4.1 provides an overview of the palaeo-seismological record and preferred, minimum and maximum estimates of the vertical fault slip for each earthquake based on the available literature. Also shown is the modelled vertical slip per event on each fault segment for all models. The vertical slip is calculated by modelled slip in down-dip direction on the fault using a fault dip of 50° for eastern and western fault zones and a dip of 60° for the WVZ.

To achieve a good fit between observed and modelled fault slip, we varied the extension rate, the length of the first preseismic phase, the friction coefficient and the viscosity of the lower crust. The differences between these models are documented in

Table 4.1. Overall the modelled and observed fault slips are in remarkably good agreement, except for a few outliers: In all models, the coseismic slip is too high for the first Brigham City event, the first and second WVFZ events, the South-Oquirrh event and the second Antelope event, whereas the third and fourth Nephi and the fifth Weber event show less slip than observed. Changing the time of the first preseismic phase increases the per-event slip in case of a longer preseismic phase, in contrast to a shorter preseismic phase, which decreases the slip per event. The influence of the time of the first preseismic phase decreases with the number of earthquakes per segment. Using a time of 1000 a (Model C) or 3000 a (Model D) instead of a 2000 a (Model A) for the first preseismic phase leads to a significant change in slip of the first and second event on each fault segment. For example, the first Weber event experiences a vertical fault slip of 3.6 m in Model A, 2.2 m in Model C and 5.0 m in Model D. The third event per segment is only affected within the range of centimeters. Experiments with a friction coefficient of $\mu = 0.3$ (Model A) instead of $\mu = 0.4$ (Model E) show no significant changes in the per-event slip. The extension rate has crucial influence on both the amount and rate of slip. Higher regional extension rates result in higher vertical slip rates and coseismic slip. An increase in extension rate from 12 mm/a to 15 mm/a and from 15 mm/a to 18 mm/a causes an increase in vertical slip rate by the factor of 1.2 (120%), respectively. Comparing Model A (extension rate of 18 mm/a), Model G (15 mm/a) and Model B (12 mm/a) shows that an extension rate of 12 mm/a delivers partially too small per event fault slip and an extension rate of 18 mm/a delivers partially too high per event fault slip. The best fit is obtained for an extension rate of 15 mm/a across the 500 km wide model, which is at the upper limit of the extension rate reported by Chang et al. (2006) for the Wasatch region (Models G, H). The modelled vertical fault slip rates and the observed vertical fault slip rates are well matched (Tab. 4.2). Exceptions are the Oquirrh segments, on which the modelled slip rate of 0.8-1.2 mm/a is higher than the observed slip rate of 0.1-0.2 mm/a (Olig et al. 1994). Apart from the extension rate, the viscosity of the lower crust influences the coseismic slip. Using a lower crust viscosity of 10^{21} Pa s (Models F, H) instead of 10^{22} Pa s (Models A, G) improves the vertical fault slip for several events. Considering all parameters, we determined Model H as the best fitting model, which we use for the following analysis of fault interaction and calculation of Coulomb stress changes.

4.4.2 Coulomb stress changes

In principle, our models enable the calculation of Coulomb stress changes on many different time scales and for any individual fault segment. In the following analysis, we focus on four

different kinds of investigations: First, we analyse Coulomb stress changes since the last earthquake per segment (Chapter 4.4.2.1; Fig. 4.4). Second, co- and postseismic Coulomb stress changes for the 4100 a SLCS event (Chapter 4.4.2.2; Fig. 4.5). Third, Coulomb stress changes and postseismic velocities from the last earthquake (200 a event on Nephi segment) (Chapter 4.4.2.3 and 4.4.3; Figs. 4.6 and 4.7) Finally, we analyse in Chapter 4.4.4 (Fig. 4.8, Tab. 4.3) the future evolution and magnitudes of hypothetical earthquakes. The background deformation, which is always present, causes a continuous Coulomb stress increase of ~ 0.19 bar/a on the central WFZ, of ~ 0.13 - 0.17 bar/a on the FOFZ and of ~ 0.12 - 0.14 bar/a on the WVFZ. Stress increase due to background deformation is superposed by the positive and negative stress changes caused by sudden coseismic slip and postseismic viscoelastic relaxation.

Depending on the magnitude of the coseismic slip, the coseismic stress drop on the source fault can reach several hundred bar (Figs. 4.5, 4.6), for example the earthquake at 4100 a with a vertical slip of 1.9 m on the SLCS exhibits a coseismic stress drop of ~ 400 bar. Apart from the coseismic stress drop, the magnitude of the co- and postseismic stress changes depends on the magnitude of the coseismic slip. Independent of the location of the source fault, an earthquake on the source fault causes coseismic stress changes on all remaining faults in our model. In general, high positive stress changes arise in the along-strike direction of the source fault while high negative stress changes occur parallel to the source fault (e.g. 4100 a SLSC earthquake). The highest coseismic stress changes occur on receiver faults near to the source fault and reach up to -160 bar and $+75$ bar during the 4100 a SLSC earthquake and -1.8 bar and $+17$ bar in case of the 200 a Nephi earthquake (coseismic slip of 1.5 m, stress drop of 318 bar). The Brigham City segment and the Fremont segment are less affected with small static stress changes of ~ 0.1 bar. Postseismic stress changes are highest in the first year after the earthquake and decrease fast in the first postseismic decade. The magnitude of the postseismic stress changes depends on the coseismic slip and the considered time interval.

4.4.2.1 Coulomb stress changes since last earthquake per segment

First, we calculated the stress changes since the last earthquake on an individual segment (Fig. 4.4). The stress changes include interseismic stress increase as well as co- and postseismic stress changes by surrounding earthquakes. Since the last earthquake on the Brigham City segment 2400 a years ago stress build up of up to 783 bar develops on the Brigham City segment, which is the highest on the central WFZ. Since 1300 a (last earthquake on the SLCS), a stress increase of up to 514 bar occurs on the SLCS. The Weber

and Provo segments have accumulated stress of 371 bar and 340 bar, respectively, since the last earthquake 600 years ago. The Nephi segment, which ruptured 200 years ago as the last palaeo-earthquake in this study, exhibits the smallest stress increase of up to 106 bar. Since 1400 years the WVFZ exhibits a stress increase of 189 bar on the Granger fault zone and 227 bar on the Taylorsville fault zone. The stress changes since the last earthquake on the Fremont-to-South-Oquirrh fault zone range between 436 bar on the Antelope segment (600 a), 687 bar on the Fremont segment (3150 a), 864 bar on the South-Oquirrh segment (300 a) and 1100 bar on the North-Oquirrh segment (6300 a).

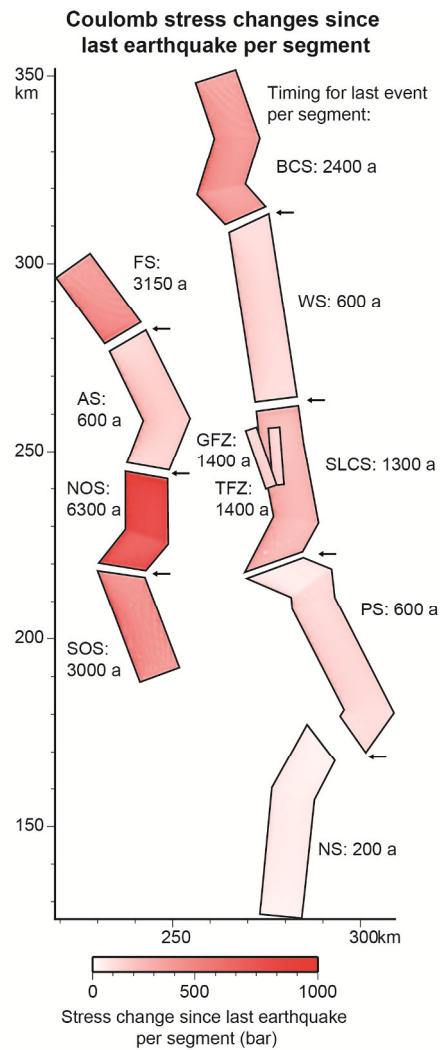


Figure 4.4: Coulomb stress changes (ΔCFS) since last earthquake on the (a) BCS for a time interval of 2400 a, (b) WB for a time interval of 600 a, (c) SLCS for a time interval of 1300 a, (d) PS for a time interval of 600 a and (e) NS for a time interval of 200 a. Arrows indicate segment boundaries.

4.4.2.2 Co- and postseismic Coulomb stress changes for the 4100 a SLCS event

To evaluate one of the palaeo-earthquakes in more detail, we have chosen the 4100 a event on the SLCS. Considering the earthquake on the SLCS 4100 a ago, the calculation of static Coulomb stress changes suggests high stress increase on adjacent fault segments in along-strike direction of the source fault (Fig. 4.5a). The Weber and Provo segments exhibit stress increase of up to 75 bar and 67 bar on the fault tips near the source fault. Similarly, the Brigham City and Nephi segments are totally located in stress triggering zones (up to ~ 0.8 bar). Stress shadow zones are located at the WVFZ, the Antelope (-18 bar) and Oquirrh fault zones (up to -17 bar) with highest stress decrease of -161 bar on the Taylorsville fault zone. The surface area of the Granger fault zone exhibits a small zone of stress increase (18 bar). Also the Fremont fault zone and the distal fault tips of the Antelope and South-Oquirrh fault zones (~ 1 bar) are located in a stress triggering zone. The coseismic stress drop on the source fault (SLCS) reaches ~ 400 bar.

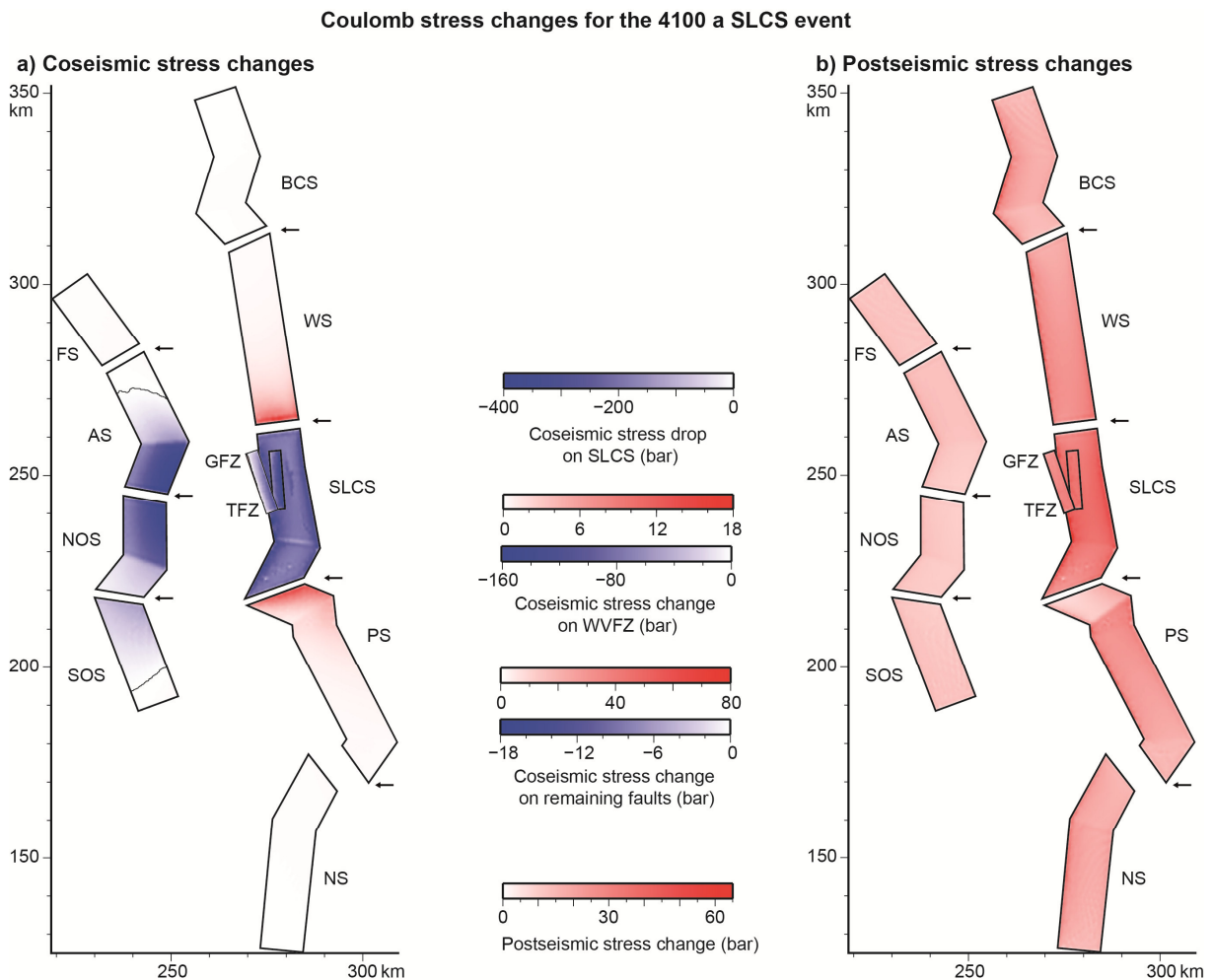


Figure 4.5: (a) Co- and (b) postseismic Coulomb stress changes (ΔCFS) for the 4100 a SLCS event. Postseismic stress changes are shown for a time interval of 100 a and include interseismic stress increase. Arrows indicate segment boundaries.

Next to the coseismic stress changes, the 4100 a SLCS event produces postseismic stress changes on the fault zones (Fig. 4.5b). Considering the next 100 a after the SLCS earthquake (including inter- and postseismic, excluding static stress changes) the SLCS exhibits 65 bar of stress increase. With increasing distance along-strike of the source fault, the maximum stress changes on the fault segments decrease by up to 43 bar on the Brigham City segment and 36 bar on the Nephi segment. Maximum stress changes on the WVFZ range between 42 bar on the Taylorsville fault zone and 31 bar on the Granger fault zone. On the Fremont-to-South-Oquirrh fault zone stress changes from 13 bar to 18 bar occur.

4.4.2.3 Co- and postseismic Coulomb stress changes from last earthquake (200 a event on Nephi segment)

The most recent earthquake in the Wasatch region occurred 200 a ago on the Nephi segment (NS). This earthquake with a coseismic stress drop of 318 bar leads to positive and negative static stress changes on all receiver faults (Fig. 4.6a). Except the Antelope segment, which is completely located in a stress shadow zone, all receiver faults are located both in stress triggering and shadow zones. Stress shadow zones generally occur at the lower part of the fault segments. The highest static stress increases are found at the southern fault tip of the Provo segment (17 bar) and at the southern part of the South-Oquirrh segment (1.1 bar), which are both located near the source fault. The highest stress decrease occurs at the lower part of the Antelope segment (-1.8 bar) and at the lower part of the Weber segment (-1.3 bar). Positive and negative stress changes on the other faults are lower than 1 bar.

Postseismic stress changes between the 200 a Nephi earthquake and today indicate a high stress increase of 106 bar on the Nephi segment (Fig. 4.6b). Maxima of stress changes are generally located in the lower parts of the fault planes. High postseismic stress increase also occurs at the Antelope segment (115 bar), the Weber segment (103 bar), the Provo segment (96 bar) and the SLCS (57 bar). The other fault segments exhibit positive stress changes between 25 bar (Granger fault zone) and 42 bar (Brigham City segment).

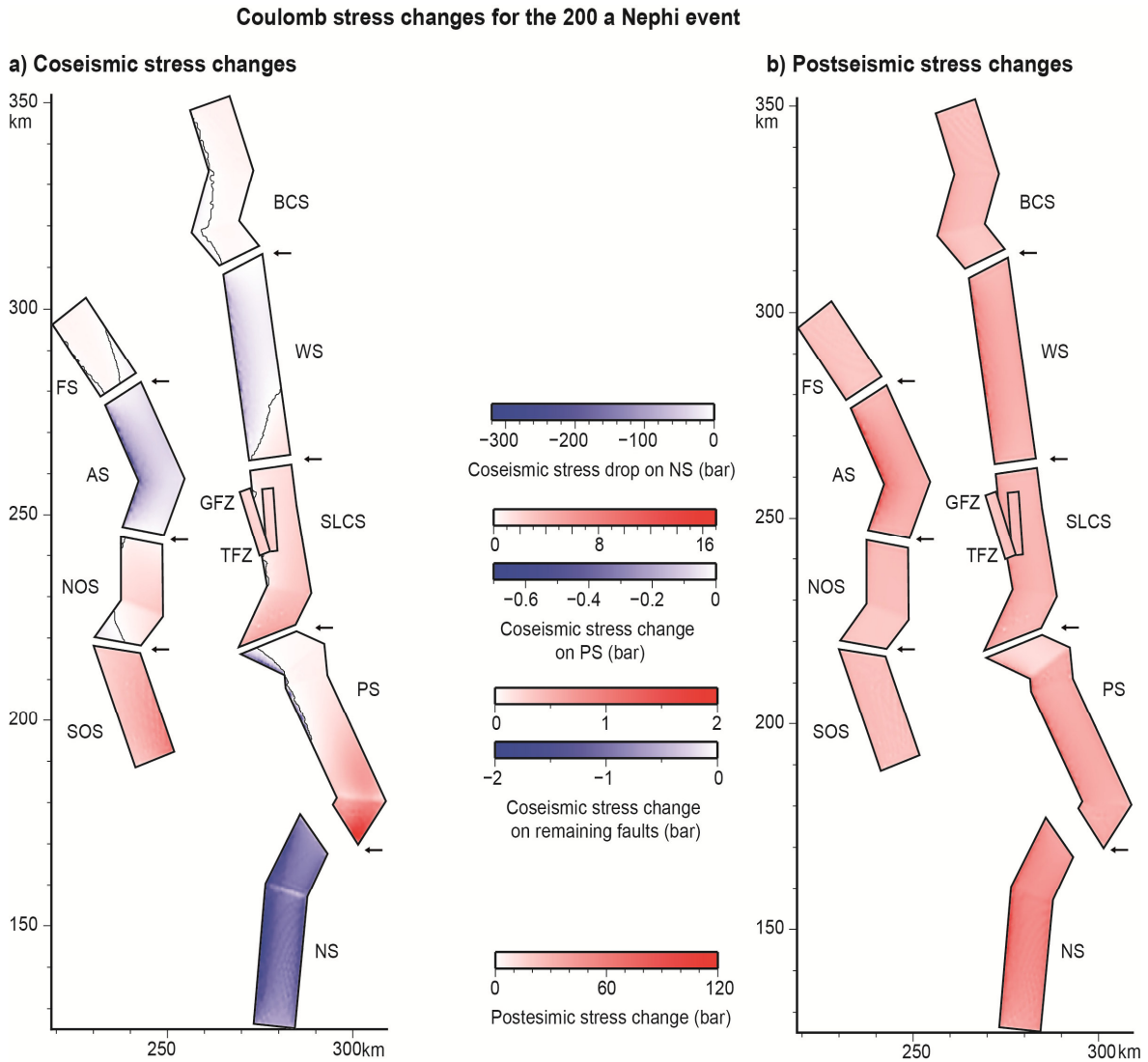


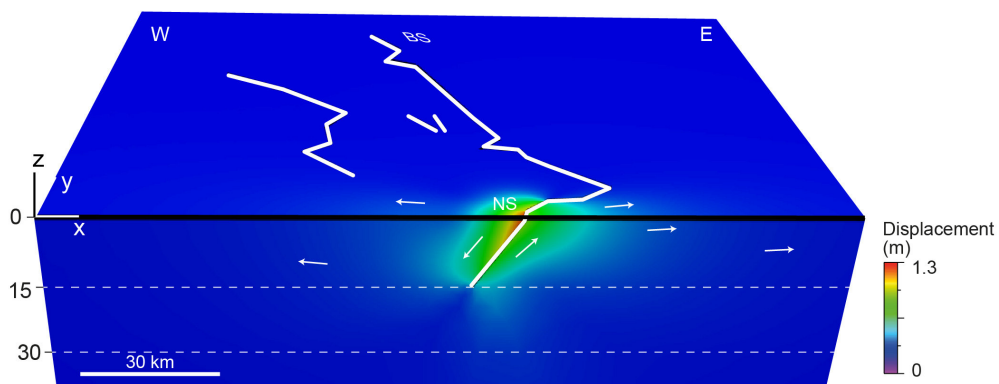
Figure 4.6: (a) Co- and (b) postseismic Coulomb stress changes (ΔCFS) for the 200 a Nephi event. Postseismic stress changes are shown for a time interval of 200 a and include interseismic stress increase. Arrows indicate segment boundaries.

4.4.3 Co- and postseismic velocities from last earthquake (200 a event on Nephi segment)

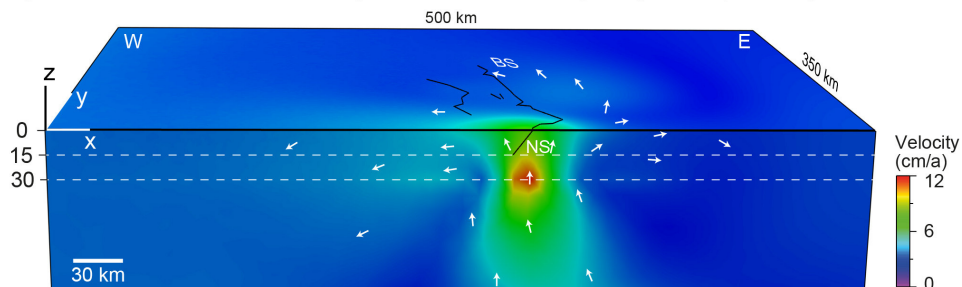
Fig. 4.7 shows the coseismic displacements and the postseismic velocities at the model surface and as cross-section across the centre of the Nephi segment. The coseismic displacement, with maximum displacement of 1.3 m in the hanging wall, illustrates footwall uplift and hanging wall subsidence in agreement with observations from normal faults (Fig. 4.7a). Considering the postseismic phase, two effects – the postseismic relaxation and the interseismic stress increase – are superposed, which both influence the postseismic velocities. In the first year of the postseismic phase, the highest velocities (12 cm/a) with upward motion are located in the transition zone between the lower crust and lithospheric mantle in the footwall of the Nephi segment (below the fault zone) (Fig. 4.7b). The velocities

strongly decrease in the first five years after the earthquake. In the second and third years the maximum velocity is still found below the Nephi fault zone, but decreases from 6.5 cm/a in the second year to 4.0 cm/a in the third year. In the tenth year velocities of 1.0 cm are present in the area below the Nephi fault zone. In the hundredth year after the Nephi earthquake the velocity field is affected by the regional extension of the model (Fig. 4.7c). Since the velocity boundary condition is applied on the western end of the model whereas the eastern end is fixed, the velocities increase from east to west. The velocities caused by the regional extension range between 0.5 cm and 0.8 cm in the area of the fault zones.

a) Coseismic displacement (200 a Nephi event)



b) Postseismic velocities in the first year after the last earthquake (200 a Nephi event)



c) Postseismic velocities in the hundredth year after the last earthquake (200 a Nephi event)

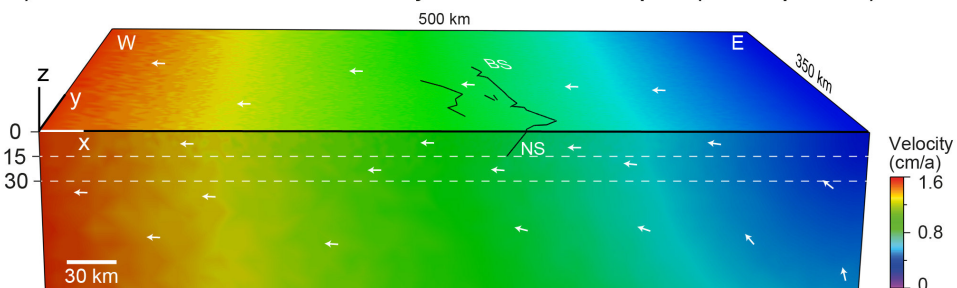


Figure 4.7: Total (a) coseismic velocities as well as postseismic velocities in the (b) first and (c) hundredth year after the Nephi earthquake at 200 a shown in cross-sections across the centre of the Nephi segment and at the model surface. Schematic arrows show the direction of the postseismic movements.

4.4.4 Model predictions on present-day and future fault slip and surface displacements

To evaluate the magnitude of a hypothetical present-day earthquake on the faults in the Wasatch region, we unlocked each model fault segment at the end of the model run. Table 4.3 shows the magnitude and vertical fault slip of a present-day scenario earthquake per segment. The magnitude is calculated by $M = 6.69 + 0.74 * \log(S)$, while S is the slip on the fault plane (Wells and Coppersmith 1994). Based on the obtained coseismic slip, the Brigham City segment would exhibit a magnitude 7.1 and the Salt Lake City segment an earthquake of magnitude 7.0 today. Figure 4.8 shows the modelled coseismic displacements for the hypothetical present-day earthquakes on the SLCS and the BCS. The modelled earthquake on the SLCS leads to surface uplift of < 0.3 m in the footwall and to subsidence of up to 1.5 m in the hanging wall, the maximum total horizontal displacement is 0.9 m. The model earthquake on the BCS causes higher displacements with maximum coseismic uplift and subsidence of 1.1 m and 2.4 m, respectively, with maximum horizontal displacements of 1.7 m. Modelled present-day ruptures of the Fremont segment and of the Oquirrh segments exhibit a magnitude 7.0 to 7.3 (Tab. 4.3). For the segments of the central Wasatch fault zone, which would exhibit a present-day magnitude 6.5 to 6.8 earthquake, we expanded the model time into the future, to analyse when the segments would experience magnitude 7 earthquakes. The model results suggest that the next $M \sim 7$ earthquake with a vertical fault slip of ~ 1.8 m can be expected after ~ 800 a, ~ 900 a and ~ 1400 a on the Provo, Weber and Nephi segments, respectively.

Table 4.3: Vertical fault slip and magnitude of a hypothetical present-day earthquake on the fault segments, respectively. Magnitude is calculated by $M = 6.69 + 0.74 * \log(S)$, while S is the slip on the fault plane (Wells and Coppersmith 1994).

Fault segment	Hypothetical present-day earthquake	
	vertical fault slip (m)	magnitude
Fremont	2.2	7.0
Antelope	1.2	6.8
North-Oquirrh	5.1	7.3
South-Oquirrh	2.8	7.1
Brigham City	2.8	7.1
Weber	0.9	6.8
Salt Lake City	1.8	7.0
Provo	1.0	6.8
Nephi	0.4	6.5
Granger	0.3	6.4
Taylorsville	0.4	6.5
WVFF (total)	0.7	6.7

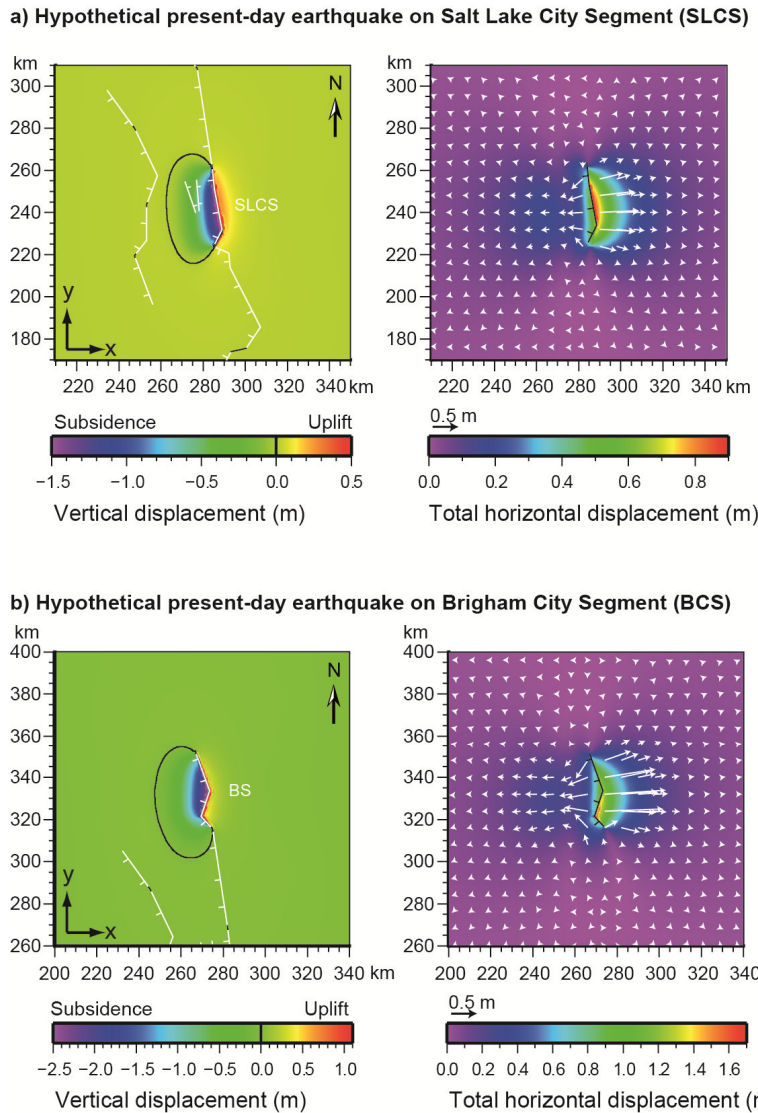


Figure 4.8: Coseismic displacements shown in map view for the central part of the model surface. Vertical and total horizontal displacement for a hypothetical present-day earthquake on the (a) SLCS and (b) BCS.

4.5 Discussion

4.5.1 Discussion of the model

Our three-dimensional finite-element model of the central Wasatch fault region includes 25 palaeo-earthquakes of the last 6400 years at the central WFZ and surrounded fault zones. Except for some events, our model delivers reasonably good agreement with the palaeo-seismological record (Tab. 4.1). Deviations between nature and our model can be caused by a variety of factors. Apart from the model parameters themselves, discrepancies arise due to the (partly large) uncertainties in the age and slip of the palaeo-earthquakes.

For identifying a best fitting model, we used the documented mean earthquake time from literature (c.f. Tab. 4.1 and references therein). The used mean earthquake time has uncertainties of tens to thousands of years (Fig. 4.2, Tab. 4.1). Highest uncertainties in our

models exist for the North- and South-Oquirrh earthquakes with uncertainties of 1600 a and 1900 a, respectively. An example for a well dated earthquake is the $600 \text{ a} \pm 50 \text{ a}$ event at the Provo segment. Potentially our models could be improved by changing the per-event earthquake time within the uncertainties. Resulting from the interseismic stress increase, a shorter time interval between two earthquakes leads to smaller fault slip for the second event, while the fault slip of the second event is increased by a longer time interval. For example, the modelled 3000 a South-Oquirrh event exhibits too high vertical fault slip (4.0 m instead of preferred 1.9 m), so that an earthquake timing several hundred years earlier seems to be more likely. In contrast, the 6300 a North-Oquirrh segment exhibits less vertical slip (1.7 m) than observed, which may imply that the earthquake has occurred several hundred years later. This is also indicated by the extremely high modelled stress increase since the last earthquake on the North-Oquirrh segment. A later event would reduce the accumulated stress increase since the last earthquake until today.

The WVFZ generally shows too much fault slip in the model, especially for the 5500 a event and the 2200 a event. As reference value for our study, we used a mean vertical fault slip of 0.5 m (DuRoss and Hylland, 2015). In contrast, Keaton et al. (1993) suggest an average per-event vertical displacement of 1.2-1.5 m for the WVFZ, which would be more compatible with our modelled fault slip of the 5500 a event and the 2200 a event. The high vertical fault slip of the 2200 a event of 1.9 m may be related to the long time interval of the 5500 a event and the accumulated stress in this time interval. As comparison, the short time interval between the 2200 a event and the 1400 a event leads to a modelled fault slip of 0.7 m.

For our study we used a simplified fault geometry including a fault dip of $\sim 50^\circ$ for the central WFZ and the FOFZ, whereas in nature the fault geometry is more complicated, e.g. the fault dip of the SLCS is 50° at the surface and 30° in depth (DuRoss and Hylland 2015). The simplified fault geometry could be one reason for deviations of the determined fault slips from nature. Furthermore, in our models we can define the timing of an earthquake by changing the boundary condition of the fault from locked to unlocked. This means that the earthquake timing is not determined by the stress situation on the fault zone. During the model earthquake (30 seconds) the stress drop and the fault slip develops freely. In nature more complicated fault geometry could lead to a different stress build up due to a different fault slip distribution. Details in real fault geometry may lead to incomplete coseismic fault slip on the fault plane resulting in smaller fault slip, less release of accumulated stress and the next earthquake could occur earlier as usually. For example, the 1100 a and 600 a Weber events as well as the 2200 a and 1500 a Provo events indicate a relative short time interval.

Our models with simplified fault geometry may neglect an incomplete fault slip and residual stress on fault planes. This could be related to the small fault slip of the 1500 a Provo event (1.4 m) in our model, which releases the residual stress caused by incomplete coseismic slip of the 2200 a Provo event. In this case, the consideration of more details in the fault geometry or a shorter coseismic phase may further improve the model.

The mean vertical fault slip from literature used for finding the best fitting model in this study is in most cases the mean vertical fault slip per segment over several earthquakes. For example, the mean vertical fault slip by DuRoss et al. (2016) is determined over a time interval of ~7000 a for the five Wasatch fault segments, respectively. Therefore, the vertical fault slip per event differs from the mean vertical fault slip per segment. Hence we used the whole uncertainty range of the mean vertical fault slip for the comparison with the modelled coseismic fault slip. Considering the documented vertical fault slip in each event (if available) for the time adaption in our models, may improve the best fitting model in this study.

An important fact in analysing earthquake cycles and the stress evolution over several thousand years is that, apart from the high magnitude earthquakes, also smaller earthquakes may occur, which are not modelled in our study, but also influence the stress situation on the fault planes. For this case it is advantageous to use the mean fault slip per fault segment including the sum of all fault slips in the considered time interval. A model including only high magnitude earthquakes and no small magnitude earthquakes, which had arisen in nature, generally delivers higher fault slips for the modelled earthquakes resulting in higher stress changes.

In our study we used a segmentation model including five segments of the central Wasatch fault zone. Fault segmentation and the existence of segment boundaries are often discussed for the Wasatch fault (Chang and Smith 2002, DuRoss et al. 2016, Machette et al. 1991, Schwartz and Coppersmith 1984). Observations of large earthquakes show that multisegment-ruptures can occur with a transfer across boundaries to neighbouring fault segments. A multisegment-rupture model of the Wasatch fault zone including fewer earthquakes generally shows smaller vertical fault slips per event for longer rupture lengths compared to a single-rupture model (Chang and Smith 2002, DuRoss et al. 2016, Machette et al. 1991, Schwartz and Coppersmith 1984). Based on palaeo-seismological data Chang and Smith (2002) prefer a multisegment-rupture model for the analysis of large earthquakes on the central Wasatch fault zone because almost all of the large, historical normal-faulting earthquakes in the Intermountain Seismic Belt were multisegmented. In contrast, the investigation of the fault segmentation and the quantification of uncertainties in segment

boundaries by DuRoss et al. (2016) shows that more complex ruptures than the usually used segment lengths are possible and they suggest a segmented fault model, which is applied to our study.

Our single-rupture model shows a dominant coseismic stress transfer on fault tips of adjacent fault segments (c.f. Figs. 4.5a, 4.6a) with high magnitudes of stress increase (e.g. 75 bar of coseismic stress increase on WS by the 4100 a SLCS event) that may trigger another earthquake on adjacent fault segments and may initiate a multisegment-rupture. In our models, the single ruptures of the fault segments are limited by segment boundaries. Because the planes of the segment boundaries do not slip the entire time of the earthquake cycles, high stress in a range of hundredths of MPa accumulates on the segment boundary plane during the series of earthquake cycles. The analysis and comparison of a multisegment-rupture model by changing the segment boundary conditions, so that they can slip during multisegment-ruptures, would be useful to offer another point of view for the analysis of Coulomb stress changes and for the analysis of the fault segmentation on the Wasatch fault zone.

4.5.2 Discussion of co- and postseismic stress transfer and the influence of viscoelastic relaxation

Our three-dimensional finite-element model of the central Wasatch fault region enables the calculation of co- and postseismic palaeo-Coulomb stress changes for the last 6400 years as well as the future evolution. The calculation of stress changes gives information about the range of stress transfer and interaction of the fault segments. Coseismic stress transfer is generally highest near the source fault, but also ranges over several hundredths of kilometres. For example, the 200 a Nephi event influenced all considered faults by static stress transfer, even if the effect on the ~120 km distant Fremont segment is smaller than 0.1 bar. The stress transfer acts both in along-strike direction of the source fault and in its hanging wall and footwall. For example, the highest stress transfer of the 4100 a SLSC event occurs on the WVFZ by -161 bar, whereas highest static stress increase of up to 75 bar is located at the fault tips of neighbored faults near the SLCS. Thereby the magnitude of coseismic stress changes is in the range of a few percent of the coseismic stress drop, as it is often shown for coseismic stress change calculation of normal faulting earthquakes (Nostro et al. 1997, Ryder et al. 2012). Comparing stress increase per segment since the last earthquake with the coseismic stress drop, our model shows that the coseismic stress drop is generally lower than the accumulated stress since the last earthquake. For example, the stress increase since the last

earthquake on SLCS is 514 bar and on the BCS 783 bar, whereas the coseismic stress drop for a hypothetical present-day earthquake is -404 bar on the SLCS and -589 bar on the BCS.

Our models show that the postseismic relaxation effects the stress situation during the last 6400 years on the Wasatch fault region and hence the seismic hazard. The postseismic stress transfer by viscoelastic relaxation, which is superposed by the interseismic stress increase, has a lower magnitude and a lower spatial expansion than the static stress changes, but the temporal expansion acts over several years. Considering the part of the relaxation, the postseismic stress changes amount several percent of the coseismic stress changes. Postseismic stress increase is highest on the source fault and generally decreases with increasing distance (e.g. Figs. 4.5b, 4.6b). Exceptions are the WS and AS, which experience high postseismic stress changes of the 200 a Nephi event, although they aren't adjacent faults. The analysis of the spatial expansion of the postseismic stress changes shows that not all faults are influenced by the postseismic relaxation. For example, the 4100 a SLCS event produces no significant amount of postseismic stress changes on the Fremont-to-South-Oquirrh fault zone. The postseismic stress increase results from the applied regional stress field (Fig. 4.5b). The 200 a Nephi event primarily effects the Provo segment by postseismic relaxation (Figs. 4.6b, 4.8b).

The effect of viscoelastic relaxation decreases fast in the first years after the earthquake (c.f. Fig. 4.8). More than 90 % of the postseismic relaxation took place in the first five postseismic years. Ten years after the earthquake the lithosphere is hardly effected by the relaxation and in the hundredths year no effect of relaxation is observed and the interseismic stress increase by the regional stress field dominates. The fast decrease of the postseismic relaxation is due to the low viscosity of the lithospheric mantle of 10^{18} Pa s. Investigating the postseismic deformation for earthquakes in the northern Basin and Range Province, Nishimura and Thatcher (2003) also determined fast relaxation time (~ 15 a) assuming a viscosity of the asthenosphere of 4×10^{18} Pa s. The fact that the lithospheric mantle viscosity is lower than the lower crust viscosity, leads to a high concentration of the highest velocities and viscoelastic relaxation on a zone below the source fault in the transition zone between the lower crust and lithospheric mantle (c.f. Chapter 4.2.4.2).

4.5.3 Future seismic hazard

The Wasatch fault zone is an active fault zone with the occurrence of large ($M \sim 7$) earthquakes in the region of high populated cities. The recurrence interval of the five most active central fault segments range between 1100 a and 1300 a (DuRoss et al. 2016). The last

earthquake on the central Wasatch fault ruptured 200 years ago on the Nephi segment. Since the last earthquake, stress of ~ 100 bar was accumulated on the Nephi segment, which could trigger a $M \sim 6.5$ earthquake. Our models illustrate that today the Wasatch fault region is not influenced by postseismic relaxation of the 200 a Nephi event due to the low mantle viscosity and the fast decrease of the relaxation influence (Fig. 4.8c, Chapter 4.5.2). The present-day stress changes on the faults in the Wasatch region are not caused by relaxation and fault interaction, but they are dominated by interseismic stress increase.

The Brigham City segment, which didn't rupture since 2400 a, accumulated ~ 780 bar of stress since the last earthquake. Of these, ~ 450 bar are caused by the interseismic stress increase and ~ 330 bar by the interaction of faults. Considering the accumulated stress, the recurrence interval and the time since the last earthquake, the Brigham City segment is the most endangered fault of the central Wasatch fault zone and could experience a $M \sim 7.1$ earthquake today. Our model results are in accordance with results for the Brigham City segment shown by Personius et al. (2012). The analysis of the recurrence interval and the stress situation on the SLCS reveals high seismic hazard for this region. Our model shows that the next earthquake on the SLCS could experience high magnitude of $M \geq 7.0$, hence the segment accumulated ~ 510 bar, since the last earthquake at 1300 a. Of these stress increase, ~ 260 bar are caused by the interaction of faults. Seismic hazard for the SLCS is also described by Chang and Smith (2002). The last earthquake on the Weber and Provo segment was triggered 600 years ago, so that less stress was accumulated until today. The analysis of seismic hazard of the faults zones west of the Wasatch fault zone is very uncertain due to insufficient data for modelling the earthquake history. Because of the high uncertainty of the historic earthquake timing on the Oquirrh fault zone, the calculation of the stress accumulation since the last earthquake is very uncertain. Calculated magnitudes of a hypothetical present-day earthquake are 7.0-7.3. A change in historic earthquake timing by several hundred years would strongly change the present-day stress situation.

Our models also show that the interaction of faults play an important role for the stress situation on fault zones and hence for the seismic hazard. The analysis of the stress changes caused by the interseismic stress increase and caused by the interaction of faults, respectively, shows that the interaction of faults contributes a significant content. For example, the SLCS accumulated ~ 650 bar of stress in the time interval between the 4100 a event and 2200 a event. Of these, ~ 370 bar are caused by the interseismic stress increase and ~ 280 bar by co- and postseismic stress changes of earthquakes on surrounded fault segments in the time interval between 4100 a and 2200 a. Due to stress transfer the seismic hazard can increase on

certain fault zones in the surrounding of the source fault. Therefore, a future earthquake on the investigated fault zones in the Wasatch region could trigger another earthquake on a nearby fault, lying in a co- and/or postseismic stress triggering zone, a short time after the first earthquake.

4.5.4 Comparison with previous studies of stress transfer and fault interaction on Wasatch fault

So far, only one study (Chang and Smith 2002) has evaluated the palaeo-Coulomb stress changes in the Wasatch region. These authors estimated the static stress changes for a hypothetical earthquake on the Provo segment and on the Brigham City segment, respectively. The generally results show static stress increase for along-strike segments of the Wasatch fault and static stress decrease for segments east and west of the faults. The $M_w = 6.8$ Brigham City event increases the stress on the adjacent WS by 1.2 bar and the $M_w = 7.1$ Provo event by 1.2 bar on the SLSC and by 4.0 bar on the NS (Chang and Smith 2002). The pattern of stress changes correlates with the spatial and temporal distribution of the palaeo-earthquakes of the Wasatch front area, including a higher recurrence interval of earthquakes in the Wasatch region than on the eastern and western faults (Chang and Smith 2002, McCalpin and Niskenko 1996). A disadvantage of this study is the neglect of the viscoelastic behaviour. Our model respects the earthquake history of the last 6400 a and the viscoelastic behaviour of the lower crust and lithospheric mantle. Our study confirmed the generally pattern of positive static stress changes in along-strike prolongation and negative static stress changes east and west of a source fault. In detail, our study reveals a small zone of stress increase in the hanging wall of the source fault. The magnitude of static stress changes is an order of magnitude higher than modelled by Chang and Smith (2002), which may relates to the definition of segment boundaries. Without calculating stress changes, but investigating palaeo-seismic data, DuRoss and Hylland (2015) assume that large earthquakes on the West Valley fault zone are linked to earthquakes on the Salt Lake City segment. Our models confirm a co- and postseismic stress transfer between the SLCS and the WVFZ. The 4100 a SLCS earthquake exhibits mostly high stress decrease (-161 bar), but also a small zone of static stress increase (18 bar) in the lower part of the Granger fault zone.

4.5.5 Comparison of geodetic displacement data and geological fault slip data

For creating our models, we analysed geodetic observations and geological data for the determination of the regional extension rate and for the improvement of our model. Geodetic

data are available for the last decades and deliver the recent surface velocity field of the Basin and Range Province, whereas geological palaeo-seismic data delivers information about the earthquake recurrence interval and fault slip for the last 10.000 a. For finding the best fitting model, we adapted the model to consider both, the measured geodetic data and the estimated fault slip per fault segment from literature.

The analysis and comparison of geodetic displacements and geological fault slip rates in the eastern Basin and Range Province (Wasatch fault region) are discussed by Friedrich et al. (2003). A perfectly-periodic earthquake model (Reid-type), where the fault ruptures are always in the same time interval with the same strain release, includes that far-field displacement agree with the fault slip (Reid 1910, Scholz 2002) (c.f. Chapter 1.1.2). Assuming the Wallace-type as strain release model for the earthquakes in the Wasatch fault region, strain accumulation (geodetic measurements) and strain release (fault slip measurements) strongly depends on the time (Wallace 1987). Slip rates strongly differ in times of earthquake clusters and times of long-term strain accumulation. Geodetic measurements and geological estimates of fault slip rates also differ for this interpretation (Friedrich et al. 2003). Chang and Smith (2002) estimated that the recurrence interval on the central Wasatch fault is higher using the geodetic-measured strain for the calculation than using the long-term fault-slip rate. They suggest that large earthquakes on the Wasatch fault may be clustered in the past 5600 a.

In our model we used a relative high value of the extension rate of 15 mm/a, which is in the upper range of the horizontal extension rate estimated by geodetic measurements (Chang et al. 2006). Lower extension rates deliver lower fault slip rates, which would be to less compared to the preferred observed fault slip rates (Tab. 4.2). A higher extension rate of 18 mm/a delivers fault slip rates, which are partly in a good agreement with the observed slip rates (Tab. 4.2), however, we didn't select this rate for our best fitting model because of the disagreement to geodetic measurements. For example, the vertical fault slip rates for the five active Wasatch fault segments are in a range of 1.3-2.0 mm/a (DuRoss et al. 2016). Our model (Mod B) with an extension rate of 12 mm/a leads to fault slip rates of 1.1-1.2 mm/a, whereas our model (Mod A) with an extension rate of 18 mm/a leads to fault slip rates of 1.6-1.8 mm/a. The vertical fault slip rate for the whole WVFZ is in a range of 0.5-0.6 mm/a (Keaton et al. 1993, Keaton and Currey 2013). An extension rate of 12 mm/a (Mod B) in our model leads to fault slip rates of 0.4 mm/a, in contrast to an extension rate of 18 mm/a (Mod A) leading to fault slip rates of 0.7 mm/a. Partly insufficient quality of data (e.g. small number of historic earthquakes, uncertainties in dating) on the Fremont-to-South-Oquirrh

fault zone, leads to variances in modelling and uncertainties in determination of the fault slip rate, resulting in high deviations between our models and literature, e.g. the slip rate on the Oquirrh fault zone in our models (0.8-1.2 mm/a) is generally higher than determined by Olig et al. (1994) (0.1-0.2 mm/a).

Using extension rates from geodetic measurements for modelling, two key factors have to be taken into account, if the spatial model extension differs from the position of the GPS-stations. First, the extension rate has to be adapted to the considered spatial extension. Second, the number of modelled fault zones has to be compared to the number of fault zones in the considered area in nature. The stations CEDA and HEBE span a 130 km wide area and are horizontally extended by 2.7 ± 0.4 mm/a (Friedrich et al. 2003), resulting in an extension rate of 9-12 mm/a for our 500 km wide model. The area between the GPS-stations include three major fault zones: the central WFZ, the Fremont-to-South-Oquirrh fault zone and the western Stansbury fault zone, as well as the border area of the WVFZ. The stations COON and HEBE span a 65 km wide area and are horizontally extended by 1.6 ± 0.4 mm/a (Chang et al. 2006), resulting in a extension rate of 9-15 mm/a for our 500 km wide model. The two GPS-stations span a region including the central WFZ and the border area of the WVFZ and excluding the Fremont-to-South-Oquirrh fault zone. Using the slip rate of the COON and HEBE stations, the modelled fault slip rate on the modelled fault zones tends to be smaller than in nature because our models include the Fremont-to-South-Oquirrh fault zone.

4.6 Conclusions

Using a three-dimensional finite-element model we analysed the stress changes for the last 6400 a and the future evolution of faults in the Wasatch fault region. This is the first study in which an entire series of earthquakes on a natural fault system is simulated in a finite-element model using realistic fault geometries and palaeo-seismological data. Our results show that despite model simplifications with respect to fault geometry and lithospheric structure, good agreement can be achieved with the palaeo-seismological record. This provides a base to use such finite-element models for calculating palaeo-Coulomb stress changes and for predicting present-day and future stress states and fault slip.

Altogether, we modelled 25 earthquakes on the segments of the central Wasatch fault zone, West Valley fault zone and Fremont-to-South-Oquirrh fault zone. Our best fitting model includes a regional extension rate of 15 mm/a, a 2000 a long first preseismic phase, a friction coefficient of $\mu = 0.4$ and a lower crust viscosity of $\eta_{lc} = 10^{21}$ Pa s. Our model results show that the background deformation causes a continuous Coulomb stress increase of ~ 0.19 bar/a

on the central WFZ, of $\sim 0.13\text{-}0.17$ bar/a on the FOFZ and of $\sim 0.12\text{-}0.14$ bar/a on the WVFZ. Stress increase due to background deformation is superposed by the positive and negative stress changes caused by sudden coseismic slip and postseismic viscoelastic relaxation. The coseismic stress drop on the source fault segments can reach several hundred bar and depends – as well as the coseismic stress changes on receiver faults – on the magnitude of the coseismic slip. The calculation of coseismic Coulomb stress changes shows that, independent of the location of the source fault, all modelled receiver faults are influenced by coseismic stress changes with highest stress changes in a range of several tenth of bar on receiver faults near the source fault. Coseismic stress changes on far distant receiver faults are in the range of less than 1 bar. In general, high positive stress changes arise in the along-strike direction of the source fault while high negative stress changes occur parallel to the source fault, however also a small zone of stress increase can arise in the nearby hanging wall of the source fault. The analysis of postseismic stress changes and the postseismic velocity field shows that the viscoelastic relaxation strongly influences the postseismic stress changes in the first years after the earthquake. The magnitude of postseismic stress change amounts several percent of the coseismic stress changes and decreases fast in the first ten years, so that no significant effect is observed in the hundredth year after the earthquake. The analysis of postseismic stress changes and velocities of the 200 a Nephi event, which is the most recent earthquake, shows that today no effect of the postseismic relaxation is present and the present-day stress accumulation is dominated by the interseismic stress increase. The calculation of Coulomb stress changes since the last earthquake per segment reveals that the highest stress increase on the central Wasatch fault zone is accumulated at the Brigham City segment (783 bar) and on the Salt Lake City segment (514 bar). Both fault zones have reached or exceeded the recurrence interval and pose high seismic hazard. A modelled hypothetical present-day earthquake would exhibit magnitudes of 7.0 and 7.1 for an SLCS event and BCS, respectively.

5 Discussion

This thesis about three-dimensional finite-element modelling of fault interaction on intra-continental normal and thrust faults shows the calculation of co- and postseismic Coulomb stress changes that are induced on surrounding receiver faults by an earthquake on a source fault. The calculation of stress changes is usually used for seismic hazard assessment to identify regions of increased stress, where the next earthquake is promoted. This thesis contains on the one hand the investigation of the influence of parameters (parameter study independent of a specific earthquake) and on the other hand the application to natural earthquakes and faults zones. In the following Chapter 5.1 the strengths and limitations of the models will be discussed. Then, the studies in this thesis will be compared and related to other natural earthquakes (Chapter 5.2, 5.3). After revealing the relevance of other stress transfer mechanisms (Chapter 5.4), the discussion closes with implications to earthquake triggering and forecast (Chapter 5.5). For detailed discussion of the co- and postseismic parameter studies and the Wasatch fault study see discussions in Chapter 2.4, 3.4 and 4.5.

5.1 Strengths and limitations of the models

The three-dimensional finite-element models created with Abaqus are well suited for the analysis of earthquake interaction. Compared to previous models, the models in this thesis have special advantages as shown in the introduction (Chapter 1), but they also include some simplifications. Next to the model discussion in Chapter 4.5.1 including some model simplifications and the problem of segment boundaries, in the following further model assumptions and simplifications as well as advantages of the models are discussed. A special advantage of the models is the variability. The models reveal the expansion of several rheologies and geometries. A simplification in the models is the finite-element mesh, which consists of linear elements because models with quadratic elements aborted.

The viscosity used in the models is described as linear Maxwell viscosity. Although this rheology is a simplification, the implementation of viscoelastic layers itself is an advantage compared to the commonly used homogeneous elastic half-space models based on Okada (1992) and is important for the investigation of postseismic stress changes and the effect of viscoelastic relaxation. In nature the viscosity depends on depth (temperature) and deformation. For power-law viscosity increasing stress leads to decreasing viscosity. Therefore, the coseismic stress increase in the lower crust and lithospheric mantle leads to lower effective viscosity resulting in higher postseismic strain rates that decrease faster; in

other words, the postseismic relaxation process would be faster than in models with linear viscosity behaviour (e.g. Ellis et al. 2006, Freed and Bürgmann 2004). Temperature is not considered in the models in this thesis. Implementation of the temperature gradient would imply that the viscosity decreases with temperature and, therefore, with depth (Sibson 1986). For further studies the models could be improved by considering temperature-dependent and power-law viscosity, both are generally potential features in Abaqus.

The friction coefficient, which controls slip on the faults, is constant in the models in this thesis. The models contain only two states of friction, when the fault slips and when the fault is locked. Dietrich (1994) has shown that the friction coefficient can change if the rate or state of the slip on the fault change (rate- and state- depending friction). Sudden increased load on a fault can reduce the fault friction which brings the fault closer to failure. The friction coefficient also alters long-term over several earthquake cycles, when the strength of the rock alters. Processes as brecciation cause reduction of fault strength (Sibson 1986), while cementation can increase fault strength (Bernabé et al. 1992). These long-term changes in friction are relevant, e.g. considering several earthquake cycles (Hampel and Hetzel 2012). In this thesis the fault behaviour is controlled by the Mohr-Coulomb criterion, although in nature the fault mechanisms are more complicated (Dietrich 1994, Scholz 1998). So far, the models created with Abaqus are limited by the usage of the Mohr-Coulomb criterion, a description of fault slip, which is also implied in the commonly used software Coulomb for the calculation of Coulomb stress changes (Toda et al. 2011).

Poroelastic properties are not defined in this thesis, but the effective coefficient of friction is applied, which considers the poroelastic stress changes, assuming that the pore pressure is proportional to the normal stress (Cocco and Rice 2002). An advantage of the models is the possibility of the integration of pore fluid pressure in future studies. Also the purely elastic behaviour of the upper crust is a simplification in the models because in reality the crust behaves elastoplastic or viscoelastoplastic outside fault zones and not simply purely elastic. On the one hand the consideration of plastic deformation in the crust would reduce the amount of coseismic slip on the source fault. On the other hand, the plastic deformation in the crust might weaken the rocks and locally modify the principal stresses (Chéry et al. 2004), which might bring other faults closer to failure. The models created with Abaqus are limited regarding to detailed modelling of the earth system, as they cannot realise all heterogeneities in the lithosphere.

The models created with Abaqus in this thesis are well suited for the calculation of Coulomb stress changes by using the Abaqus outputs of shear stress and normal stress. The

calculation of stress changes for natural earthquakes in other studies is associated with uncertainties derived from model assumptions and data uncertainties, particularly from uncertainties in the parameterisation of the source fault model (Hainzl et al. 2009, Woessner et al. 2012). Wang et al. (2014a) presented an error estimator for the Coulomb stress change and investigated the sensitivity of coseismic stress changes to some fault parameters in relation to the 2008 Wenchuan earthquake. The Coulomb stress studies in this thesis neither contain uncertainties analyses nor error propagation analysis. The parameter studies in this thesis are independent of a specific earthquake and data uncertainties to analyse the general effect of model parameter on Coulomb stress changes. Furthermore, the slip on the faults evolves freely from the regional stress field so that no uncertain source fault model has to be implied for the parameter studies. Also in the Wasatch fault study the fault slip is consistent with the regional stress field, which is important for the investigation of long-term stress changes over several earthquake cycles. Using source fault models and data inversion includes the implementation of geological heterogeneities resulting in Coulomb stress changes depending on local conditions, which is also important for the investigation of earthquakes. But also the understanding of the general pattern of Coulomb stress changes is essential. The idealised parameter models in this study are well suited for the understanding of the general pattern of stress changes and they can emphasise results which are not detectable in models using data inversion. In case of data inversion for natural examples the general pattern of stress changes is superposed by effects caused by geological conditions and heterogeneities. The parameter models in this thesis highlight the discrepancies to the models referring to a specific earthquake to analyse the effect of geological conditions on the Coulomb stress changes.

Another advantage of the models in this thesis is that – next to the Coulomb stress analysis – the models can be used also for further investigations, e.g. for the analysis of co- and postseismic surface deformation. The models created in Abaqus reveal the evaluation of surface deformation (e.g. displacements, velocities, strain field) for the coseismic phase (c.f. Figs. 2.2 a-d, 2.10, 4.7, 4.8) and postseismic phase (Figs. 5.1, 4.8). This modelled co- and postseismic surface deformation can be compared to natural surface deformation measured by geodetic data, e.g. GPS (Global Positioning System) and InSAR (Interferometric Synthetic Aperture Radar) data. For example, Hampel and Hetzel (2015) have shown a correlation between general finite-element models, which are similar to the models in this thesis, and the 2009 L'Aquila earthquake (Italy) as well as the 1999 Chi-Chi earthquake (Taiwan) for coseismic surface displacements and postseismic surface velocities (Fig. 5.2).

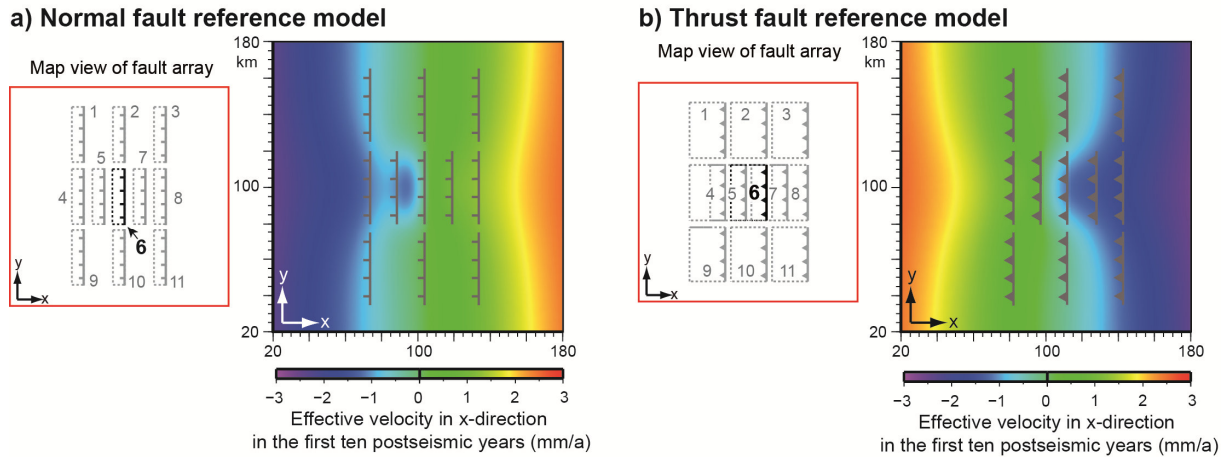


Figure 5.1: Modelled effective postseismic velocity in x-direction in the first ten years after the earthquake on fault 6 in the (a) normal and (b) thrust fault reference model shown in map view for the central part of the model surface (indicated by red box). The faults are labelled with numbers.

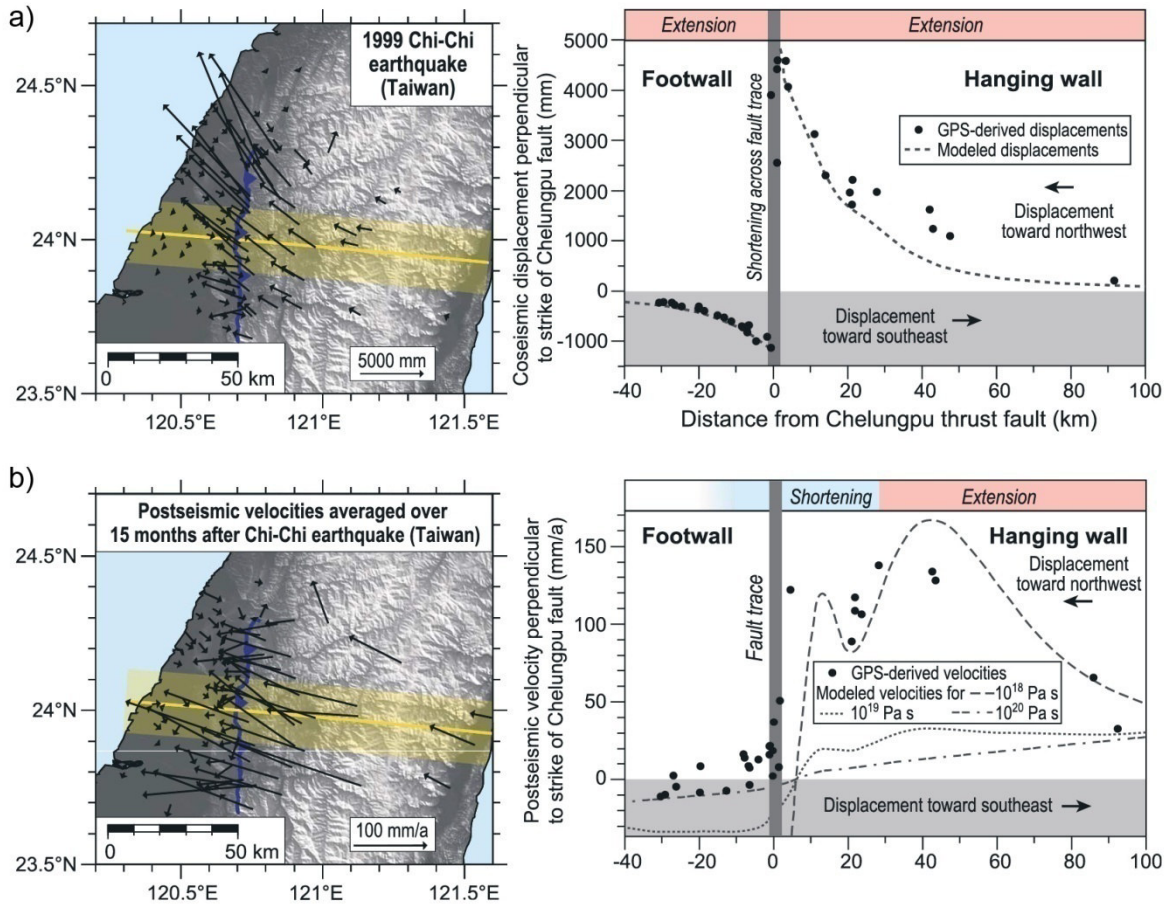


Figure 5.2: (a) Co- and (b) postseismic displacements and velocities for the 1999 Chi-Chi earthquake (Taiwan) from GPS records (left) and from finite-element thrust fault model on a profile perpendicular to strike of the Chelungpu fault (Hampel and Hetzel 2015). The results of the idealised model fit to the GPS records.

5.2 Comparison of the studies in this thesis

The models in this thesis were used to calculate co- and postseismic Coulomb stress changes for parameter studies independent of a specific fault or earthquake and for the Wasatch fault study applied to special fault zones and earthquake series. Each study builds upon the

previous one, where the knowledge of the influence of the parameter (Chapter 2 and 3) is involved for adapting the Wasatch fault model to nature and to calculate the co- and postseismic stress changes for palaeo-earthquakes and the future evolution.

The geometry of the fault zones in the normal fault parameter studies and in the Wasatch fault study is comparable. The parameter studies contain receiver faults, which are located parallel and in along-strike prolongation of the source fault and are therefore applicable to nature such as the Wasatch fault zone and the surrounding fault systems. The fault segments in the Wasatch fault study are positioned parallel in the hanging wall or footwall and displaced in along-strike direction. The general pattern of positive coseismic stress changes in along-strike prolongation and negative stress changes parallel to the source fault are observed in the normal fault models (e.g. Fig. 5.3).

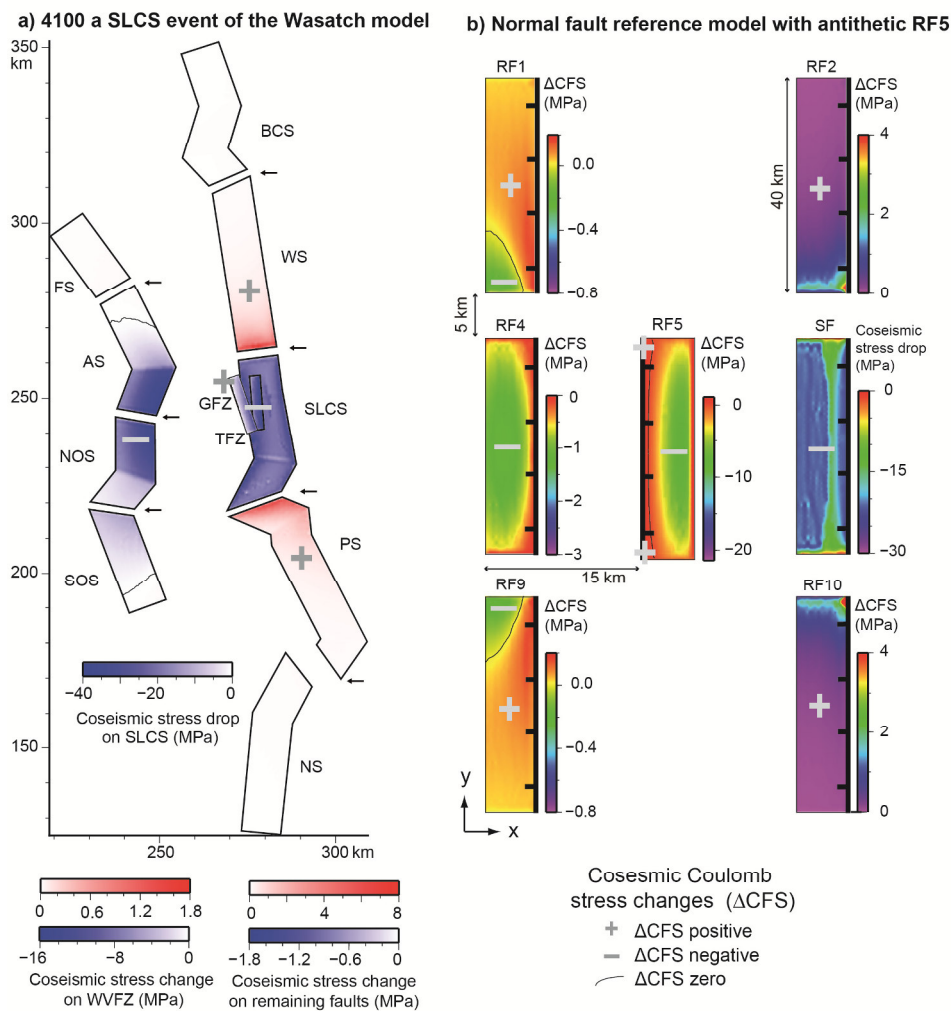


Figure 5.3: (a) Coseismic Coulomb stress changes for the 4100 a Salt Lake City segment (SLCS) earthquake on 50°-dipping synthetic receiver faults (Fremont segment (FS), Antelope segment (AS), North-Oquirrh segment (NOS), South-Oquirrh segment (SOS), Brigham City segment (BCS), Weber segment (WS), Nephi segment (NS)) and 60°-dipping antithetic receiver faults (Granger fault zone (GFZ), Taylorsville fault zone (TFZ)). (b) Coseismic Coulomb stress changes for the normal fault reference model with 60°-dipping synthetic receiver fault, except antithetic receiver fault 5.

In detail, a small zone of stress increase parallel and near the source fault is observed in the Wasatch fault model (on GFZ caused by the SLCS event, Fig. 5.3) and in the normal fault models of the parameter study. In this context it has to be noted that a small change in fault geometry (e.g. dip direction, dip angle) strongly influences whether a fault plane is located in a stress-triggering or stress-shadow zone as shown in Chapter 2.4.1. Differences between the parameter studies and the Wasatch fault study are, next to the fault geometry, caused by different rheologies and boundary conditions, e.g. by different viscosity structures (which effect is analysed in Chapter 3) or by different friction coefficients or different durations of the preseismic phase (which effect is analysed in Chapter 2). The application to the Wasatch fault model has the advantage that the influence of previous earthquakes is considered which improves the analysis of Coulomb stress changes. The Wasatch fault model shows that for future investigations of earthquake interaction the analysis of only one recent earthquake can be exceeded to the analysis of several earthquake cycles for the complete fault system.

5.3 Comparison with other natural earthquakes

The results of this thesis show that the models of the parameter studies can be adapted to natural earthquakes. Detailed comparisons between the parameter models and natural earthquakes are shown in Chapters 2.4.3 and 3.4.3. For example, the triggering of the 2013 Lushan earthquake (China) by the 2008 Wenchuan earthquake (China) correlates with the positive static stress change in along-strike direction of the thrust source fault in the parameter study of this thesis (Parsons and Segou 2014, Wang et al. 2014b). Also the coseismic stress-triggering zones in the normal fault reference model correlate with the 1997 Umbria-Marche earthquake sequence (Italy) (including eight $M > 5$ events), which occurred in along-strike prolongation between the faults that ruptured by the 1984 Gubbio earthquake and the 1979 Norcia earthquake (Cocco et al. 2000). The recent 2016 central Italy $M = 6.2$ earthquake on the NW-SE oriented normal fault in the central Apennines (Fig. 5.4) occurred ~ 10 km southeast of the 1979 Norcia earthquake (Haessler et al. 1988), ~ 50 km southeast of the 1997 Umbria-Marche sequence (Cocco et al. 2000, Fig. 5.4b) and ~ 45 km northwest of the 2009 $M_w = 6.3$ L'Aquila earthquake (Serpelloni et al. 2012, Fig. 5.4c). Preliminary results show that the recent central Italy earthquake is located in a gap between the aftershock sequences of the 2009 L'Aquila event and 1997 Umbria-Marche event (USGS homepage <http://earthquake.usgs.gov/>). The normal fault model of the parameter study of this thesis suggests that the location of the recent central Italy earthquake corresponds to the location of

the coseismic stress-triggering zones of the 2009 L'Aquila event and 1997 Umbria-Marche event (Fig. 5.4e).

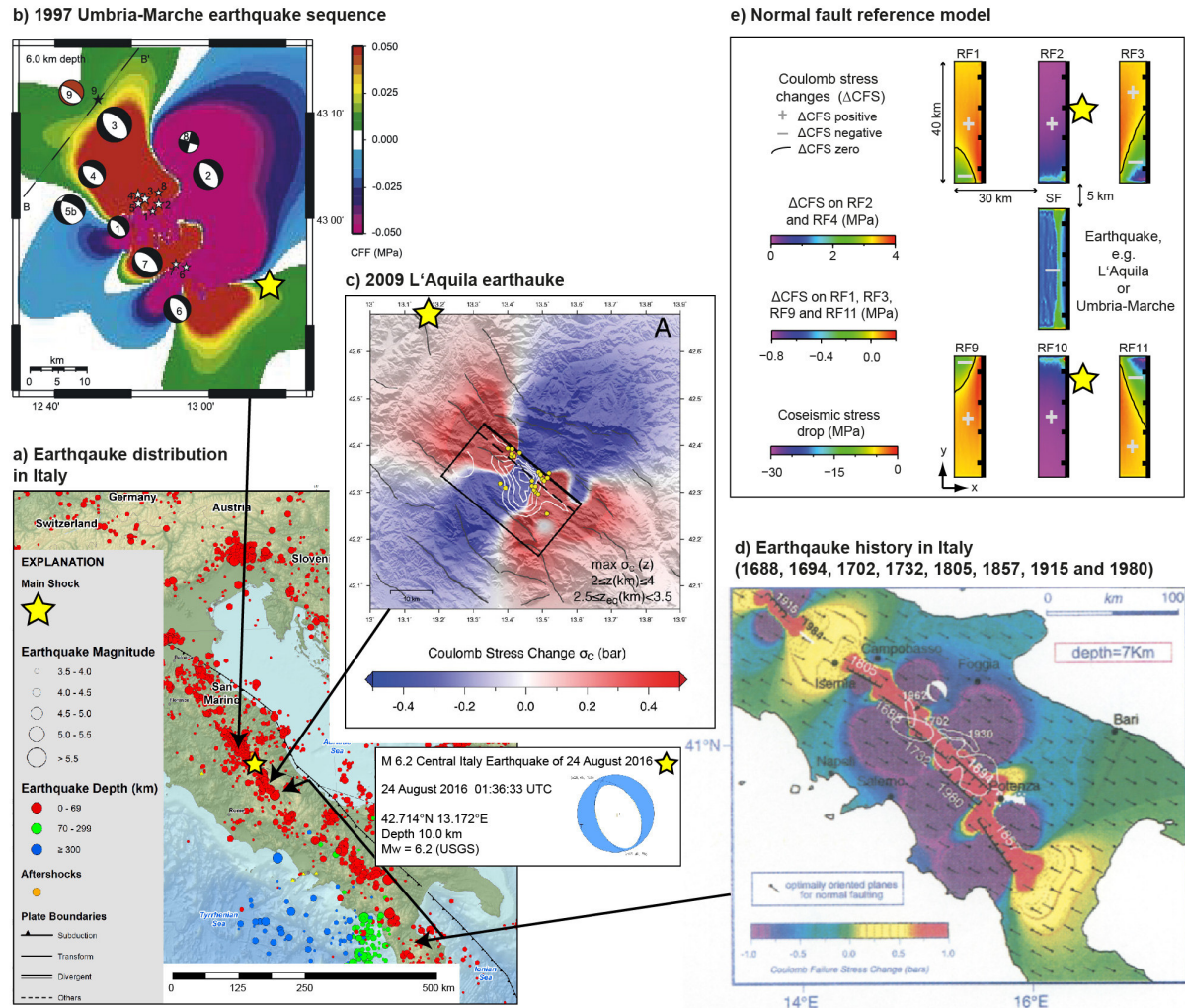


Figure 5.4: General overview of the 2016 central Italy earthquake (yellow star) relating to location and stress changes induced by previous earthquakes. (a) Earthquake distribution in Italy during last century (modified from USGS homepage <http://earthquake.usgs.gov/>). (b) Coseismic stress changes of the 1997 Umbria-Marche earthquake sequence (modified from Nostro et al. 2005). (c) Coseismic stress changes of the 2009 L'Aquila earthquake (modified from Serpelloni et al. 2011). (d) Earthquake history between 1688 and 1980 (modified from Nostro et al. 1997). (e) Coseismic stress changes from the normal fault reference model, which earthquake on the source fault can be compared to the Umbria-Marche earthquake sequence and the L'Aquila earthquake. The 2016 central Italy earthquake is located in stress triggering zones of the Umbria-Marche earthquake sequence and the 2009 L'Aquila earthquake, which is supported by the model results in this thesis.

Also the postseismic parameter study can be used for the application to the recent central Italy earthquake. The viscosity structure of model NP3 and NP4 is comparable with the local conditions including an elastic upper crust, underlain by a transition zone with a viscosity of 10^{18} Pa s (Riva et al. 2007). Therefore, the results of this thesis suggest a strong effect of viscoelastic relaxation, fault interaction and stress changes in the first years after the earthquake related to model NP3 and NP4. Because of the existence of palaeo-seismic records and fault geometries for historic and recent earthquakes in central Italy (c.f. Fig. 5.4d, Nostro et al. 1997) and because of the correlation between the model results and natural events, the

models in this thesis are well suited for the investigation of stress changes including the earthquake history as shown for the Wasatch fault model in this thesis (Chapter 4).

5.4 Consideration of other stress transfer mechanisms

While investigating earthquake triggering it is always important to consider that stress interaction can be caused by a superposition of mechanisms and the triggering always depends on the status of the fault in its earthquake cycle. Therefore, stress transfer can bring a fault closer to failure and reduces the time to the next earthquake without triggering an earthquake at the moment. Some of these stress transfer mechanisms are shown in Chapter 1. Each mechanism can lead to stress increase and or decrease over individual time intervals. This thesis includes the effect of static stress changes as well as the effect of postseismic stress changes caused by viscoelastic relaxation superpositioned by the interseismic stress increase to analyse under which conditions these mechanisms bring a fault closer to failure (due to positive stress transfer) and under which conditions the next earthquake is delayed (due to negative stress transfer) (parameter studies). To estimate the stress changes on a natural fault system as much as possible stress transfer mechanisms should be considered. The Wasatch fault model in this study could be improved if other mechanisms of stress transfer (e.g. pore pressure changes) will be implemented in the analysis.

5.5 Implications for earthquake triggering and forecast

So far, several earthquake cycle models are developed to describe and understand the earthquake recurrence on fault zones. Well established models as the time-predictable and slip-predictable model as well as the Wallace-type behaviour are shown in Chapter 1.1.2 (Fig. 1.2, Friedrich et al. 2003). In nature, however, the earthquake occurrence generally differs from these models due to individual local conditions and heterogeneities in the lithosphere. Therefore, a time-prediction for the next earthquake is so far impossible (Geller et al. 1997, Stein 2003). Apart from the stress increase caused by the regional stress field, stress changes on fault zones also arise from special local conditions. For example, earthquakes can be triggered by changes in water masses or ice sheets (Karow and Hampel 2010), anthropogenic activities (e.g. fluid injections: Shirzaei et al. 2016) or mechanisms shown in Chapter 1.1.4. An important mechanism of earthquake triggering is the interaction of faults by stress transfer. In contrast to the assumption that earthquakes are independent, studies have shown that seismicity is highly interactive and that changes in seismicity rate correlate with stress changes caused by earthquakes (e.g. Stein 1999, Stein 2003). Although the forecast of

time, location and magnitude of future earthquakes is still impossible, the consideration of stress transfer and interaction of faults reveals the identification of fault zones with increased and decreased seismic hazard and the generation of a seismic hazard map after an earthquake (King et al. 1994, Stein 1999, Stein 2003). Therefore, the calculation of stress changes, considering the alternation of seismic hazard after an earthquake for surrounding fault zones, introduces a new generation of earthquake forecast (Stein 2003).

The theory of co- and postseismic stress transfer can be connected to the occurrence of earthquake clusters, where long-term strain accumulations are alternated with short-term earthquake series (Wallace 1987). These earthquake clusters can be associated with interacting fault zones and increased occurrence of stress transfer caused by previous earthquakes leading to the triggering of further earthquakes during the short-term earthquake series. In addition, the commonly used stress change analysis for a specific earthquake could be improved considering the earthquake history of a whole fault system as shown for the Wasatch fault model in Chapter 4. Such models, which are constrained by the palaeoseismological record and consider a realistic fault geometry, co-and postseismic stress transfer mechanisms, interseismic stress increase, offer the possibility to extend the model run into future and hence may provide a tool for estimating timing, slip and magnitude of possible future earthquakes.

6 Conclusions and Outlook

In the context of seismic hazard assessment, this thesis includes the investigation of fault interaction by calculating co- and postseismic Coulomb stress changes using three-dimensional finite-element models of intra-continental dip-slip faults, including slip developing freely from the applied tectonic background (i.e. shortening or extension) and considering gravity and viscoelastic behaviour. The parameter studies deliver information about the general stress pattern independent of a specific earthquake and without superposition of geological conditions and heterogeneities and show how parameters like fault geometry, rheology and friction coefficient change the co- and postseismic stress pattern. The application of the models to the active normal Wasatch fault system in the eastern Basin and Range Province (Utah) is a pilot study showing that an entire series of earthquakes on a natural fault system can be modelled using realistic fault geometries and palaeo-seismological data to analyse co- and postseismic Coulomb stress changes of palaeo-earthquakes and the future evolution. The models used in this thesis provide the fundament for future work. An advantage of the models is that they can be steadily extended and improved or changed and adapted to natural examples. Further steps may include the improvement of the general model setup, for example by the implementation of power-law and temperature-dependent viscosity or the implementation of pore pressure changes. The models could be investigated regarding the effect of these implementations or further parameters. Another possible research objective is the investigation of the Wasatch fault study in terms of the relevance and influence of segment boundaries. The modelling of a number of earthquake cycles for the assessment of future seismic risks and earthquake triggering as shown in the Wasatch fault model promises new approaches and in the future this method should be applied to other earthquake series on diverse fault systems. Such models require information about fault geometry and palaeo-seismic data. For example, the earthquake series in central Italy, which were documented for centuries, including the most recent 2016 central Italy earthquake, could be investigated in a similar way. Because the models in this thesis can be evaluated regarding to several aspects (e.g. stress, strain, displacement, velocities), the models reveal the comparison with several natural data sets as geodetic data (GNSS, InSAR), seismological data and palaeo-seismological data.

7 Acknowledgements

First of all, I would like to sincerely thank my supervisor Prof. Dr. Andrea Hampel for all her support and encouragement throughout the last years. Thank you for offering me the opportunity to undertake this exciting and challenging project. I am very pleased for your continued interest, your constant reinforcement and for sharing your extensive knowledge. The multitude of inspirational discussions and the constructive criticism in all phases of my work have been a great pleasure.

Secondly, I would like to thank Dr. Georgios Maniatis not only for providing technical support but also for many constructive topical discussions. I would like to extend my thanks to all my colleagues for inspiring conversations at our Institute and on several conferences. In particular, I thank Ryan Gold for inspirational communication and helpful suggestions for the successful implementation of the Wasatch fault study.

Furthermore, I would like to acknowledge Prof. Dr. Ulrich Heimhofer for taking up the position as co-examiner as well as Prof. Dr. Jürgen Böttcher for his support as a chairman of the examination committee.

Special thanks go also to my family and friends for encouraging me and the continuous moral support.

8 References

- Allmann, B.P., Shearer, P.M. 2009. Global variations of stress drop for moderate to large earthquakes. *J. Geophys. Res.* 114, B01310. doi:10.1029/2008JB005821
- Asano, Y., Saito, T., Ito, Y., Shiomi, K., Hirose, H., Matsumoto, T., Aoi, S., Hori, S., Sekiguchi, S. 2011. Spatial distribution and focal mechanisms of aftershocks of the 2011 off the Pacific coast of Tohoku Earthquake. *Earth Planets Space* 63, 669-673.
- Bagge, M., Hampel, A. 2015. Three-dimensional finite-element modelling of coseismic Coulomb stress changes on intra-continental dip-slip faults, *Tectonophysics* 684, 52-62. doi:10.1016/j.tecto.2015.10.006
- Bagge, M., Hampel, A. Postseismic Coulomb stress changes on intra-continental dip-slip faults due to viscoelastic relaxation in the lower crust and lithospheric mantle: insights from 3D finite-element modelling, submitted to *International Journal of Earth Sciences*.
- Belardinelli, M.E., Cocco, M., Coutant, O., Cotton, F. 1999. Redistribution of dynamic stress during coseismic ruptures: Evidence for fault interaction and earthquake triggering. *J. Geophys. Res.* 104, 14925-14945
- Bernabé, Y., Fryer, D.T., Hayes, J.A. 1992. The effect of cement on the strength of granular rocks. *Geophys. Res. Lett.* 19, 1511-1514. doi:10.1029/92GL01288
- Bhloscaidh, M.N., McCloskey, J., Bean, C.J. 2014. Response of the San Jacinto Fault Zone to static stress changes from the 1992 Landers earthquake. *J. Geophys. Res.* 119, 8914-8935.
- Bills, B.G., Currey, D.R., Marshall, G.A. 1994. Viscosity estimates for the crust and upper mantle from patterns of lacustrine shoreline deformation in the Eastern Great Basin. *J. Geophys. Res.* 99, 22059-22086. doi:10.1029/94JB01192
- Brace, W.F., Kohlstedt, D.L. 1980. Limits on lithospheric stress imposed by laboratory experiments. *J. Geophys. Res.* 85, 6248-6252.
- Burov, E.B., Watts, A.B. 2006. The long-term strength of the continental lithosphere: "jelly sandwich" or "crème brûlée"? *GSA Today* 16, 4-10.
- Byerlee, J. 1978. Friction of rocks. *Pure and applied geophysics* 116, 615-626. doi:10.1007/BF00876528
- Cattania, C., Hainzl, S., Wang, L., Enescu, B., Roth, F. 2015. Aftershock triggering by postseismic stresses: A study based on Coulomb rate-and-state models. *J. Geophys. Res.* 120, 2388-2407.
- Chang, W.L., Smith, R.B. 2002. Integrated seismic-hazard analysis of the Wasatch Front, Utah. *Bull. Seismol. Soc. Am.* 92, 1904-1922. doi:10.1785/0120010181

- Chang, W.L., Smith, R.B., Meertens, C.M., Harris, R.A. 2006. Contemporary deformation of the Wasatch Fault, Utah, from GPS measurements with implications for interseismic fault behavior and earthquake hazard: Observations and kinematic analysis. *J. Geophys. Res.* 111, B11405. doi:10.1029/2006JB004326
- Cheloni, D., D'Agostino, N., D'Anastasio, E., Avallone, A., Mantenuto, S., Giuliani, R., Mattone, M., Calcaterra, S., Gambino, P., Dominici, D., Radicioni, F., Fastellini, G. 2010. Coseismic and initial post-seismic slip of the 2009 Mw 6.3 L'Aquila earthquake, Italy, from GPS measurements. *Geophys. J. Int.* 181, 1539-1546.
- Chen, W.P., Molnar, P. 1983. Focal depths of intracontinental and intraplate earthquakes and their implications for the thermal and mechanical properties of the lithosphere. *J. Geophys. Res.* 88, 4183-4214.
- Chen, Z., Lin, B., Bai, W., Cheng, X., Wang, Y. 2011. A study on the influence of the 2008 Wenchuan earthquake on the stability of the Qinghai–Tibet Plateau tectonic block system. *Tectonophysics* 510, 94-103.
- Chéry, J., Carretier, S., Ritz, J.-F. 2001. Postseismic stress transfer explains time clustering of large earthquakes in Mongolia. *Earth Planet. Sci. Lett.* 194, 277-286.
- Chéry, J., Zoback, M.D., Hickman, S. 2004. A mechanical model of the San Andreas fault and SAFOD Pilot Hole stress measurements. *Geophys. Res. Lett.* 31, L15S13. doi:10.1029/2004GL019521
- Cianetti, S., Giunchi, C., Cocco, M. 2005. Three-dimensional finite element modeling of stress interaction: An application to Landers and Hector Mine fault systems. *J. Geophys. Res.* 110, B05S17.
- Coble, C.G., French, M.E., Chester, F.M., Chester, J.S., Kitajima, H. 2014. *In situ* frictional properties of San Andreas Fault gouge at SAFOD. *Geophys. J. Int.* 199, 956-967.
- Cocco, M., Nostro, C., Ekström, G. 2000. Static stress changes and fault interaction during the 1997 Umbria-Marche earthquake sequence. *J. Seismology* 4, 501-516.
- Cocco, M., Rice, J.R. 2002. Pore pressure and poroelasticity effects in Coulomb stress analysis of earthquake interactions. *J. Geophys. Res.* 107, 2030. doi:10.1029/2000JB000138
- Collettini, C., Niemeijer, A., Viti, C., Marone, C. 2009. Fault zone fabric and fault weakness. *Nature* 462, 907-910.
- Dempsey, D.E., Archer, R.A., Ellis, S.M., Rowland, J.V. 2013. Hydrological effects of dip-slip fault rupture on a hydrothermal plume. *J. Geophys. Res.* 118, 195–211. doi:10.1029/2012JB009395

- Diao, F., Xiong, X., Wang, R., Zheng, Y., Walter, T.R., Weng, H., Li, J. 2014. Overlapping post-seismic deformation processes: afterslip and viscoelastic relaxation following the 2011 M_w 9.0 Tohoku (Japan) earthquake. *Geophys. J. Int.* 196, 218-229.
- Dieterich, J. 1994. A constitutive law for rate of earthquake production and its application to earthquake clustering. *J. Geophys. Res.* 99, 2601-2618. doi:10.1029/93JB02581
- DuRoss, C.B., Personius, S.F., Crone, A.J., Olig, S.S., Lund, W.R. 2011. Integration of palaeoseismic data from multiple sites to develop an objective earthquake chronology: Application to the Weber segment of the Wasatch fault zone, Utah. *Bull. Seismol. Soc. Am.* 101, 2765-2781. doi:10.1785/0120110102
- DuRoss, C.B., Hylland, M.D. 2015. Synchronous Ruptures along a Major Graben-Forming Fault System: Wasatch and West Valley Fault Zones, Utah. *Bull. Seismol. Soc. Am.* 105. doi:10.1785/0120140064
- DuRoss, C.B., Personius, S.F., Crone, A.J., Olig, S.S., Hylland, M.D., Lund, W.R., Schwartz, D.P. 2016. Fault Segmentation: New Concepts from the Wasatch Fault Zone, Utah, USA. *J. Geophys. Res.* 121, 1131–1157. doi:10.1029/2015JB012519
- Ellis, S., Stöckhert, B. 2004. Elevated stresses and creep rates beneath the brittle-ductile transition caused by seismic faulting in the upper crust. *J. Geophys. Res.* 109, B05407. doi:10.1029/2003JB002744
- Ellis, S., Beavan, J., Eberhart-Phillips, D., Stöckhert, B. 2006. Simplified models of the Alpine Fault seismic cycle: stress transfer in the mid-crust. *Geophys. J. Int.* 166, 386-402.
- England, P., Jackson, J. 2011. Uncharted seismic risk. *Nature Geoscience* 4, 348-349.
- Evans, J.P., Langrock, H. 1994. Structural analysis of the Brigham City-Weber segment boundary zone, Wasatch normal fault, Utah: Implications for fault growth and structure. *pure and applied geophysics* 142, 663-685. doi:10.1007/BF00876059
- Fagan, M.J. 1992. *Finite Element Analysis: Theory and Practice*, Harlow.
- Freed, A.M. 2005. Earthquake triggering by static, dynamic, and postseismic stress transfer. *Annu. Rev. Earth Planet. Sci.* 33, 335-367. doi:10.1146/annurev.earth.33.092203.122505
- Freed, A.M., Lin, J. 1998. Time-dependent changes in failure stress following thrust earthquakes. *J. Geophys. Res.* 103, 24393-24409.
- Freed, A.M., Lin, J. 2001. Delayed triggering of the 1999 Hector Mine earthquake by viscoelastic stress transfer. *Nature* 411, 180-183.
- Freed, A.M., Bürgmann, R. 2004. Evidence of power-law flow in the Mojave desert mantle. *Nature* 430, 548-551. doi:10.1038/nature02784
- Friedrich, A.M., Wernicke, B.P., Niemi, N.A., Bennett, R.A., Davis, J.L. 2003. Comparison

- of geodetic and geologic data from the Wasatch region, Utah, and implications for the spectral character of Earth deformation at periods of 10 to 10 million years. *J. Geophys. Res.* 108. 2199. doi:10.1029/2001JB000682
- Fu, B., Ninomiya, Y., Lei, X., Toda, S., Awata, Y. 2004. Mapping active fault associated with the 2003 Mw 6.6 Bam (SE Iran) earthquake with ASTER 3D images. *Remote Sensing Environ.* 92, 153-157.
- Geller, R.J., Jackson, D.D., Kagan, Y.Y., Mulargia, F. 1997. Earthquakes cannot be predicted. *Science* 275, 1616-1616. doi:10.1126/science.275.5306.1616
- Gilbert, G.K. 1928. Studies of Basin and Range structure, U.S. Geol. Surv. Prof. Pap. 153.
- Gomberg, J., Reasenber, P.A., Bodin, P., Harris, R.A. 2001. Earthquake triggering by seismic waves following the Landers and Hector Mine earthquakes. *Nature* 411, 462-466. doi:10.1038/35078053
- Gourmelen, N., Amelung, F. 2005. Postseismic mantle relaxation in the central Nevada seismic belt. *Science* 310, 1473-1476. doi:10.1126/science.1119798
- Haessler, H., Gaulon, R., Rivera, L., Console, R., Frogneux, M., Gasparini, G., Martel, L., Patau, G., Siciliano, M., Cisternas, A. 1988. The Perugia (Italy) earthquake of 29, April 1984: a microearthquake survey. *Bull. Seismol. Soc. Am.* 78, 1948-1964.
- Hainzl, S., Enescu, B., Cocco, M., Woessner, J., Catalli, F., Wang, R., Roth F. 2009. Aftershock modeling based on uncertain stress calculations, *J. Geophys. Res.* 114, B05309. doi:10.1029/2008JB006011
- Haller, K.M., Machette, M.N., Dart, R.L., Rhea, B.S. 2004. U.S. Quaternary fault and fold database released. *Eos, Trans. Am. Geophys. Union* 85, 22, 218.
- Hampel, A., Hetzel, R., Maniatis, G., Karow, T. 2009 Three-dimensional numerical modeling of slip rate variations on normal and thrust fault arrays during ice cap growth and melting. *J. Geophys. Res.* 114, B08406. doi:10.1029/2008JB006113
- Hampel, A., Hetzel, R. 2012. Temporal variation in fault friction and its effects on the slip evolution of a thrust fault over several earthquake cycles. *Terra Nova* 24, 357-362.
- Hampel, A., Li, T., Maniatis, G. 2013. Contrasting strike-slip motions on thrust and normal faults: Implications for space-geodetic monitoring of surface deformation. *Geology* 41, 299-302. doi:10.1130/G33927.1
- Hampel, A., Hetzel, R. 2015. Horizontal surface velocity and strain patterns near thrust and normal faults during the earthquake cycle: The importance of viscoelastic relaxation in the lower crust and implications for interpreting geodetic data. *Tectonics* 34, 731-752. doi:10.1002/2014TC003605

- Hanks, T.C. 1977. Earthquake Stress Drops, Ambient Tectonic Stresses and Stresses That Drive Plate Motions. *Pure Appl. Geophys.* 115, 441-458.
- Harris, R.A. 1998. Introduction to special section: Stress triggers, stress shadows, and implications for seismic hazard. *J. Geophys. Res.* 103, 24347-24358. doi:10.1029/98JB01576
- Hetzl, R., Tao, M., Niedermann, S., Strecker, M.R., Ivy-Ochs, S., Kubik, P.W., Gao, B. 2004. Implications of the fault scaling law for the growth of topography: mountain ranges in the broken foreland of north-east Tibet. *Terra Nova* 16, 157-162.
- Hetzl, R., Hampel, A. 2005. Slip rate variations on normal faults during glacial–interglacial changes in surface loads. *Nature* 435, 81-84. doi:10.1038/nature03562
- Hsu, Y.-J., Simons, M., Avouac, J.-P., Galetzka, J., Sieh, K., Chlieh, M., Natawidjaja, D., Prawirodirdjo, L., Bock, Y. 2006. Frictional afterslip following the 2005 Nias-Simeulue earthquake, Sumatra. *Science* 312, 1921-1926.
- Hurd, O., Zoback, M.D. 2012. Intraplate earthquakes, regional stress and fault mechanics in the Central and Eastern US and Southeastern Canada. *Tectonophysics* 581, 182-192.
- Jia, D., Li, Y., Lin, A., Wang, M., Chen, W., Wu, X., Ren, Z., Zhao, Y., Luo, L. 2010. Structural model of 2008 M_w 7.9 Wenchuan earthquake in the rejuvenated Longmen Shan thrust belt, China. *Tectonophysics* 491, 174-184.
- Jia, K., Zhou, S., Zhuang, J., Jiang, C. 2014. Possibility of the Independence between the 2013 Lushan Earthquake and the 2008 Wenchuan Earthquake on Longmen Shan Fault, Sichuan, China. *Seismol. Res. Lett.* 85, 60-67.
- Kanamori, H., Anderson, D.L. 1975. Theoretical basis of some empirical relations in seismology. *Bull. Seismol. Soc. Am.* 65, 1073-1095.
- Karow, T., Hampel, A. 2010. Slip rate variations on faults in the Basin-and-Range Province caused by regression of Late Pleistocene Lake Bonneville and Lake Lahontan. *Int. J. Earth Sciences* 99, 1941-1953. doi:10.1007/s00531-009-0496-3
- Kaufmann, G., Amelung, F. 2000. Reservoir-induced deformation and continental rheology in vicinity of Lake Mead, Nevada. *J. Geophys. Res.* 105, 16341-16358. doi:10.1029/2000JB900079
- Keaton, J.R., Currey, D.R. 1993. Earthquake Hazard Evaluation of the West Valley Fault Zone in the Salt Lake City Urban Area, Utah. *Utah Geol. Surv. Contract Rept.* 93-7.
- Keaton, J.R., Currey, D.R., Olig, S.J. 1993. Paleoseismicity and Earthquake Hazards Evaluation of the West Valley Fault Zone, Salt Lake City Urban Area, Utah. *Utah Geol. Surv. Contract Rept.* 93-8.

- King, G.C., Stein, R.S., Lin, J. 1994. Static Stress Changes and the Triggering of Earthquakes. *Bull. Seismol. Soc. Am.* 84, 935-953.
- Klemperer, S.L. 2006. Crustal flow in Tibet: Geophysical evidence for the physical state of Tibetan lithosphere, and inferred patterns of active flow. *Geol. Soc. London Spec. Publ.* 268, 39-70. 10.1144/GSL.SP.2006.268.01.03
- Lin, A., Ren, Z.K., Jia, D., Wu, X.J. 2009. Co-seismic thrusting rupture and slip distribution produced by the 2008 M_w 7.9 Wenchuan earthquake, China. *Tectonophysics* 471, 203-215.
- Lin, J., Stein, R.S. 2004. Stress interaction in thrust and subduction earthquakes and stress interaction between the southern San Andreas and nearby thrust and strike-slip faults. *J. Geophys. Res.* 109, B02303. doi:10.1029/2003JB002607
- Lin, J., Stein, R.S., Meghraoui, M., Toda, S., Ayadi, A., Dorbath, C., Belabbes, S. 2011. Stress transfer among en echelon and opposing thrusts and tear faults: Triggering caused by the 2003 M_w = 6.9 Zemmouri, Algeria, earthquake. *J. Geophys. Res.* 116, B03305.
- Lund, W.R. 2005. Consensus preferred recurrence interval and vertical slip rate estimates: Review of Utah paleoseismic-trenching data by the Utah Quaternary Fault Parameters Working Group: *Utah Geol. Surv. Bull.* 134.
- Luo, G., Liu, M. 2010. Stress evolution and fault interactions before and after the 2008 Great Wenchuan earthquake. *Tectonophysics* 491, 127-140.
- Machette, M.N., Personius, S.F., Nelson, A.R., Schwartz, D.P., Lund, W.R. 1991. The Wasatch fault zone, Utah—segmentation and history of Holocene earthquakes. *J. Struct. Geol.* 13, 137-149. doi:10.1016/0191-8141(91)90062-N
- Mallman, E.P., Zoback, M.D. 2007. Assessing elastic Coulomb stress transfer models using seismicity rates in southern California and southwestern Japan. *J. Geophys. Res.* 112, B03304. doi:10.1029/2005JB004076
- Malservisi, R., Dixon, T.H., La Femina, P.C., Furlong, K.P. 2003. Holocene slip rate of the Wasatch fault zone, Utah, from geodetic data: Earthquake cycle effects. *Geophys. Res. Lett.* 30. doi:10.1029/2003GL017408
- Maniatis, G., Hampel, A. 2008. Along-strike variations of the slip direction on normal faults: Insights from three-dimensional finite-element models. *J. Struct. Geology* 30, 21-28. doi:10.1016/j.jsg.2007.10.002
- Masterlark, T., Wang, H.F. 2002. Transient Stress-Coupling Between the 1992 Landers and 1999 Hector Mine, California, Earthquakes. *Bull. Seismol. Soc. Am.* 92, 1470-1486.
- McCalpin, J.P., Nishenko, S.P. 1996. Holocene paleoseismicity, temporal clustering, and probabilities of future large ($M > 7$) earthquakes on the Wasatch fault zone, Utah. *J.*

- Geophys. Res. 101, 6233-6253. doi:10.1029/95JB02851
- Meyer, B., Tapponnier, P., Bourjot, L., Métivier, F., Gaudemer, Y., Peltzer, G., Guo, S., Chen, Z. 1998. Crustal thickening in Gansu-Qinghai, lithospheric mantle subduction, and oblique, strike-slip controlled growth of the Tibetan Plateau. *Geophys. J. Int.* 135, 1-47.
- Miller, S.A., Collettini, C., Chiaraluce, L., Cocco, M., Barchi, M., Kaus, B.J. 2004. Aftershocks driven by a high-pressure CO₂ source at depth. *Nature* 427, 724-727.
- Nalbant, S.S., McCloskey, J. 2011. Stress evolution before and after the 2008 Wenchuan, China earthquake. *Earth Planet. Sci. Lett.* 307, 222-232.
- Niemeijer, A.R., Collettini, C. 2014. Frictional properties of a low-angle normal fault under in situ conditions: Thermally-activated velocity weakening. *Pure Appl. Geophys.* 171, 2641-2664.
- Niemi, N.A., Wernicke, B.P., Friedrich, A.M., Simons, M., Bennett, R.A., Davis, J.L. 2004. BARGEN continuous GPS data across the eastern Basin and Range province, and implications for fault system dynamics. *Geophys. J. Int.* 159, 842-862. doi:10.1111/j.1365-246X.2004.02454.x
- Nishimura, T., Thatcher, W. 2003. Rheology of the lithosphere inferred from postseismic uplift following the 1959 Hebgen Lake earthquake. *J. Geophys. Res.* 108. doi:10.1029/2002JB002191
- Nostro, C., Cocco, M., Belardinelli, M.E. 1997. Static Stress Changes in Extensional Regimes: An Application to Southern Apennines (Italy). *Bull. Seismol. Soc. Am.* 87, 234-248.
- Nostro, C., Piersanti, A., Cocco, M. 2001. Normal fault interaction caused by coseismic and postseismic stress changes. *J. Geophys. Res.* 106, 19391-19410.
- Nostro, C., Chiaraluce, L., Cocco, M., Baumont, D., Scotti, O. 2005. Coulomb stress changes caused by repeated normal faulting earthquakes during the 1997 Umbria-Marche (central Italy) seismic sequence. *J. Geophys. Res.* 110, B05S20. doi:10.1029/2004JB003386
- Okada, Y. 1992. Internal deformation due to shear and tensile faults in a half-space. *Bull. Seismol. Soc. Am.* 82, 1018-1040.
- Olig, S.S., Lund, W.R., Black, B.D. 1994. Large mid-Holocene and late Pleistocene earthquakes on the Oquirrh fault zone: Utah. *Geomorph.* 10, 285-315.
- Olig, S.S., Gorton, A.E., Black, B.D., Forman, S.L. 2001. Paleoseismology of the Mercur fault and segmentation of the Oquirrh-East Great Salt Lake fault zone, Utah: Final Technical Report to the U.S. Geological Survey National Earthquake Hazards Reduction Program, Award No. 98HQGR1036.

- Oviatt, C.G., Currey, D.R., Sack, D. 1992. Radiocarbon chronology of Lake Bonneville, eastern Great Basin, USA. *Palaeogeography, Palaeoclimatology, Palaeoecology* 99, 225-241. doi:10.1016/0031-0182(92)90017-Y
- Parsons, T., Ji, C., Kirby, E. 2008. Stress changes from the 2008 Wenchuan earthquake and increased hazard in the Sichuan basin. *Nature* 454, 509-510.
- Parsons, T., Segou, M. 2014. Stress, Distance, Magnitude, and Clustering Influences on the Success or Failure of an Aftershock Forecast: The 2013 M 6.6 Lushan Earthquake and Other Examples. *Seismol. Res. Lett.* 85, 44-51.
- Personius, S.F., DuRoss, C.B., Crone, A.J. 2012. Holocene Behavior of the Brigham City Segment: Implications for Forecasting the Next Large-Magnitude Earthquake on the Wasatch Fault Zone, Utah. *Bull. Seismol. Soc. Am.* 102, 2265-2281. doi:10.1785/0120110214
- Piersanti, A., Spada, G., Sabadini, R., Bonafede, M. 1995. Global post-seismic deformation. *Geophys. J. Int.* 120, 544-566. doi:10.1111/j.1365-246X.1995.tb01838.x
- Piersanti, A., Spada, G., Sabadini, R. 1997. Global postseismic rebound of a viscoelastic Earth: Theory for finite faults and application to the 1964 Alaska earthquake. *J. Geophys. Res.* 102, 477-492.
- Piombo, A., Martinelli, G., Dragoni, M. 2005. Post-seismic fluid flow and Coulomb stress changes in a poroelastic medium. *Geophys. J. Int.* 162, 507-515.
- Pollitz, F.F. 1997. Gravitational viscoelastic postseismic relaxation on a layered spherical Earth. *J. Geophys. Res.* 102, 17921-17941.
- Pollitz, F.F., Sacks, I.S. 2002. Stress triggering of the 1999 Hector Mine earthquake by transient deformation following the 1992 Landers earthquake. *Bull. Seismol. Soc. Am.* 92, 1487-1496. doi:10.1785/0120000918
- Pollitz, F.F., Stein, R.S., Sevilgen, V., Bürgmann, R. 2012. The 11 April 2012 east Indian Ocean earthquake triggered large aftershocks worldwide. *Nature* 490, 250-255.
- Ranalli, G. 1995. *Rheology of the Earth*. London.
- Reid, H.F. 1910. The California earthquake of April 18, 1906. Report of the (California) State Earthquake Investigation Commission, vol. 2: The mechanics of the earthquake. Washington.
- Riva, R.E.M., Borghi, A., Aoudia, A., Barzaghi, R., Sabadini, R., Panza, G.F. 2007. Viscoelastic relaxation and long-lasting after-slip following the 1997 Umbria-Marche (Central Italy) earthquakes. *Geophys. J. Int.* 169, 534-546. doi:10.1111/j.1365-246X.2007.03315.x

- Roberts, G.P., Michetti, A.M. 2004. Spatial and temporal variations in growth rates along active normal fault systems: an example from the Lazio–Abruzzo Apennines, central Italy. *J. Struct. Geol.* 26, 339-376.
- Ryder, I., Bürgmann, R., Fielding, E. 2012. Static stress interactions in extensional earthquake sequences: An example from the South Lunggar Rift, Tibet. *J. Geophys. Res.* 117, B09405. doi:10.1029/2012JB009365
- Scholz, C.H. 1998. Earthquakes and friction laws. *Nature* 391, 37-42. doi:10.1038/34097
- Scholz, C.H. 2002. *The mechanics of earthquakes and faulting*. New York.
- Schwartz, D.P., Coppersmith, K.J. 1984. Fault behavior and characteristic earthquakes: Examples from the Wasatch and San Andreas fault zones. *J. Geophys. Res.* 89, 5681-5698. doi:10.1029/JB089iB07p05681
- Serpelloni, E., Anderlini, L., Belardinelli, M.E. 2012. Fault geometry, coseismic-slip distribution and Coulomb stress change associated with the 2009 April 6, M_w 6.3, L'Aquila earthquake from inversion of GPS displacements. *Geophys. J. Int.* 188, 473-489.
- Shan, B., Xiong, X., Wang, R., Zheng, Y., Yang, S. 2013. Coulomb stress evolution along Xianshuihe–Xiaojiang Fault System since 1713 and its interaction with Wenchuan earthquake, May 12, 2008. *Earth Planet. Sci. Lett.* 377, 199-210.
- Shi, X., Kirby, E., Furlong, K.P., Meng, K., Robinson, R., Wang, E. 2015. Crustal strength in central Tibet determined from Holocene shoreline deflection around Siling Co. *Earth Planet. Sci. Lett.* 423, 145–154.
- Shimazaki, K., Nakata, T. 1980. Time-predictable recurrence model for large earthquakes. *Geophys. Res. Lett.* 7, 279-282. doi:10.1029/GL007i004p00279
- Shirzaei, M., Ellsworth, W.L., Tiampo, K.F., González, P.J., Manga, M. 2015. Surface uplift and time-dependent seismic hazard due to fluid-injection in eastern Texas. *Science* 353, 1416-1419.
- Sibson, R.H. 1986. Brecciation processes in fault zones: inferences from earthquake upturning. *Pure and Applied Geophysics* 124, 159-175. doi:10.1007/BF00875724
- Smith, R.B., Bruhn, R.L. 1984. Intraplate extensional tectonics of the eastern Basin-Range: Inferences on structural style from seismic reflection data, regional tectonics, and thermal-mechanical models of brittle-ductile deformation. *J. Geophys. Res.* 89, 5733-5762. doi:10.1029/JB089iB07p05733
- Smith, B.R., Sandwell, D.T. 2006. A model of the earthquake cycle along the San Andreas Fault System for the past 1000 years. *J. Geophys. Res.* 111, B01405. doi:10.1029/2005JB003703

- Stein, R.S. 1999. The role of stress transfer in earthquake occurrence. *Nature* 402, 605-609.
doi:10.1038/45144
- Stein, R.S. 2003. Earthquake Conversations. *Scientific American* 288, 72-79.
doi:10.1038/scientificamerican0103-72
- Stein, R.S., King, G.C., Lin, J. 1992. Change in Failure Stress on the Southern San Andreas Fault System Caused by the 1992 Magnitude = 7.4 Landers Earthquake. *Science* 258, 1328-1332.
- Stein, R.S., Barka, A.A., Dieterich, J.H. 1997. Progressive failure on the North Anatolian fault since 1939 by earthquake stress triggering. *Geophys. J. Int.* 128, 594-604.
- Sun, T., Wang, K., Iinuma, T., Hino, R., He, J., Fujimoto, H., Kido, M., Osada, Y., Miura, S., Ohta, Y., Hu, Y. 2014. Prevalence of viscoelastic relaxation after the 2011 Tohoku-oki earthquake. *Nature* 514, 84-87.
- Swan, F.H., Schwartz, D.P., Cluff, L S. 1980. Recurrence of moderate to large magnitude earthquakes produced by surface faulting on the Wasatch fault zone, Utah. *Bull. Seismol. Soc. Am.* 70, 1431-1462.
- Toda, S., Lin, J., Meghraoui, M., Stein, R.S. 2008. 12 May 2008 $M = 7.9$ Wenchuan, China, earthquake calculated to increase failure stress and seismicity rate on three major fault systems. *Geophys. Res. Lett.* 35, L17305.
- Toda, S., Stein, R.S., Sevilgen, V., Lin, J. 2011. Coulomb 3.3 Graphic-rich deformation and stress-change software for earthquake, tectonic, and volcano research and teaching—user guide: U.S. Geological Survey Open-File Report 2011-1060, available at <http://pubs.usgs.gov/of/2011/1060/>
- Townend, J., Zoback, M.D. 2000. How faulting keeps the crust strong. *Geology* 28, 399-402.
- Turcotte, D. L., Schubert, G. 2002. *Geodynamics*. Cambridge.
- Wallace, R.E. 1987. Grouping and migration of surface faulting and variation in slip rates on faults in the Great Basin province. *Bull. Seismol. Soc. Am.* 77, 868–877.
- Wan, Y., Shen, Z.K. 2010. Static Coulomb stress changes on faults caused by the 2008 M_w 7.9 Wenchuan, China earthquake. *Tectonophysics* 491, 105-118.
- Wang, J., Xu, C., Freymueller, J.T., Li, Z., Shen, W. 2014a. Sensitivity of Coulomb stress change to the parameters of the Coulomb failure model: A case study using the 2008 M_w 7.9 Wenchuan earthquake. *J. Geophys. Res.* 119, 3371-3392.
- Wang, Y., Wang, F., Wang, M., Shen, Z.K., Wan, Y. 2014b. Coulomb Stress Change and Evolution Induced by the 2008 Wenchuan Earthquake and its Delayed Triggering of the 2013 M_w 6.6 Lushan Earthquake. *Seismol. Res. Lett.* 85, 52-59.

- Wells, D.L., Coppersmith, K.J. 1994. New Empirical Relationships among Magnitude, Rupture Length, Rupture Width, Rupture Area, and Surface Displacement. *Bull. Seismol. Soc. Am.* 84, 974-1002.
- Wernicke, B., Friedrich, A.M., Niemi, N.A., Bennett, R.A., Davis, J.L. 2000. Dynamics of Plate Boundary Fault Systems from Basin and Range Geodetic Network (BARGEN) and Geologic Data. *GSA Today* 10, 1-7.
- WGUEP (Working Group on Utah Earthquake Probabilities) 2016. Earthquake probabilities or the Wasatch Front region in Utah, Idaho, and Wyoming: Utah Geological Survey Miscellaneous Publication 16-3.
- Woessner, J., Jónsson, S., Sudhaus, H., Baumann, C. 2012. Reliability of Coulomb Stress Changes inferred from correlated uncertainties of finite-fault source models. *J. Geophys. Res.* 117. doi:10.1029/2011JB009121

9 Curriculum Vitae

Name	Meike Bagge
Date of birth	14.08.1989
Place of birth	Langenhagen
Citizenship	German

2002 – 2008	Abitur Gymnasium Herschelschule Hannover
-------------	--

10/2008 – 08/2011	Bachelor of Science in Geosciences Leibniz Universität Hannover
-------------------	---

10/2011 – 09/2013	Master of Science in Geosciences Leibniz Universität Hannover
-------------------	---

since 10/2013	Research staff (doctoral candidate) Institut für Geologie Leibniz Universität Hannover
---------------	---

10 Publications

Publications in peer-reviewed journals

- **Bagge, M.**, Hampel, A. 2016. Three-dimensional finite-element modelling of coseismic Coulomb stress changes on intra-continental dip-slip faults. *Tectonophysics* 684, 52-62. doi:10.1016/j.tecto.2015.10.006
- Polom, U., **Bagge, M.**, Wadas, S., Winsemann, J., Brandes, C., Binot, F., Krawczyk, C. M. 2013. Surveying near-surface depocentres by means of shear wave seismics. *First Break* 31, 67-79.
- Barckhausen, U., **Bagge, M.**, Wilson, D. S. 2013. Seafloor spreading anomalies and crustal ages of the Clarion-Clipperton Zone, *Marine Geophys. Res.* 34, 79-88. doi:10.1007/s11001-013-9184-6

Manuscripts in review or in preparation

- **Bagge, M.**, Hampel, A. Postseismic Coulomb stress changes on intra-continental dip-slip faults due to viscoelastic relaxation in the lower crust and lithospheric mantle: insights from 3D finite-element modelling, submitted to *International Journal of Earth Sciences*.
- **Bagge, M.**, Hampel, A., Gold R. Coulomb stress changes on the Wasatch fault (Utah), in prep.

Conference contributions

- **Bagge, M.**, Hampel, A. 2016 (poster). Coseismic and postseismic Coulomb stress changes on intra-continental dip-slip faults and the role of viscoelastic relaxation in the lower crust: insights from 3D finite-element models. EGU General Assembly, Wien.
- **Bagge, M.**, Hampel, A. 2015 (talk). 3D-Finite-Element Modelling of Coseismic and Postseismic Coulomb Stress Changes on Intra-Continental Dip-Slip Faults. AGU Fall Meeting, San Francisco.
- **Bagge, M.**, Hampel, A. 2015 (poster). 3D finite-element modelling of postseismic Coulomb stress changes on intra-continental normal and thrust faults. SIMULIA Community Conference, Berlin.
- **Bagge, M.**, Hampel, A. 2015 (poster). Postseismic Coulomb stress changes on intra-continental dip-slip faults: insights from three-dimensional finite-element modelling. 75. Jahrestagung der Deutschen Geophysikalischen Gesellschaft, Hannover.

- **Bagge, M.**, Hampel, A. 2014 (talk). Three-dimensional finite-element modelling of coseismic Coulomb stress changes on intra-continental dip-slip faults. GeoFrankfurt 2014, Frankfurt.
- **Bagge, M.**, Hampel, A. 2014 (poster). Coseismic Coulomb stress changes on intra-continental normal and thrust faults: insights from three-dimensional finite-element modelling. GeoMod2014, Potsdam.
- **Bagge, M.**, Barckhausen, U. 2013 (talk). Magnetische Anomalien im zentralen Pazifik zwischen der Clarion- und Galapagos-Fracture Zone. 73. Jahrestagung der Deutschen Geophysikalischen Gesellschaft, Leipzig.
- **Bagge, M.**, Polom, U., Brandes, C., Winsemann, J. 2013 (poster). Scherwellen-Reflexionsseismik zur Erkundung des oberflächennahen quartären Untergrundes im Raum Nörten-Hardenberg. 73. Jahrestagung der Deutschen Geophysikalischen Gesellschaft, Leipzig.
- **Bagge, M.**, Barckhausen, U. 2012 (poster). Tektonische Entwicklung des östlichen deutschen Manganknollen-Lizenzgebietes. GeoHannover 2012, Hannover
- **Bagge, M.**, Barckhausen, U. 2012 (poster). Überlieferung der Plattenreorganisation im Ostpazifik – Das östliche deutsche Manganknollen-Lizenzgebiet. 72. Jahrestagung der Deutschen Geophysikalischen Gesellschaft, Hamburg.